

MODELING OF MICRODISCHARGES FOR DISPLAY TECHNOLOGY

PROEFSCHRIFT

ter verkrijging van de graad van doctor
aan de Technische Universiteit Eindhoven,
op gezag van de Rector Magnificus, prof.dr. M. Rem,
voor een commissie aangewezen door het College
voor Promoties in het openbaar te verdedigen
op maandag 13 november 2000 om 16.00 uur

door

Gerardus Johannes Maria Hagelaar

geboren te Helmond

Dit proefschrift is goedgekeurd door de promotoren:

prof.dr.ir. G. M. W. Kroesen
en
prof.dr. F. J. de Hoog

Copromotor:
dr. L. Vriens

The work described in this thesis was financially supported by the Philips Research Laboratories in Eindhoven, The Netherlands.

CIP-DATA LIBRARY TECHNISCHE UNIVERSITEIT EINDHOVEN

Hagelaar, Gerardus Johannes Maria

Modeling of microdischarges for display technology / by Gerardus Johannes Maria Hagelaar

Eindhoven: Technische Universiteit Eindhoven, 2000. –Proefschrift.–

ISBN 90-386-1659-7

NUGI 812

Trefw.: PALC / PDP / gasontlading / plasmamodellering / plasmasimulatie

Subject headings: PALC / PDP / gas discharge / plasma modeling / plasma simulation

Drukwerk: Universiteitsdrukkerij Technische Universiteit Eindhoven

Contents

1. Introduction	5
1.1 Introduction	5
1.2 The plasma addressed liquid crystal (PALC) technology	5
1.3 The plasma display panel (PDP) technology	7
1.4 Physical characterization of the microdischarges	9
1.5 Discharge modeling	10
1.6 The scope of this thesis	11
2. A fluid model of microdischarges	13
2.1 Introduction	13
2.2 The system of fluid equations	13
2.3 New boundary conditions for particle transport	15
2.4 The boundary conditions for the system of fluid equations	20
2.5 Input data for the simulation of PALC discharges	21
2.6 Input data for the simulation of PDP discharges	24
3. The numerical solution of the fluid equations	29
3.1 Introduction	29
3.2 Time integration of the system of equations	29
3.3 Implicit treatment of the electron energy source term	30
3.4 Spatial grid and the definition of the discharge configuration	35
3.5 Spatial discretization of the transport equations	35
3.6 Spatial discretization of Poisson's equation	38
3.7 The solution of five-point equations	40
4. The fluid simulation of PALC discharges	43
4.1 Introduction	43
4.2 Discharge pulse	46
4.3 Afterglow	47
4.4 Addressing	49
4.5 Conclusions	52
5. Energy loss mechanisms in PDP discharges	53
5.1 Introduction	53
5.2 Simulation of a PDP discharge	54
5.3 Analysis of the energy dissipation	56
5.4 Parametric studies	58
5.5 Conclusions	62
6. A Monte Carlo modeling study of the electrons in PALC discharges	63
6.1 Introduction	63
6.2 PALC discharges	64
6.3 Overview of the Monte Carlo model	66
6.4 The simulation of an electron path	68

6.5 Results for a DC discharge	71
6.6 Results for the afterglow	74
6.7 Conclusions	76
7. The energy distribution of ions and fast neutrals	77
7.1 Introduction	77
7.2 The ion energy distribution	78
7.3 Fast neutrals	80
7.4 Monte Carlo calculations	81
7.5 Conclusions	85
8. Resonance radiation transport in PDP discharges	87
8.1 Introduction	87
8.2 The photon Monte Carlo model	89
8.3 Comparison with the trapping factor approach	91
8.4 Comparison with experimental results	92
8.5 Conclusions	94
9. Conclusions	95
References	97
Publications	103
Summary	105
Samenvatting	107
Dankwoord	109
Curriculum vitae	109

Chapter 1

Introduction

1.1 Introduction

To the present day, the television (TV) market has been dominated by bulky cathode ray tube (CRT) displays. Yet, display researchers have always been looking for more elegant alternatives. Recently, two alternative display technologies have emerged, that offer the possibility of large, lightweight, flat TV monitors. Both of these technologies make use of exceptionally small gas discharges: microdischarges. The best known is the plasma display panel (PDP) technology, using microdischarges to generate the light of the display. The other is the plasma addressed liquid crystal (PALC) technology, where microdischarges serve as electrical switches.

Before the PALC and PDP displays are ready to replace the conventional CRT displays, they need considerable improvements in performance, lifetime, and cost price. Most of the weaknesses of PALC and PDP are directly related to the operation of the microdischarges. To be able to improve the properties of these discharges, it is necessary to understand the underlying physics. Discharge modeling can be very useful in obtaining this understanding, even more so since the microdischarges are so small that they are hardly accessible to most experimental diagnostics.

As suggested by its title, this thesis deals with the modeling of the microdischarges. In this chapter we provide the necessary background information. Sections 1.2 and 1.3 describe the operation principles and improvement issues of the PALC and the PDP technologies, respectively. Section 1.4 physically characterizes the microdischarges. Section 1.5 gives an introduction to discharge modeling. Finally, in Section 1.6, we define the aim of the work presented in this thesis and give an outlook over the following chapters.

1.2 The plasma addressed liquid crystal (PALC) technology

The PALC technology was invented at Tektronics in 1990, and has been described in several publications from that company, e.g. in Refs. [Buz90, Buz93, Kak95]. At present, several display manufacturers are involved in the development of PALC displays.

The PALC technology is a variant of the liquid crystal display (LCD) technology that is nowadays widely used in portable computers. Just like other LCDs, PALC displays are passive: they do not generate light, but modulate the light generated by a device behind the display (backlight), utilizing the unique optical properties of liquid crystal. Liquid crystal (LC) is an electro-optic material: it alters the state of polarization of light passing through it, where the polarization changing effect depends on the electric field applied to the LC. In LCDs, light from a uniform backlight passes first through a polarizing layer, then through a layer of LC, and finally through a second polarizing layer. The percentage of light transmitted by the second polarizer depends on the electric field in the LC, which is controlled independently for each display element (pixel) by an electrical switching element. Conventional LCDs use

thin film transistors (TFTs) as switching devices. Due to the extreme tolerances of the submicron semiconductor technology needed to manufacture the TFTs, the yield expectations are low for larger display sizes (>20 in. diagonal). In PALC displays, however, the pixels are addressed by plasma switching devices, which are much more easily manufactured, permitting the production of large size displays. In contrast to the TFT LCD technology, the PALC technology does seem to be suitable for large size TV applications.

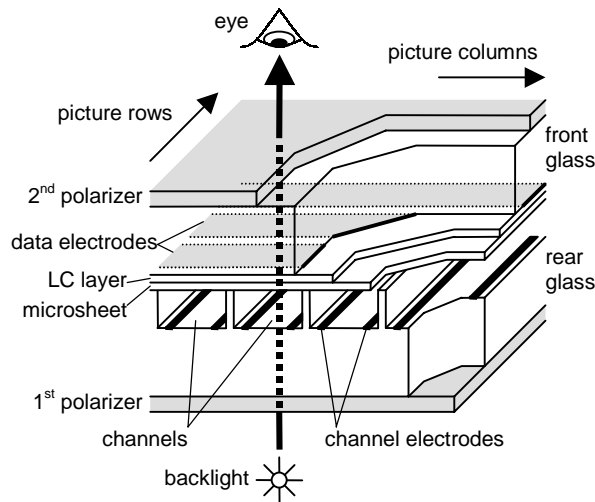


Figure 1.1. Schematic drawing of a PALC display.

Figure 1.1 schematically depicts a PALC panel. The LC and a protective microsHEET are sandwiched between two glass plates. The rear plate contains parallel channels filled with a discharge gas, typically helium or a helium-based binary mixture at a pressure of a few hundred Torr. The channels correspond to the picture rows of the display. Two thin parallel electrodes run all along the bottom of each channel. The front glass plate is patterned with so-called data electrodes: transparent, conductive stripes of indium-tin-oxide (ITO), which correspond to the picture columns of the display. A pixel is formed by the intersection of a channel and a data electrode.

The image on the display is written row by row, i.e. all pixels of one picture row are addressed at the same time. In order to address a certain row, a discharge is created in the corresponding channel, by applying a short DC voltage pulse to the channel electrodes. During the afterglow of the discharge, small voltages - representing the data to be written on the pixels of the row - are applied between the data and channel electrodes. The decaying plasma in the channel screens itself from the resulting electric fields, by depositing surface charge on the microsHEET. It continues to build up this surface charge until the fields in the channel have vanished and the data voltages stand entirely across the LC layer and the microsHEET. After the plasma has completely decayed, the surface charge is fixed and unaffected by any change in the data voltages. The electric fields in the LC - and the transmission through the second polarizer - will now remain nearly unchanged until the next discharge pulse is applied to the channel.

One of the major concerns of PALC is the addressing speed. For modern high definition TV applications, at least 1000 lines (rows) have to be addressed per frame, that is, 50-60 times a second. This implies that the total time required to write one line should be at most 16.7 μ s, and preferably much shorter. The PALC discharges should

therefore ignite quickly and have a short decay time; one should realize that if the plasma is not entirely gone by the end of the addressing time, charging errors will occur. In addition, it is important that the charging of the microsheet is accurate and as uniform as possible: inhomogenities in the charging translate directly into a loss of contrast. Another issue of concern is the lifetime of the displays, which might be limited by ion-induced sputtering of channel electrode material. The PALC discharges should also not emit disturbing light. Finally, in view of the cost price of PALC displays, it is important that the required driving voltages are not too high and that the microdischarge geometry can be manufactured easily.

1.3 The plasma display panel (PDP) technology

The basic principles of the PDP technology were first demonstrated in the 1960s. Since then, the technology has continuously been improved and is now one of the most promising technologies for large size TVs. Since the early 1990s most of the world's major TV manufacturers have been involved in the development of PDPs; recently the first PDP TVs have appeared on the market. There is an extensive literature on the principles of PDPs; here we explicitly mention the review articles [Wes75, Slo76, Web85, Sob91].

A PDP consists of two glass plates, which are sealed together with a gap of 100-200 μm . The gap between the plates is filled with a discharge gas at a pressure of 400-500 Torr. Each plate has a large number of thin parallel electrodes deposited on its inner surface, where the electrodes on the two plates are at right angles, and correspond to the rows and columns of the display. At each intersection of a row and a column electrode, a gas discharge can be switched on and off independently, by applying appropriate voltage pulses to the electrodes in question. The discharge leads to the formation of a plasma that emits visible and ultraviolet (UV) light. In monochrome PDPs the visible light is used directly, whereas in color PDPs the UV radiation is used to excite phosphors that in turn emit red, blue, or green light. The discharge gas is typically a rare gas mixture. Color PDPs always contain a percentage of xenon; of the rare gases, xenon is the most efficient in emitting UV radiation.

The electrodes can be driven in various ways, where the discharges operate in either the direct current (DC) or the alternating current (AC) mode. In DC driven PDPs the electrodes are in direct contact with the discharge gas, whereas in AC designs they are covered with a dielectric layer. Two types of AC PDPs can be distinguished: the opposed-electrode type, where the discharges occur between the column and the row electrodes on the different plates, and the coplanar-electrode type, where the discharges occur between pairs of electrodes on one plate and are triggered by the electrodes on the other plate. The coplanar-electrode AC PDP - also known as the surface-discharge PDP - is considered by most manufacturers as the most promising type for TV applications.

Figure 1.2 gives a schematic representation of a color PDP of this type. The discharges occur between the so-called sustain electrodes on the front plate. These electrodes are transparent and covered by a glass layer. A magnesium-oxide (MgO) thin film is deposited on top of the glass layer to protect it from incident ion flux and to increase the secondary electron emission coefficient of the surface. The rear glass plate is equipped with so-called address electrodes, which are used to switch the discharges on and off, and correspond to the picture columns. In order to avoid electrical and

optical interaction between the columns, dielectric barriers (ribs) are deposited in between the address electrodes. The rear plate and the side walls of the ribs are coated with phosphors; alternately red, blue, and green phosphors are used for consecutive columns. A picture element (pixel) is formed by the intersection of a pair of sustain electrodes and one address electrode.

In operation a square wave voltage with a frequency of 50 – 250 kHz (sustain voltage) is constantly applied to the sustain electrodes. This voltage is just below the breakdown voltage: in itself cannot ignite a discharge. To turn a certain pixel on, an additional voltage pulse (write pulse) is applied to the address electrode and one of the sustain electrodes (scan electrode) of the pixel. The resulting discharge is quickly quenched due to the accumulation of surface charge on the dielectrics covering the electrodes, which screens the discharge gas from the sustain voltage. However, on its next half cycle the sustain voltage changes polarity. The stored surface charge now reinforces the effect of the sustain voltage, causing a new discharge to be ignited, despite the fact that the sustain voltage itself is smaller than the breakdown voltage. A new surface charge distribution quickly develops, quenches the discharge again, and so on. In this way, a new transient discharge occurs at each half cycle of the sustain voltage, as long as surface charge is present. Note that the surface charge changes polarity every half cycle of the sustain voltage. The pixel is turned off by applying a so-called erase pulse to the address and sustain electrodes, which disturbs or erases the surface charge distribution.

When a pixel is on, pulses of UV photons hit the phosphors at twice the sustain frequency, which results in a certain (time averaged) intensity of emitted visible light. The intensity of the pixel is controlled by controlling the fractions of the time that the pixel is on and off. For this purpose, every picture frame is divided into a number of (binary weighted) subframes, during which pixels can be either on or off.

An important drawback of PDPs is their low luminous efficacy: only about 1 lm/Watt, compared to 4 lm/Watts for the conventional CRTs. One of the few possibilities to improve this, is to improve the efficiency of the microdischarges in generating UV photons, which is only about 10% in present-day PDPs. Another issue that needs improvement is the writing and erasing of the pixels: this should be reliable and – in view of the cost price - require not too high driving voltages.

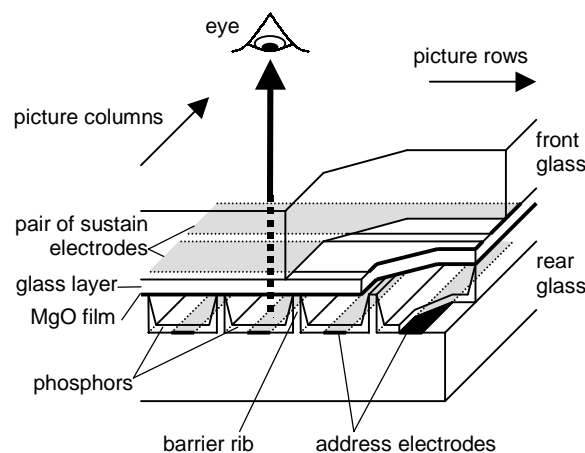


Figure 1.2. Schematic drawing of a coplanar-electrode AC PDP.

1.4 Physical characterization of the microdischarges

In gas discharges, electric current is conducted through a gas. There are many different types of gas discharges, having different physical principles; an excellent overview can be found in Ref. [Rai91]. The microdischarges in PALC and PDP displays are of a discharge type called glow discharge. More specifically, they are pulsed DC glow discharges; for even in AC PDPs, the discharges have a DC-like character. Table 1.1 outlines the characteristic properties of the microdischarges considered in this thesis.

In glow discharges the gas is only weakly ionized, but still has – for the most part – clearly the character of a plasma. Due to the low ionization degree, recombination is of minor importance, and most of the charged particles are lost by transport to the surface. The plasma is far from thermal equilibrium: the gas and the electrodes are relatively cold, heated only slightly above room temperature, while the electron mean energy reaches values of 1 eV and beyond.

DC glow discharges are sustained by the emission of secondary electrons from the cathode, due primarily to positive ion impact. The secondary electrons are accelerated toward the anode by the electric field, and obtain such high energies that they start ionizing neutral gas particles. The electrons thus created are also accelerated, and an ionization avalanche forms. In a fully developed glow discharge, the region in front of the cathode – known as cathode fall – contains a positive space charge, which screens the remainder of the discharge largely from the applied electric field. Ionization only occurs in and around the cathode fall, and the size of the cathode fall is such, that the ionization exactly balances the ion loss at the cathode: if one ion releases γ secondary electrons, then one secondary electron must cause $1/\gamma$ ionizations on its trip to the anode.

Table 1.1. Typical values of some important discharge parameters for the microdischarges in PALC displays and coplanar-electrode type PDPs. Parameters tagged with a star are given per unit of electrode length.

Parameter	DC PALC	coplanar AC PDP
gas	He-H ₂ (0 – 5%)	Ne-Xe (3 – 10%)
gas pressure	100 – 200 Torr	400 – 500 Torr
gas temperature	300 – 320 K	300 – 320 K
electrode distance	200 – 300 μm	50 – 100 μm
discharge type	pulsed DC glow	pulsed DC glow
discharge duration	2 – 10 μs	30 – 100 ns
discharge frequency	~60 kHz	100 – 500 kHz
applied voltage	200 – 300 V	120 – 250 V
peak current*	1.5 – 5 mA cm ⁻¹	10 – 50 mA cm ⁻¹
energy deposition*	2 – 10 $\mu\text{J cm}^{-1}$	0.3 – 0.6 $\mu\text{J cm}^{-1}$
plasma density	$5 \times 10^{11} - 5 \times 10^{12} \text{ cm}^{-3}$	$10^{13} - 10^{14} \text{ cm}^{-3}$
ionization degree	$10^{-7} - 10^{-6}$	$10^{-6} - 10^{-5}$
electron mean energy (cathode fall)	40 – 70 eV	20 – 25 eV
electron mean energy (plasma)	4 – 10 eV	2 – 6 eV
electron elastic collision length	2 – 5 μm	1 – 3 μm
electron ionization length (cath. fall)	20 – 50 μm	2 – 10 μm
Debye length (plasma)	6 – 30 μm	1 – 6 μm
number of electrons in Debye sphere	4000 – 50000	400 – 8000

The gas pressure in the microdischarges is much higher than the pressure in the normal size glow discharges that are used in discharge lamps or for materials processing. However, one should realize that not the pressure, but the product of pressure and electrode distance – a measure for the number of atoms an electron encounters on its trip from cathode to anode – determines the similarity of discharges. For example, according to the Paschen law, the voltage required for the development of a glow discharge (breakdown voltage) is a function of the pressure-distance product. For microdischarges, as for other glow discharges, this product is around 5 Torr cm.

Finally, we remark that the term microdischarges is not specific for the discharges in display technology; it is also used for other small discharge phenomena with fundamentally different characteristics.

1.5 Discharge modeling

In physics, the word “model” is used to indicate a system of equations, data, and assumptions, which gives a mathematical representation of all the major features of a certain physical phenomenon. By solving the model equations, the physical phenomenon is simulated. Models are used to theoretically interpret and predict experimental observations. They are crucial in the research of phenomena that involve many different theoretical aspects at the same time, so that the link between theory and experiment is rather complicated; gas discharges are good examples of such phenomena. The invention of the computer – an excellent tool for solving equations numerically – has greatly increased the possibilities of modeling. Numerical models have become so popular, that the word model itself has become associated with the computer implementation of model equations, rather than with the equations themselves. In the past few decades, numerical discharge models have been developed in plasma groups all over the world. Two major modeling approaches can be distinguished:

In the fluid approach, the plasma particle species (electrons, ions, excited neutrals) are represented by macroscopic quantities such as particle number density, flux, mean energy. The space and time variation of these quantities is described by fluid equations, which are derived from the Boltzmann equation [Shk66, Gog92]. Surface processes are accounted for in the boundary conditions of the fluid equations. Usually the fluid equations are coupled to macroscopic Maxwell equations, such as Poisson’s equation, which describes the effect of space charge on the electric field. In this way, a complete, self-consistent description of the discharge is obtained. Unfortunately, the fluid equations and the boundary conditions incorporate restrictive assumptions concerning the particle transport. In addition, they require input data on macroscopic properties of the particles (diffusion coefficients, reaction rate coefficients), which are based on assumptions of the particle energy distribution function. Due to all these assumptions, the fluid approach can only be applied over a limited range of discharge conditions. However, in the case of glow discharges, fluid models have proved to be very useful in helping to understand the basic discharge properties and in predicting trends. Fluid models are computationally efficient: they can simulate the time evolution of a discharge in one or two spatial dimensions within a manageable period of computation time, say, a few hours.

More detail is given by the particle approach. In particle models – also known as Monte Carlo models – the paths of individual plasma particles are simulated, where the

occurrence and effect of collisions are treated by random numbers. Since it is infeasible to calculate the paths of all particles, only a number – sufficiently large to produce reliable and smooth results – of representative test particles is followed. From the test particle paths, macroscopic quantities (density, flux, etc.), as well as the particle energy distribution function, can be inferred. To self-consistently calculate the electric field, particle models require a rather complicated technique, called the particle-in-cell technique. Since no assumptions are made concerning the particle transport or the particle energy distribution functions, particle models can be applied over wide range of discharge conditions. However, they need the input of collision cross section data, which are often unknown or have large experimental uncertainties. In view of the large computational effort they take, particle models are not very suitable to study complex discharge geometries and chemistries; they are more often used to validate fluid models.

The two major discharge modeling approaches can also be combined in one single model: In hybrid models, one part of the particles is described by fluid equations, and the other part (often the high energy electrons) is treated with a Monte Carlo simulation.

The discharge conditions of microdischarges are on the edge of what can be reliably simulated with a fluid model. However, the simulation of the rather complex operation of these discharges absolutely requires the computational efficiency of the fluid approach; particle models are simply too time consuming to study the full microdischarge operation. Several fluid models of PDP discharges have been developed and described in the literature, some of them 1D [Meu95, Vee95], some 2D [Cho95, Cam95, Pun98, Rau99]. Much less work has been done on the modeling of PALC discharges: so far, only one model [Ilc97] of PALC discharges has been reported.

1.6 The scope of this thesis

The main aim of the work presented in this thesis is to obtain of a self-consistent model, which is suitable for the simulation of the microdischarges used in PALC and PDP, which helps understand the behavior of these discharges, and which can be used as a tool for optimizing the microdischarge operating conditions, geometry, and gas composition. In addition to this, there is the more academic goal to contribute to discharge modeling in general. Let it be clear that the actual improvement of the PALC and PDP technologies is not – at least not directly – the aim of this work.

The Chapters 2 through 5 form the basis of this thesis: they present a two-dimensional fluid model that can be used for the complete simulation of the microdischarges used in display technology. Chapter 2 discusses the physical basis of the fluid model. In order to make the fluid model useful as a research tool, an efficient numerical implementation is required. Chapter 3 provides all the details of this numerical implementation. In the Chapters 4 and 5, we present examples of fluid modeling studies of PALC and PDP discharges, respectively. The modeling results presented in these chapters are compared with experimental results wherever possible; experimental validation of the fluid model is thus done.

In the Chapters 6-8 we look beyond the fluid modeling approach. Chapter 6 presents a Monte Carlo (particle) model for the electrons in microdischarges. We use this model to investigate the validity and the consequences of one of the most

restrictive assumptions of the fluid model: the assumption concerning the electron energy distribution function. In Chapter 7, we attempt to predict – on the basis of fluid modeling results - the energy distribution of ions and fast neutrals impinging on the surface; this is important for the lifetime of PALC and PDP displays. We use both an elementary theoretical approach and a more comprehensive Monte Carlo approach. Chapter 7 focuses on the resonance radiation transport in PDPs, which is only very crudely accounted for in the fluid model. We present a Monte Carlo model for resonance photons, which gives a much more accurate description of this phenomenon.

Chapter 2

A fluid model of microdischarges

2.1 Introduction

The basis of the work presented in this thesis is a self-consistent fluid model. This model gives a complete description of a discharge, accounting for all its major physical aspects: transport of particles, transport of momentum, transport of energy, plasma chemistry, space and surface charge induced electric fields, emission of radiation. In this chapter we describe the physical equations and data that define the fluid model. Section 2.2 outlines the basic system of equations. These equations describe the relations between all important physical quantities in the bulk, but do not describe what happens at the surfaces that surround the discharge. Surface processes are incorporated as boundary conditions for the basic equations. Before lining up all the boundary conditions in Section 2.4, we discuss, in Section 2.3, the physical background of our boundary conditions for particle transport; these conditions are different from anything previously used by other authors. In the Sections 2.5 and 2.6 we describe two extensive sets of input data for the simulation of discharges in helium-hydrogen mixtures and neon-xenon mixtures, respectively.

2.2 The system of fluid equations

We pursue the well-known fluid approach and describe the behavior of plasma particles by the first few velocity moments of the Boltzmann equation: the continuity equation, the momentum balance equation, and the energy balance equation. These equations – also known as transport equations - are coupled to Poisson's equation for the electric field. Since this approach has been described previously in numerous papers [Mey90, Boe87, Meu95, Boe95, Pun98, Pas93, Cho95, Vee95, Vee96, Vee97, Cam95, Iva99], we will only briefly outline it here. For the derivation of the transport equations from the Boltzmann equation we refer to Ref. [Gog92].

Given the low ionization degree, the density and temperature of the gas particles are assumed to be constant and unaffected by the discharge. For every plasma particle species p , the time evolution of the density is described by a continuity equation

$$\frac{\partial n_p}{\partial t} + \nabla \cdot \mathbf{\Gamma}_p = S_p, \quad (2.1)$$

where n_p is the density, $\mathbf{\Gamma}_p$ the flux, S_p the source term, and the index p can indicate: electrons ($p = e$), an ion species, or a neutral species. The flux is given by the momentum balance equation, which we approximate by the drift-diffusion equation

$$\mathbf{\Gamma}_p = \text{sgn}(q_p) \mu_p \mathbf{E} n_p - D_p \nabla n_p. \quad (2.2)$$

Here \mathbf{E} is the electric field, q_p the particle charge, μ_p the mobility and D_p the diffusion coefficient. The first term gives the flux due to the electric field (drift) and the second term represents the flux due to concentration gradients (diffusion). Particle inertia is neglected.

The source term S_p is determined by the reactions occurring in the discharge. It consists of positive contributions from the reactions in which a particle of species p is created and negative contributions from those in which such a particle is lost:

$$S_p = \sum_r c_{p,r} R_r . \quad (2.3)$$

The index r refers to a reaction; $c_{p,r}$ is the net number of particles of species p created in one reaction of type r , and it can be negative as well as positive. The reaction rate R is proportional to the densities of the reacting particles:

$$R = kn_1n_2 \quad (2.4)$$

for two-body reactions, and

$$R = kn_1n_2n_3 \quad (2.5)$$

for three-body reactions. The proportionality constant k is the reaction rate coefficient. Similarly, the rate of spontaneous decay processes is

$$R = kn , \quad (2.6)$$

where k is the decay frequency.

The transport equations (2.1) and (2.2) require the input of reaction rate coefficients k and transport coefficients μ and D . In general these quantities depend on the energy distribution of the considered particles. We use the following approximations concerning these dependencies:

We assume that the charged particle transport coefficients satisfy the Einstein relation

$$D = \frac{k_B T \mu}{e} , \quad (2.7)$$

where k_B is the Boltzmann constant, e is the elementary charge, and T is the particle temperature, corresponding to the energy of the random particle motion.

For ions we use the local field approximation, which assumes a direct relation between the particle energy distribution and the electric field. Transport and rate coefficients are regarded as functions of the electric field:

$$\mu = \mu(E), \quad D = D(E), \quad k = k(E). \quad (2.8)$$

These relations can be found in the literature as results of experiments and classical theories. In particular, the ion diffusion coefficients are found from the mobilities by the Einstein relation (2.7), in which the ion temperature is related to the electric field by [Ell76, Ell84]

$$k_B T = k_B T_g + \frac{m + m_g}{5m + 3m_g} m_g (\mu E)^2 , \quad (2.9)$$

where T_g is the gas temperature and m and m_g are the ion and gas particle mass, respectively.

For electrons however, the local field approximation often leads to unsatisfactory modeling results, as a result of the poor energy transfer in electron-neutral collisions (due to the huge mass difference). Therefore, rather than using the relations (2.8), we assume the electron transport coefficients and the rate coefficients of electron impact reactions to be functions of the electron mean energy, as in Refs. [Pas93, Boe95]:

$$\mu_e = \mu_e(\bar{\epsilon}), \quad D_e = D_e(\bar{\epsilon}), \quad k = k(\bar{\epsilon}), \quad (2.10)$$

where the subscript e refers to electrons, and the electron mean energy $\bar{\epsilon}$ results from an energy balance equation

$$\frac{\partial n_\epsilon}{\partial t} + \nabla \cdot \Gamma_\epsilon = S_\epsilon , \quad (2.11)$$

which has the form of a continuity equation for electron energy. In this equation n_e is the electron energy density

$$n_e = n_e \bar{\epsilon}, \quad (2.12)$$

and Γ_ϵ is the electron energy flux

$$\Gamma_\epsilon = \frac{5}{3} \bar{\epsilon} \Gamma_e + \mathbf{q}, \quad (2.13)$$

where \mathbf{q} is the heat flux, which we assume to be proportional to the gradient of the electron mean energy according to [Rai91]

$$\mathbf{q} = -\frac{5}{3} n_e D_e \nabla \bar{\epsilon}. \quad (2.14)$$

Substitution of equation (2.14) and the drift-diffusion expression (2.2) for Γ_e casts equation (2.13) into the form of a drift-diffusion equation for electron energy

$$\Gamma_\epsilon = -\frac{5}{3} \mu_e \mathbf{E} n_e - \frac{5}{3} D_e \nabla n_e. \quad (2.15)$$

The source term for electron energy is given by

$$S_\epsilon = -e \Gamma_e \cdot \mathbf{E} - n_e \sum_r \bar{\epsilon}_r k_r n_r, \quad (2.16)$$

where the two terms represent heating by the electric field and energy loss in collisions, respectively. The summation in the loss term is only over the electron impact reactions, with n_r the density of the target particles and $\bar{\epsilon}_r$ the threshold energy. Energy loss due to elastic collisions is included in this term by using an imaginary threshold energy of 1 eV in combination with an effective rate coefficient.

The functions (2.10) are obtained from cross sections, assuming a Maxwellian electron energy distribution function, or – which usually gives better results - using the electron energy distribution function resulting from uniform-field Monte-Carlo or Boltzmann calculations. In the above equations, the electron mean energy is assumed to result mainly from random motion, so that it is consistent to use

$$k_B T_e = \frac{2}{3} \bar{\epsilon} \quad (2.17)$$

with the Einstein relation (2.7) to find the electron diffusion coefficient.

Finally, the electric field depends on the space charge density according to Poisson's equation

$$\nabla \cdot (\epsilon \mathbf{E}) = -\nabla \cdot (\epsilon \nabla V) = \rho, \quad (2.18)$$

where ϵ is the dielectric permittivity, V the electrostatic potential, and ρ the space charge density

$$\rho = \sum_p q_p n_p. \quad (2.19)$$

2.3 New boundary conditions for particle transport*

The boundary conditions for the above equations are an essential part of the description of the problem. For the particle transport equations (2.1-2), a variety of

* This section, in slightly altered form, has been published in: G. J. M. Hagelaar, F. J. de Hoog, and G. M. W. Kroesen, "Boundary conditions in fluid models of gas discharges," in *Phys. Rev. E* **62** (1), 1452-1454 (2000).

boundary conditions can be found in the literature. Straightforward boundary conditions, such as $n = 0$ or $\nabla n \cdot \mathbf{n} = 0$ with \mathbf{n} a normal vector, are satisfactory in some cases [Mey90, Sur90, Pas93, Cho95], but do generally fail to fit the physics. In particular, the physical phenomenon of secondary electron emission by the surface, which is essential for many types of discharges, is not described by these conditions. Most authors therefore use a more general approach, imposing expressions for the particle fluxes, which for electrons may include secondary electron emission. For instance, Refs. [Meu95, Boe95, Pun98, Iva99, Vee97] assume the flux to be directed toward the surface according to

$$\Gamma \cdot \mathbf{n} = a \operatorname{sgn}(q) \mu \mathbf{E} \cdot \mathbf{n} n + \frac{1}{4} v_{th} n, \quad (2.20)$$

where \mathbf{n} is the normal vector pointing toward the wall and v_{th} is the thermal velocity

$$v_{th} = \sqrt{\frac{8k_B T}{\pi m}}. \quad (2.21)$$

The number a is set to one if the drift velocity is directed toward the wall and to zero otherwise:

$$a = \begin{cases} 1 & \operatorname{sgn}(q) \mu \mathbf{E} \cdot \mathbf{n} > 0 \\ 0 & \operatorname{sgn}(q) \mu \mathbf{E} \cdot \mathbf{n} \leq 0 \end{cases}. \quad (2.22)$$

In the case of electrons, a flux due to secondary emission is added to the flux defined by equation (2.20):

$$\Gamma_e \cdot \mathbf{n} = -a_e \mu_e \mathbf{E} \cdot \mathbf{n} n_e + \frac{1}{4} v_{th,e} n_e - \sum_p \gamma_p \Gamma_p \cdot \mathbf{n}, \quad (2.23)$$

where the subscript e refers to electrons, and the summation in the last term is over the ion species impinging on the wall. The secondary emission coefficient γ is the average number of electrons emitted per incident ion.

We show here however, that the boundary conditions (2.20) and (2.23) fall short of physical reality in several ways. We propose improved boundary conditions, which can be used instead.

To start with, we discuss the particle flux toward the wall. From kinetic considerations, it follows that under drift-diffusion conditions, the particle flux toward the wall is given by [Mcd64, New48]

$$\Gamma \cdot \mathbf{n} = (1 - r) \left[a \operatorname{sgn}(q) \mu \mathbf{E} \cdot \mathbf{n} n + \frac{1}{4} v_{th} n - \frac{1}{2} D \nabla n \cdot \mathbf{n} \right], \quad (2.24)$$

where r is the fraction of particles reflected by the surface, and a is once again given by equation (2.22). The last two terms represent the diffusion flux, due to the random motion of the particles. The last term, which is wrongly ignored by many authors, e.g. in the boundary condition (2.20), reflects the fact that this random motion flux involves all particles within a certain mean free path from the wall, not just the local particles at the wall. In order to circumvent possible numerical difficulties in accurately evaluating the density gradient in this term, we now rewrite equation (2.24). Imposition of the expression (2.24) as a boundary condition for the drift-diffusion equation (2.2) implies that the following equation must hold at the boundary:

$$\operatorname{sgn}(q) \mu \mathbf{E} \cdot \mathbf{n} n - D \nabla n \cdot \mathbf{n} = (1 - r) \left[a \operatorname{sgn}(q) \mu \mathbf{E} \cdot \mathbf{n} n + \frac{1}{4} v_{th} n - \frac{1}{2} D \nabla n \cdot \mathbf{n} \right]. \quad (2.25)$$

Note that although both members of this equation contain similar terms, their nature is very different: the left member is a continuum expression, which in principle can be

used anywhere in space, but only has physical meaning inside the plasma volume, whereas the right member is a kinetic expression for the flux at the boundary. From equation (2.25) we find an expression to replace the last term in equation (2.24). Substitution of that expression gives

$$\mathbf{\Gamma} \cdot \mathbf{n} = \frac{1-r}{1+r} \left[(2a-1) \text{sgn}(q) \mu \mathbf{E} \cdot \mathbf{n} n + \frac{1}{2} v_{th} n \right]. \quad (2.26)$$

This equation is an appropriate boundary condition for heavy particle species. It has the same structure as the usual condition (2.20), but gives a better physical description. For neutral species ($\mu = 0$), the equation (2.26) corresponds to the diffusion boundary condition derived by Chantry, using the concept of “linear extrapolation length” [Cha87].

In the case of electrons, influx due to secondary electron emission must be taken into account. Simple addition of this influx to the flux toward the wall, as is done in equation (2.23), gives

$$\mathbf{\Gamma}_e \cdot \mathbf{n} = (1-r_e) \left[-a \mu_e \mathbf{E} \cdot \mathbf{n} n_e + \frac{1}{4} v_{th,e} n_e - \frac{1}{2} D_e \nabla n_e \cdot \mathbf{n} \right] - \sum_p \gamma_p \mathbf{\Gamma}_p \cdot \mathbf{n}. \quad (2.27)$$

Equating the drift-diffusion flux, as before, equation (2.27) becomes

$$\mathbf{\Gamma}_e \cdot \mathbf{n} = \frac{1-r_e}{1+r_e} \left[-(2a_e-1) \mu_e \mathbf{E} \cdot \mathbf{n} n_e + \frac{1}{2} v_{th,e} n_e \right] - \frac{2}{1+r_e} \sum_p \gamma_p \mathbf{\Gamma}_p \cdot \mathbf{n}. \quad (2.28)$$

This boundary condition is our counterpart of the common electron condition (2.23). However, as we point out now, both of these boundary conditions lead to an unrealistic artifact: According to these conditions, *all* electrons in front of the surface contribute to the diffusion flux toward the wall, including the electrons emitted by secondary emission. In this way, the diffusion terms in (2.23) and (2.28) introduce an overaccounting of the backscattering of emitted electrons: Several studies [Nag97, Phe99] have demonstrated that in reality, virtually no emitted electrons are scattered back to surface if a high enough electric field ($> 100 \text{ V cm}^{-1} \text{ Torr}^{-1}$) is present, as is typically the case in front of cathode surfaces.

In order to find a more realistic boundary condition for electrons, we distinguish between two electron groups at the wall: α -electrons, coming from the bulk, and γ -electrons, emitted by the surface. Both groups are treated equally and indistinguishably with the drift-diffusion equation, but have different boundary conditions. To the α -electrons we apply the boundary condition (2.26):

$$\mathbf{\Gamma}_\alpha \cdot \mathbf{n} = \frac{1-r_e}{1+r_e} \left[-(2a_e-1) \mu_e \mathbf{E} \cdot \mathbf{n} n_\alpha + \frac{1}{2} v_{th,e} n_\alpha \right], \quad (2.29)$$

where $\mathbf{\Gamma}_\alpha$ and n_α are the flux and density of the α -electrons. In contrast, the γ -electrons do not flow (back) to the wall:

$$\mathbf{\Gamma}_\gamma \cdot \mathbf{n} = -(1-a_e) \sum_p \gamma_p \mathbf{\Gamma}_p \cdot \mathbf{n}, \quad (2.30)$$

where $\mathbf{\Gamma}_\gamma$ is the flux of γ -electrons, and the factor $(1-a_e)$ is included to cancel the flux in case the electric field is directed away from the wall. The sum of the two fluxes (2.29) and (2.30) can be used as a boundary condition for the total electron flux, if we manage to relate the density of the α -electrons in (2.29) to the total electron density. Keeping in mind that $n_\alpha = n_e - n_\gamma$, where n_γ is the density of the γ -electrons, we choose the following approach:

We write expression (2.30) as the boundary condition for the drift-diffusion equation for γ -electrons, in analogy to equation (2.25):

$$-\mu_e \mathbf{E} \cdot \mathbf{n} n_\gamma - D_e \nabla n_\gamma \cdot \mathbf{n} = -(1 - a_e) \sum_p \gamma_p \Gamma_p \cdot \mathbf{n}. \quad (2.31)$$

Secondary electron emission is important mainly where a strong electric field is directed toward the wall. In this case it is justified to neglect the second term in the left member of this equation, which gives us the density of the γ -electrons

$$n_\gamma = (1 - a_e)^p \frac{\sum_p \gamma_p \Gamma_p \cdot \mathbf{n}}{\mu_e \mathbf{E} \cdot \mathbf{n}}. \quad (2.32)$$

Note that this expression may be incorrect if the electric field is small, but in that case n_γ is negligible anyway ($n_\alpha \approx n_e$). Realizing that the ion fluxes Γ_p are largely proportional to \mathbf{E} , we find that

$$n_\gamma \approx (1 - a_e) \frac{1}{\mu_e} \sum_p \gamma_p \frac{1 - r_p}{1 + r_p} \left[(2a_p - 1) \text{sgn}(q_p) + \frac{1}{2} \sqrt{\frac{8(m_p + m_g)m_g}{\pi(5m_p + 3m_g)m_p}} \right] \mu_p n_p. \quad (2.33)$$

For this approximation we used the equations (2.26), (2.21), and (2.9), where we neglected the gas temperature and assumed the electric field to be perpendicular to the wall.

Finally, we obtain the appropriate boundary condition for the total electron flux, by adding the fluxes (2.29) and (2.30) of the two electron groups, and substituting $n_\alpha = n_e - n_\gamma$ and expression (2.32):

$$\Gamma_e \cdot \mathbf{n} = \frac{1 - r_e}{1 + r_e} \left[-(2a_e - 1) \mu_e \mathbf{E} \cdot \mathbf{n} n_e + \frac{1}{2} v_{th,e} n_e - \frac{1}{2} v_{th,e} n_\gamma \right] - \frac{2}{1 + r_e} (1 - a_e) \sum_p \gamma_p \Gamma_p \cdot \mathbf{n}, \quad (2.34)$$

where n_γ is once again given by (2.32) or by the numerically more convenient expression (2.33). This boundary condition is similar to the boundary condition (2.28), except for the term containing n_γ , which provides a correction for the directed motion of the emitted electrons. Due to this term, the boundary condition automatically switches between the limit (2.30) for high fields toward the wall, and the limit (2.29) for low fields or fields directed from the wall.

In order to demonstrate the effect of the correction term, we simulated a DC discharge in an imaginary two-dimensional rectangular geometry, with one cathode wall and three anode walls. The geometry is represented in Fig. 2.1. The discharge gas is helium, only two particle species are taken into account, electrons and helium ions. The secondary emission coefficient of the ions is assumed to be $\gamma = 0.20$. We calculated the steady state solution of the transport equations, using (2.34) as the boundary condition for electrons. It turned out that the correction term almost entirely cancelled the diffusion flux (back) toward the cathode: $n_\gamma > 0.98 n_e$ all over the cathode surface, so that $\Gamma_e \cdot \mathbf{n} \approx \Gamma_\gamma \cdot \mathbf{n}$. At the anode on the other hand, the correction term was of minor importance: $n_\gamma < 0.1 n_e$, which means that nearly all electrons contributed to the diffusion component. We did the same calculation without the correction term, setting $n_\gamma = 0$ everywhere. In this case we found that the electron influx due to secondary emission from the cathode was partially cancelled by diffusion back to the surface, so that $\Gamma_e \cdot \mathbf{n} \approx 0.7 \Gamma_\gamma \cdot \mathbf{n}$ at the cathode. As a result the steady state plasma density was about one order of magnitude lower. This dramatic effect is illustrated by Fig. 2.2, which shows the calculated steady state electron density for the two cases. It

turned out that the unrealistic backscattering flux toward the cathode can be compensated for by artificially increasing the secondary emission coefficient. Using $\gamma = 0.24$ instead of $\gamma = 0.20$ leads to virtually the same plasma density as the corrected boundary condition.

In conclusion, we have pointed out some shortcomings of the commonly used boundary conditions (2.20) and (2.23): First, the diffusion flux to the surface is only partially included. Second, the treatment of secondary electron emission may lead to an unrealistic diffusion flux of emitted electrons back to wall. This artifact necessitates the use of unphysically high secondary emission coefficients. We have presented alternative boundary conditions, where these problems have been solved in an elegant way.

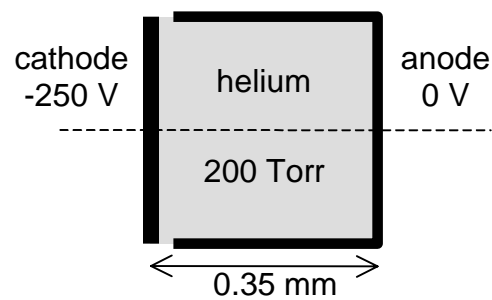


Figure 2.1. Two-dimensional Cartesian DC discharge geometry used for the test calculations.

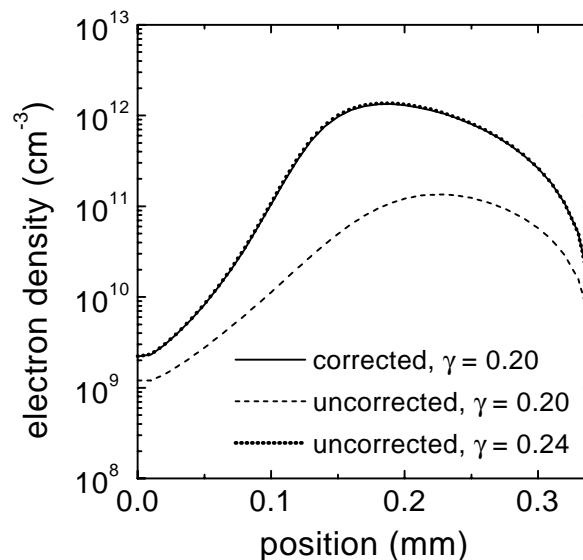


Figure 2.2. Calculated steady state electron densities along the dashed line in the geometry of Fig. 2.1. The cathode and anode are at the left and right hand side of the picture, respectively. The figure compares the boundary condition (2.34), including a correction term for the directed motion of emitted electrons, with the same boundary condition without the correction term.

2.4 The boundary conditions for the system of fluid equations

For the particle transport equations (2.1-2) we use the boundary conditions presented in the previous section, where – because of the lack of data - we set all the reflection coefficients to zero. The boundary condition for the transport of heavy species reads

$$\Gamma_p \cdot \mathbf{n} = (2a_p - 1) \text{sgn}(q_p) \mu_p \mathbf{E} \cdot \mathbf{n} n_p + \frac{1}{2} v_{th,p} n_p. \quad (2.35)$$

For electrons we apply

$$\Gamma_e \cdot \mathbf{n} = -(2a_e - 1) \mu_e \mathbf{E} \cdot \mathbf{n} n_e + \frac{1}{2} v_{th,e} n_e - \frac{1}{2} v_{th,e} n_\gamma - 2(1 - a_e) \sum_p \gamma_p \Gamma_p \cdot \mathbf{n}, \quad (2.36)$$

where

$$n_\gamma = (1 - a_e) \frac{1}{\mu_e} \sum_p \gamma_p \left[(2a_p - 1) \text{sgn}(q_p) + \frac{1}{2} \sqrt{\frac{8(m_p + m_g)m_g}{\pi(5m_p + 3m_g)m_p}} \right] \mu_p n_p. \quad (2.37)$$

For the electron energy transport equations (2.11) and (2.15), we use a boundary condition that is consistent with the boundary condition for electron transport:

$$\Gamma_\varepsilon \cdot \mathbf{n} = -(2a_e - 1) \frac{5}{3} \mu_e \mathbf{E} \cdot \mathbf{n} n_\varepsilon + \frac{2}{3} v_{th,e} n_\varepsilon - \frac{2}{3} v_{th,e} n_{\varepsilon,\gamma} - 2(1 - a_e) \sum_p \gamma_p \bar{\varepsilon}_p \Gamma_p \cdot \mathbf{n}, \quad (2.38)$$

where

$$n_{\varepsilon,\gamma} = (1 - a_e) \frac{1}{\mu_e} \sum_p \gamma_p \bar{\varepsilon}_p \left[(2a_p - 1) \text{sgn}(q_p) + \frac{1}{2} \sqrt{\frac{8(m_p + m_g)m_g}{\pi(5m_p + 3m_g)m_p}} \right] \mu_p n_p, \quad (2.39)$$

and $\bar{\varepsilon}_p$ is the mean initial energy of electrons emitted by incidence of species p .

The electrode potentials are boundary conditions for Poisson's equation. Dielectric materials surrounding the discharge gas do not naturally impose boundary conditions for the electric potential or field, so that it is necessary to solve Poisson's equation in the entire dielectric surroundings of the plasma. The effect of surface charge on top of a dielectric wall is described by Gauss's law

$$\varepsilon_{\text{wall}} \mathbf{E}_{\text{wall}} \cdot \mathbf{n} - \varepsilon_0 \mathbf{E}_{\text{gas}} \cdot \mathbf{n} = \sigma, \quad (2.40)$$

where \mathbf{E}_{wall} and \mathbf{E}_{gas} are the electric fields at the surface, respectively inside and outside the dielectric material. The surface charge density σ results from discharge currents striking the wall. We assume that this charge does not diffuse along the surface, but stays in the very spot it is deposited by the discharge:

$$\sigma = \int \mathbf{j} \cdot \mathbf{n} dt, \quad (2.41)$$

where \mathbf{j} is the plasma current density

$$\mathbf{j} = \sum_p q_p \Gamma_p. \quad (2.42)$$

The current through an electrode is given by

$$I = \iint_{\text{electrode surface}} \left(\mathbf{j} \cdot \mathbf{n} - \varepsilon_0 \frac{\partial}{\partial t} \mathbf{E} \cdot \mathbf{n} \right) d^2S. \quad (2.43)$$

The second term of this equation is the displacement current; it corresponds to changes in total amount of charge present at the surface of the electrode. An external electric circuit, involving back-coupling from the discharge current to the electrode voltage, is not included in the model: the electrode potentials are imposed at all time.

2.5 Input data for the simulation of PALC discharges*

The reactions taken into account in the fluid simulation of PALC discharges are listed in Table 2.1. This reaction scheme has been designed to describe the electrical behavior of microdischarges in pure helium and helium-hydrogen mixtures with a small percentage of hydrogen (< 5%). Since all the important metastable helium states – $\text{He}(2^3S)$, $\text{He}(2^1S)$, and $\text{He}_2(2s^3\Sigma_u)$ – participate in similar reactions with very similar rate coefficients, we have grouped them together into one species He^* . Highly vibrationally excited hydrogen molecules ($v>6$) are treated as one separate species $\text{H}_2(v'')$.

Table 2.1. Reactions in helium-hydrogen mixtures. The second column gives the mean electron energy lost in the reaction.

#	Reaction	Energy (eV)	Rate coefficient	Ref.
excitation				
R1	$e + \text{H}_2 \rightarrow e + 2\text{H}$	11.7	b, Fig. 2.4(f)	[Bol96]
R2	$e + \text{H}_2 \rightarrow e + \text{H}_2(v'')$	12.0	b, Fig. 2.4(e)	[Bol96]
R3	$e + \text{He} \rightarrow e + \text{He}^*$	20.215	b, Fig. 2.4(a)	[Bol96]
ionization by electrons				
R4	$e + \text{H}_2 \rightarrow 2e + \text{H}_2^+$	15.4	b, Fig. 2.4(d)	[Bol96]
R5	$e + \text{He} \rightarrow 2e + \text{He}^+$	24.58	b, Fig. 2.4(c)	[Bol96]
R6	$e + \text{He}^* \rightarrow 2e + \text{He}^+$	4.365	b, Fig. 2.4(b)	[Bol96]
ionization by excited atoms				
R7	$\text{He}^* + \text{H}_2 \rightarrow e + \text{H}_2^+ + \text{He}$	-4.815	$3.2 \times 10^{-11} \text{ cm}^3 \text{ s}^{-1}$	[Mar89]
R8	$\text{He}^* + \text{H} \rightarrow e + \text{H}^+ + \text{He}$	-6.615	$1.1 \times 10^{-9} \text{ cm}^3 \text{ s}^{-1}$	[Mot85]
R9	$\text{He}^* + \text{He}^* \rightarrow e^* + \text{He}^+ + \text{He}$	-15.0	$8.7 \times 10^{-10} \text{ cm}^3 \text{ s}^{-1}$	[Ste82]
R10	$\text{He}^* + \text{He}^* \rightarrow e^* + \text{He}_2^+$	-17.4	$2.0 \times 10^{-9} \text{ cm}^3 \text{ s}^{-1}$	[Ste82]
ion conversion				
R11	$\text{H}_2^+ + \text{H}_2 \rightarrow \text{H}_3^+ + \text{H}$		$2.1 \times 10^{-9} \text{ cm}^3 \text{ s}^{-1}$	[Has99]
R12	$\text{H}^+ + 2\text{H}_2 \rightarrow \text{H}_3^+ + \text{H}_2$		$3.1 \times 10^{-29} \text{ cm}^6 \text{ s}^{-1}$	[Has99]
R13	$\text{He}^+ + 2\text{He} \rightarrow \text{He}_2^+ + \text{He}$		$1.1 \times 10^{-31} \text{ cm}^6 \text{ s}^{-1}$	[Joh80]
R14	$\text{He}_2^+ + \text{H}_2 \rightarrow \text{H}_2^+ + 2\text{He}$		$4.1 \times 10^{-10} \text{ cm}^3 \text{ s}^{-1}$	[Col78]
recombination				
R15	$e + \text{H}_3^+ \rightarrow \text{H} + \text{H} + \text{H}$	0	b, Fig. 2.4(g)	[Bol96]
R16	$e + \text{H}_3^+ \rightarrow \text{H}_2(v'') + \text{H}$	0	b, Fig. 2.4(h)	[Bol96]
R17	$\text{H}^- + \text{H}_3^+ \rightarrow 2\text{H}_2$		$2 \times 10^{-7} \text{ cm}^3 \text{ s}^{-1}$	[Bac81]
de-excitation				
R18	$e + \text{He}^* \rightarrow e^* + \text{He}$	-20.215	$2.9 \times 10^{-9} \text{ cm}^3 \text{ s}^{-1}$	[Ste82]
electron attachment				
R19	$e + \text{H}_2(v'') \rightarrow \text{H}^- + \text{H}$	0	b, Fig. 2.4(i)	[Bol96]
electron detachment				
R20	$\text{H}^- + \text{H} \rightarrow e + \text{H}_2$	0	$7.6 \times 10^{-11} \text{ cm}^3 \text{ s}^{-1}$	[Has99]

* This section, in slightly altered form, has been published in: G. J. M. Hagelaar, G. M. W. Kroesen, U. van Slooten, and H. Schreuders, "Modeling of the microdischarges in plasma addressed liquid crystal displays," J. Appl. Phys. **88** (5), 2252-2262 (2000).

The electron mobility and the rate coefficients of the electron impact reactions are obtained with the Boltzmann code BOLSIG [Bol96], which calculates the electron energy distribution in uniform electric fields, taking into account a comprehensive set of cross sections. Figs. 2.3 and 2.4 show these coefficients for a mixture of 97% helium and 3% hydrogen; for other mixing ratios they are slightly different. The mobilities and diffusion coefficients of all heavy species are assumed to be determined merely by the helium gas. Ion mobilities are shown in Fig. 2.5. The diffusion coefficients of the neutral species are all taken from Ref. [Gri97]: $D \times p = 4.5 \times 10^2 \text{ cm}^2 \text{ Torr s}^{-1}$ for He^* , $D \times p = 2.1 \times 10^3 \text{ cm}^2 \text{ Torr s}^{-1}$ for H, and $D \times p = 1.2 \times 10^3 \text{ cm}^2 \text{ Torr s}^{-1}$ for $\text{H}_2(v'')$, where p is the gas pressure.

We use constant secondary electron emission coefficients: 0.2 for helium ions and 0.01 for hydrogen ions. [Mcd64] Possible dependence of the secondary emission coefficients on the reduced electric field in front of the surface is not considered because of the ambiguity in the published data on this topic. Most of the field dependence reported in the literature is related to the backscattering of emitted electrons. As follows from our discussion in Section 2.3, ambiguity arises when such field-dependent secondary emission coefficients are combined with a fluid boundary condition for electron transport. Secondary electron emission by neutral species is neglected. The mean initial energy is taken to be 5 eV for the secondary electrons emitted by helium ions [Mcd64] and 1 eV for those emitted by hydrogen ions.

The metastable-metastable ionization processes R9 and R10 produce electrons at 15 – 20 eV of energy, which is not enough to excite or ionize helium atoms, but at the same time too much to be efficiently lost in elastic collisions. It is suggested in Ref. [Ilc97] and proven in Chapter 6 of this thesis that these electrons are not thermalized and treated incorrectly by the transport and rate coefficients calculated with BOLSIG [Bol96]. In pure helium, where metastable-metastable ionization plays an important role, we consider them as a separate species: e^* , mono-energetic electrons of 15 eV, which do not take part in any reaction. This approach is supported by the Monte-Carlo calculations presented in Chapter 6. For the mobility of these electrons we use a constant value of $\mu \times p = 6.8 \times 10^5 \text{ cm}^2 \text{ Torr V}^{-1} \text{ s}^{-1}$, the diffusion coefficient is taken to be $D \times p = 6.8 \times 10^6 \text{ cm}^2 \text{ Torr s}^{-1}$. In helium-hydrogen mixtures we use only one electron group.

The importance of H^- is unclear. The reactions R2 and R19 only represent the most probable mechanism for its production. Details and reliable values for rate coefficients are not known. The rate coefficient for dissociative attachment R19 increases by orders of magnitude with increasing vibrational level of H_2 ; [His91] only states $\text{H}_2(v > 6)$ may contribute significantly to the production of H^- . It has been suggested that these high vibrational levels are populated mainly through radiative decay of higher singlet electronic states excited by energetic electrons. [Bac81, Dem88, Has99] Since the exact vibrational distribution resulting from these processes is unknown, the effective rate coefficient for reaction R19 is no more than a rough estimate. The rate coefficient of reaction R2 is taken to be proportional to the excitation rates of $\text{H}_2(C^1\Pi_u)$ and $\text{H}_2(B^1\Sigma_u^+)$; [Bac81, Dem88] the proportionality constant however is only a conjecture. In view of the large uncertainties concerning the production of H^- , we prefer to omit the species H^- and $\text{H}(v'')$, as well as the reactions R2, R17, R19, and R20, from the reaction scheme, unless there is evidence for the importance of H^- in PALC discharges.

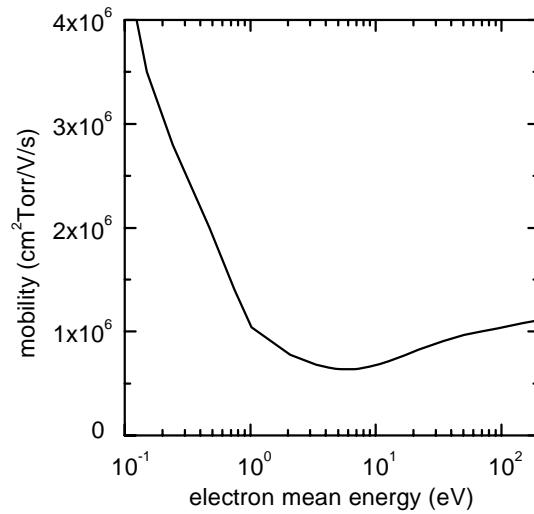


Figure 2.3. Electron mobility in 97% helium – 3% hydrogen. The data come from Ref. [Mcd64] (< 1 eV) and a BOLSIG²⁹ calculation (> 1 eV).

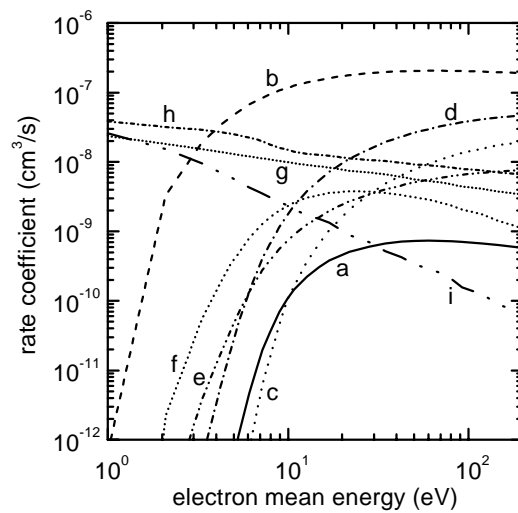


Figure 2.4. Rate coefficients of electron impact reactions in 97% helium – 3% hydrogen, as calculated with BOLSIG [Bol96]. (a) total excitation $\text{He}^*(2^3S)$ and $\text{He}^*(2^1S)$ (R3), (b) ionization from He^* (R6), (c) direct ionization He (R5), (d) direct ionization H_2 (R4), (e) $20\% \times$ total excitation $\text{H}_2(C^1\Pi_u)$ and $\text{H}_2(B^1\Sigma_u^+)$ (R2), (f) dissociation H_2 (R1), (g) recombination H_3^+ (R15), (h) recombination H_3^+ (R16), (i) dissociative attachment (R19).

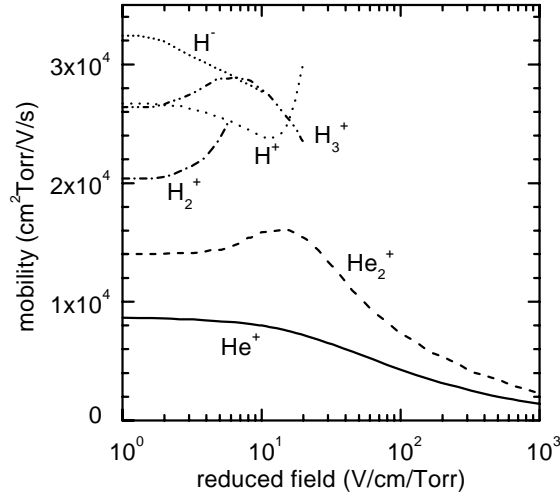


Figure 2.5. Ion mobilities in helium. The data are taken from Ref. [Ell76] (for He^+ , He_2^+ , H_2^+ , H_3^+ , and H^+), Ref. [Ell84] (for H^+), and Ref. [Mcf73] (for He_2^+ at high field).

2.6 Input data for the simulation of PDP discharges

Table 2.2 shows the reaction scheme for the simulation of PDP discharges in neon-xenon mixtures. Similar reaction schemes have been reported in the literature, e. g. in Ref. [Meu95]. The scheme is more comprehensive than the PALC scheme, because it has to describe not only the electrical behavior of the discharge but also the mechanisms of UV photon generation; the kinetics of excited neutrals must be described in much greater detail. Of particular interest are the excited xenon states, since these are mainly responsible for UV emission. We have included all excited atomic xenon states, as four different species: The two lowest levels – the metastable $\text{Xe}^*(^3P_2)$ and the resonant $\text{Xe}^*(^3P_1)$ states – are treated as separate species. The other states are grouped into two compound species: Xe^{**} represents the states indicated by the Racah notations $6s'$, $6p$, $5d$, $7s$, as in Ref. [Meu95], and Xe^{***} are all the other excited states.

The electron mobility and the rate coefficients of the electron impact reactions are obtained by the Boltzmann code described in Ref. [Mue91]; Fig. 2.6 shows the rate coefficients of selected reactions. The mobilities and diffusion coefficients of the neon ions Ne^+ and Ne_2^+ are assumed to be the same as in pure neon, and taken from Ref. [Ell76]. The mobilities of the xenon ion species Xe^+ , Xe_2^+ , and NeXe^+ are obtained from the data in Refs. [Bro69, Ell76, Ell84] using Blanc's law [Bla08]

$$\frac{1}{\mu} = \frac{1-x}{\mu_{\text{Ne}}} + \frac{x}{\mu_{\text{Xe}}}, \quad (2.44)$$

where x is the xenon fraction, and μ_{Ne} and μ_{Xe} are the mobilities in pure neon and in pure xenon, respectively. An analogous expression applies to the diffusion coefficients of these ions. The diffusion coefficients of the neutral species are calculated from a hard-sphere model [Hir54] and Blanc's law; for 5% xenon they are $D \times p = 3.7 \times 10^2 \text{ cm}^2 \text{ Torr s}^{-1}$ for neon atoms, $D \times p = 1.4 \times 10^2 \text{ cm}^2 \text{ Torr s}^{-1}$ for xenon atoms, and $D \times p = 85 \text{ cm}^2 \text{ Torr s}^{-1}$ for xenon dimers.

Table 2.2. Reactions in neon-xenon mixtures. The second column gives the mean electron energy lost in the reaction.

#	Reaction	Energy (eV)	Rate coefficient	Ref.
excitation				
R21	$e + \text{Xe} \rightarrow e + \text{Xe}^*(^3P_2)$	8.32	b, Fig. 2.6(g)	[Pue91]
R22	$e + \text{Xe} \rightarrow e + \text{Xe}^*(^3P_1)$	8.44	b, Fig. 2.6(f)	[Pue91]
R23	$e + \text{Xe} \rightarrow e + \text{Xe}^{**}$	9.58	b, Fig. 2.6(d)	[Fel68]
R24	$e + \text{Xe} \rightarrow e + \text{Xe}^{***}$	11	b, Fig. 2.6(e)	[Kle99]
R25	$e + \text{Xe}^*(^3P_2) \rightarrow e + \text{Xe}^{**}$	1.26	b, Fig. 2.6(b)	[Hym81]
R26	$e + \text{Xe}^*(^3P_1) \rightarrow e + \text{Xe}^{**}$	1.14	b, Fig. 2.6(a)	[Hym81]
R27	$e + \text{Ne} \rightarrow e + \text{Ne}^*$	16.61	b, Fig. 2.6(i)	[Reg84]
R28	$e + \text{Ne} \rightarrow e + \text{Ne}^{**}$	18.38	b, Fig. 2.6(j)	[Reg84]
R29	$e + \text{Ne}^* \rightarrow e + \text{Ne}^{**}$	1.77	b	[Hym79]
R30	$e + \text{Xe}_2(^3\Sigma_u^+) \rightarrow e + \text{Xe}_2(^1\Sigma_u^+)$	0.06	b	[Eck88]
R31	$e + \text{Xe}_2(^3\Sigma_u^+) \rightarrow e + \text{Xe}^*(^3P_2) + \text{Xe}$	1.12	b	[Eck88]
R32	$e + \text{Xe}_2(^3\Sigma_u^+) \rightarrow e + \text{Xe}_2^{**}$	1.8	b	[Eck88]
ionization by electrons				
R33	$e + \text{Xe} \rightarrow 2e + \text{Xe}^+$	12.12	b, Fig. 2.6(c)	[Rap65]
R34	$e + \text{Xe}^*(^3P_2) \rightarrow 2e + \text{Xe}^+$	3.8	b, Fig. 2.6(k)	[Hym79]
R35	$e + \text{Xe}^*(^3P_1) \rightarrow 2e + \text{Xe}^+$	3.68	b	[Hym79]
R36	$e + \text{Xe}^{**} \rightarrow 2e + \text{Xe}^+$	2.54	b	[Hym79]
R37	$e + \text{Ne} \rightarrow 2e + \text{Ne}^+$	21.56	b, Fig. 2.6(h)	[Rap65]
R38	$e + \text{Ne}^* \rightarrow 2e + \text{Ne}^+$	4.95	b	[Hym79]
R39	$e + \text{Ne}^{**} \rightarrow 2e + \text{Ne}^+$	3.18	b	[Hym79]
ionization by excited atoms				
R40	$\text{Xe}^*(^3P_2) + \text{Xe}^*(^3P_2) \rightarrow e + \text{Xe}^+ + \text{Xe}$	-4.52	$5 \times 10^{-10} \text{ cm}^3 \text{ s}^{-1}$	[Eck88]
R41	$\text{Xe}^*(^3P_2) + \text{Xe}^*(^3P_1) \rightarrow e + \text{Xe}^+ + \text{Xe}$	-4.64	$1 \times 10^{-9} \text{ cm}^3 \text{ s}^{-1}$	[Eck88]
R42	$\text{Xe}^*(^3P_1) + \text{Xe}^*(^3P_1) \rightarrow e + \text{Xe}^+ + \text{Xe}$	-4.76	$5 \times 10^{-10} \text{ cm}^3 \text{ s}^{-1}$	[Eck88]
R43	$\text{Ne}^* + \text{Xe} \rightarrow e + \text{Xe}^+ + \text{Ne}$	-4.49	$7.5 \times 10^{-11} \text{ cm}^3 \text{ s}^{-1}$	[Ney70]
R44	$\text{Ne}^* + \text{Xe} \rightarrow e + \text{NeXe}^+$	-4.51	$2.3 \times 10^{-11} \text{ cm}^3 \text{ s}^{-1}$	[Ney70]
R45	$\text{Ne}^{**} + \text{Xe} \rightarrow e + \text{NeXe}^+$	-6.28	$2.3 \times 10^{-11} \text{ cm}^3 \text{ s}^{-1}$	[Ney70]
ion conversion				
R46	$\text{Xe}^+ + 2\text{Xe} \rightarrow \text{Xe}_2^+ + \text{Xe}$		$2.0 \times 10^{-31} \text{ cm}^6 \text{ s}^{-1}$	[Eck88]
R47	$\text{Xe}^+ + \text{Xe} + \text{Ne} \rightarrow \text{Xe}_2^+ + \text{Ne}$		$1.5 \times 10^{-31} \text{ cm}^6 \text{ s}^{-1}$	[Lev81]
R48	$\text{Xe}^+ + 2\text{Ne} \rightarrow \text{NeXe}^+ + \text{Ne}$		$1.5 \times 10^{-31} \text{ cm}^6 \text{ s}^{-1}$	[Lev81]
R49	$\text{Ne}^+ + 2\text{Ne} \rightarrow \text{Ne}_2^+ + \text{Ne}$		$4.4 \times 10^{-32} \text{ cm}^6 \text{ s}^{-1}$	[Hok84]
R50	$\text{Ne}^+ + \text{Ne} + \text{Xe} \rightarrow \text{NeXe}^+ + \text{Ne}$		$1 \times 10^{-31} \text{ cm}^6 \text{ s}^{-1}$	[Lev81]
R51	$\text{Ne}_2^+ + \text{Ne} + \text{Xe} \rightarrow \text{Xe}^+ + 3\text{Ne}$		$4 \times 10^{-30} \text{ cm}^6 \text{ s}^{-1}$	[Hok84]
R52	$\text{NeXe}^+ + \text{Xe} \rightarrow \text{Xe}^+ + \text{Ne} + \text{Xe}$		$5 \times 10^{-10} \text{ cm}^3 \text{ s}^{-1}$	[Meu95]
R53	$\text{NeXe}^+ + \text{Xe} \rightarrow \text{Xe}_2^+ + \text{Ne}$		$5 \times 10^{-12} \text{ cm}^3 \text{ s}^{-1}$	[Meu95]
R54	$e + \text{Xe}_2^+ \rightarrow e + \text{Xe}^+ + \text{Xe}$	0.99	b	[Eck88]
recombination				
R55	$e + \text{Xe}_2^+ \rightarrow \text{Xe}^{**} + \text{Xe}$	0	b	[Bar70]
R56	$e + \text{Ne}_2^+ \rightarrow \text{Ne}^{**} + \text{Ne}$	0	b	[Bar70]
R57	$e + \text{NeXe}^+ \rightarrow \text{Xe}^{**} + \text{Ne}$	0	b	[Bar70]

(continued on the next page)

Table 2.2. (continued)

de-excitation				
R58	$e + \text{Xe}^*(^3P_2) \rightarrow e + \text{Xe}$	-8.32	b	[Pue91]
R59	$e + \text{Xe}^*(^3P_1) \rightarrow e + \text{Xe}$	-8.44	b	[Pue91]
R60	$e + \text{Xe}^{**} \rightarrow e + \text{Xe}^*(^3P_2)$	-1.26	b	[Hym81]
R61	$e + \text{Xe}^{**} \rightarrow e + \text{Xe}^*(^3P_1)$	-1.14	b	[Hym81]
R62	$e + \text{Ne}^{**} \rightarrow e + \text{Ne}^*$	-1.77	b	[Hym79]
R63	$e + \text{Xe}_2(^3\Sigma_u^+) \rightarrow e + 2\text{Xe}$	-7.2	b	[Eck88]
R64	$e + \text{Xe}_2^{**} \rightarrow e + \text{Xe}_2(^3\Sigma_u^+)$	-1.88	b	[Eck88]
R65	$e + \text{Xe}_2^{**} \rightarrow e + \text{Xe}_2(^1\Sigma_u^+)$	-1.8	b	[Eck88]
R66	$e + \text{Xe}_2^{**} \rightarrow e + \text{Xe}_2(O_u^+)$	-0.73	b	[Eck88]
excited neutral kinetics				
R67	$\text{Xe}^*(^3P_2) + \text{Ne} \rightarrow \text{Xe}^*(^3P_1) + \text{Ne}$	$1.6 \times 10^{-16} \text{ cm}^3 \text{ s}^{-1}$		[Meu95]
R68	$\text{Xe}^*(^3P_2) + \text{Xe} \rightarrow \text{Xe}^*(^3P_1) + \text{Xe}$	$1.3 \times 10^{-16} \text{ cm}^3 \text{ s}^{-1}$		[Meu95]
R69	$\text{Xe}^*(^3P_1) + \text{Ne} \rightarrow \text{Xe}^*(^3P_2) + \text{Ne}$	$3.1 \times 10^{-14} \text{ cm}^3 \text{ s}^{-1}$		[Meu95]
R70	$\text{Xe}^*(^3P_2) + \text{Xe} \rightarrow \text{Xe}^*(^3P_1) + \text{Xe}$	$2.2 \times 10^{-14} \text{ cm}^3 \text{ s}^{-1}$		[Meu95]
R71	$\text{Xe}^{**} + \text{Ne} \rightarrow \text{Xe}^*(^3P_2) + \text{Ne}$	$2 \times 10^{-12} \text{ cm}^3 \text{ s}^{-1}$		[Meu95]
R72	$\text{Xe}^{**} + \text{Ne} \rightarrow \text{Xe}^*(^3P_1) + \text{Ne}$	$2 \times 10^{-12} \text{ cm}^3 \text{ s}^{-1}$		[Meu95]
R73	$\text{Xe}^{**} + \text{Xe} \rightarrow \text{Xe}^*(^3P_2) + \text{Xe}$	$1 \times 10^{-10} \text{ cm}^3 \text{ s}^{-1}$		[Meu95]
R74	$\text{Xe}^{**} + \text{Xe} \rightarrow \text{Xe}^*(^3P_1) + \text{Xe}$	$1 \times 10^{-10} \text{ cm}^3 \text{ s}^{-1}$		[Meu95]
R75	$\text{Xe}^*(^3P_2) + \text{Xe} + \text{Ne} \rightarrow \text{Xe}_2(^3\Sigma_u^+) + \text{Ne}$	$1.4 \times 10^{-32} \text{ cm}^6 \text{ s}^{-1}$		[Meu95]
R76	$\text{Xe}^*(^3P_2) + 2\text{Xe} \rightarrow \text{Xe}_2(^3\Sigma_u^+) + \text{Xe}$	$8.5 \times 10^{-32} \text{ cm}^6 \text{ s}^{-1}$		[Meu95]
R77	$\text{Xe}^*(^3P_1) + \text{Xe} + \text{Ne} \rightarrow \text{Xe}_2(O_u^+) + \text{Ne}$	$4.1 \times 10^{-32} \text{ cm}^6 \text{ s}^{-1}$		[Meu95]
R78	$\text{Xe}^*(^3P_1) + 2\text{Xe} \rightarrow \text{Xe}_2(O_u^+) + \text{Xe}$	$1.6 \times 10^{-31} \text{ cm}^6 \text{ s}^{-1}$		[Meu95]
R79	$\text{Xe}^{**} + 2\text{Xe} \rightarrow \text{Xe}_2^{**} + \text{Xe}$	$5.1 \times 10^{-31} \text{ cm}^6 \text{ s}^{-1}$		[Eck88]
R80	$\text{Xe}_2(O_u^+) + \text{Xe} \rightarrow \text{Xe}_2(^1\Sigma_u^+) + \text{Xe}$	$2.6 \times 10^{-10} \text{ cm}^3 \text{ s}^{-1}$		[Meu95]
spontaneous decay				
R81	$\text{Xe}^*(^3P_1) \rightarrow \text{Xe} + h\nu (147 \text{ nm})$	$2.2 \times 10^6 \text{ s}^{-1}$		[Kle97]
R82	$\text{Xe}^{**} \rightarrow \text{Xe}^*(^3P_2) + h\nu (800 \text{ nm})$	$3 \times 10^7 \text{ s}^{-1}$		[Meu95]
R83	$\text{Xe}^{**} \rightarrow \text{Xe}^*(^3P_1) + h\nu (800 \text{ nm})$	$3 \times 10^7 \text{ s}^{-1}$		[Meu95]
R84	$\text{Xe}^{***} \rightarrow \text{Xe} + h\nu$	$1 \times 10^7 \text{ s}^{-1}$		[Kle99]
R85	$\text{Xe}^{***} \rightarrow \text{Xe}^{**} + h\nu$	$1 \times 10^8 \text{ s}^{-1}$		[Kle99]
R86	$\text{Xe}_2(^3\Sigma_u^+) \rightarrow 2\text{Xe} + h\nu (173 \text{ nm})$	$9 \times 10^6 \text{ s}^{-1}$		[Meu95]
R87	$\text{Xe}_2(^1\Sigma_u^+) \rightarrow 2\text{Xe} + h\nu (173 \text{ nm})$	$1.6 \times 10^8 \text{ s}^{-1}$		[Meu95]
R88	$\text{Xe}_2(O_u^+) \rightarrow 2\text{Xe} + h\nu (150 \text{ nm})$	$5 \times 10^8 \text{ s}^{-1}$		[Meu95]
R89	$\text{Xe}_2^{**} \rightarrow \text{Xe}(^3P_2) + \text{Xe}$	$5 \times 10^7 \text{ s}^{-1}$		[Eck88]
R90	$\text{Xe}_2^{**} \rightarrow \text{Xe}(^3P_1) + \text{Xe}$	$5 \times 10^7 \text{ s}^{-1}$		[Eck88]
R91	$\text{Ne}^{**} \rightarrow \text{Ne}^* + h\nu (600 \text{ nm})$	$3.6 \times 10^7 \text{ s}^{-1}$		[LTI]

The secondary-emission coefficients for ion impact on magnesium-oxide are assumed to be 0.45 for Ne^+ and Ne_2^+ , and 0.001 for Xe^+ , Xe_2^+ , and NeXe^+ , as in Ref. [Pun98a]. The small value for xenon ions is supported by the experimental data of Ref. [Kle99]. Once again we do not consider dependence of γ on E/p , and neglect secondary emission by neutral species. The mean initial energy of the secondary electrons is assumed to be 1 eV.

The resonant state $\text{Xe}^*(^3P_1)$ decays with a natural decay frequency $\nu_0 = 2.89 \times 10^8 \text{ s}^{-1}$ [Ber79]. Under PDP conditions however, the emitted resonance UV photons are many times absorbed by ground state xenon atoms and re-emitted, before

reaching the discharge walls: they are imprisoned. We account for the imprisonment by using an effective frequency for the decay of $\text{Xe}^*(^3P_1)$, which given by [Kle97]

$$v_{\text{eff}} = 5.74 \times 10^{-5} \sqrt{\frac{x+0.0408}{xd}} v_0, \quad (2.45)$$

where x is the xenon fraction, and d is the typical distance in meters from the region of photon generation to the wall. A similar approach is used in Refs. [Meu95, MCG98, Rau99]. Equation (2.45) has been obtained from a fit to the cylinder symmetrical solution of Holstein's equation for radiation transport [Hol51], using data from Ref. [Iga95]. The rate coefficient of reaction R81 in Table 2.2 corresponds to equation (2.45) with $x = 0.05$ and $d = 10^{-4}$ m. The effective decay frequency only gives a very crude description of the imprisonment of the resonance photons. A much better description is given in Chapter 8 of this thesis, by a Monte Carlo model for resonance photons.

In both PALC and PDP discharges molecular ions are formed, such as He_2^+ and Xe_2^+ . References [Gro73] and [Mai75] show that if the energy of these ions exceeds a threshold on the order of 1 eV, collisions with gas atoms may well lead to their dissociation. In Monte Carlo simulations (see Chapter 7 of this thesis) we found that although these ions are stable in low field regions ($<50 \text{ V cm}^{-1} \text{ Torr}^{-1}$), they are massively dissociated in the microdischarge sheaths. Yet the dissociative ion-neutral collisions are not mentioned by other authors in the field of discharge modeling, e. g. in Ref. [Meu95]. The dissociation processes could be included in the fluid model using field dependent rate coefficients. However, such rate coefficients would be no more than conjectures, for lack of accurate experimental data. Moreover, the dissociation reactions are unlikely to have a significant effect on the electrical or the radiative behavior of the discharge, since we assume the same secondary emission coefficient for molecular and atomic ions. We therefore follow Ref. [Meu95] and simply ignore the dissociation of molecular ions.

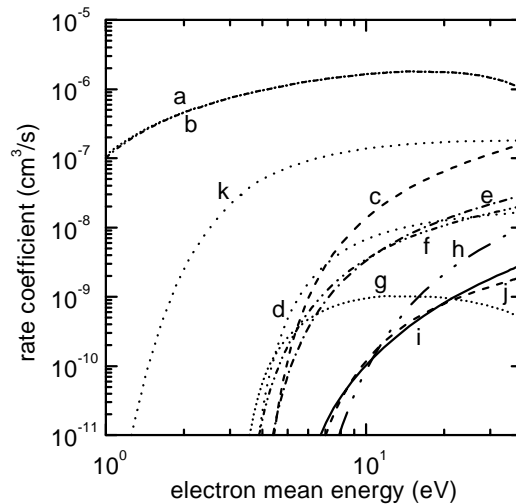


Figure 2.6. Rate coefficients of electron impact reactions in 95% neon – 5% xenon, obtained from [Mue91]. (a) excitation Xe^* from $\text{Xe}^*(^3P_1)$ (R26), (b) excitation Xe^{**} from $\text{Xe}^*(^3P_2)$ (R25), (c) direct ionization Xe (R33), (d) excitation Xe^{**} (R23), (e) excitation Xe^{***} (R24), (f) excitation $\text{Xe}^*(^3P_1)$ (R22), (g) excitation $\text{Xe}^*(^3P_2)$ (R21), (h) direct ionization Ne (R37), (i) excitation Ne^* (R27), (j) excitation Ne^{**} (R28), (k) ionization from $\text{Xe}^*(^3P_2)$ (R34).

Chapter 3

The numerical solution of the fluid equations*

3.1 Introduction

The system of fluid equations presented in the previous chapter is solved numerically, by a computer code, taking into account both time evolution and two spatial dimensions. We solve the equations by the finite difference method [Mor94], where all quantities are represented by their values at a discrete set of points in time and space. Using these values, the derivatives in the equations are approximated by finite differences: the equations are discretized. In this chapter we describe in detail how the equations are discretized and how the discretized equations are solved.

3.2 Time integration of the system of equations

When solving the system of fluid equations, one has to deal with the coupling between the different equations. In this section we demonstrate how this is taken care of in the discretization scheme for the time integration. The words “explicit” and “implicit” will turn out to be the keywords in solving the couplings in the system. Let upper indices refer to a moment in time, and let Δt be a time step, with $t^{k+1} = t^k + \Delta t$. Assume that the values of all quantities are known at a time t^k and are to be calculated at time t^{k+1} . The continuity equations for particles (2.1) and for electron energy (2.11) are discretized in time as follows:

$$\frac{n_p^{k+1} - n_p^k}{\Delta t} - \nabla \cdot \Gamma_p^l = S_p^m, \quad (3.1)$$

where l and m are the time indices pertinent to Γ and S , respectively. The transport term and the source term can be evaluated either at time t^k ($l, m = k$) or at time t^{k+1} ($l, m = k+1$). Evaluation at time t^k is explicit, since all quantities at t^k are already known. This is computationally attractive, but it can lead to fluctuations or even instabilities in the calculation, unless restrictions are applied to the time step Δt . Evaluation at time t^{k+1} must be implicit, since no values are known yet. Implicit treatment does not lead to fluctuations or instabilities, but it can be very hard to accomplish: The coupling between different equations and non-linearities can make implicit evaluations quite cumbersome or impossible. We now write equation (3.1) more precisely as

$$\frac{n_p^{k+1} - n_p^k}{\Delta t} - \nabla \cdot \Gamma_p(n_p^{l_n}, \mathbf{E}^{l_E}, \mu_p^{l_\mu}, D_p^{l_D}) = S_p(n_1^{m_n}, n_2^{m_n}, \dots, k_1^{m_k}, k_2^{m_k}, \dots), \quad (3.2)$$

and discuss in detail the treatment of the different quantities appearing in the transport and source terms of this equation:

* Parts of this chapter have been published in: G. J. M. Hagelaar and G. M. W. Kroesen, “Speeding up fluid models for gas discharges by implicit treatment of the electron energy source term,” J. Comp. Phys. **59**, 1-12 (2000).

The density in the transport term is always handled implicitly: $l_n = k+1$, because explicit treatment ($l_n = k$) would lead to very severe time step restrictions due to a fundamental necessary condition for the convergence of difference methods, known as the Courant-Friedrichs-Lewy (CFL) condition [Roa76, Mor94].

The evaluation of the electric field in the transport term has drawn the attention of many authors in the field of discharge modeling. If the electric field in the transport term is treated explicitly ($l_E = k$), as is done in conventional discharge models, the following time step condition must be applied [Bar87]:

$$\Delta t < \frac{\epsilon_0}{\sum_p |q_p| \mu_p n_p}, \quad (3.3)$$

in order to avoid numerical instabilities. The electric field at t^{k+1} can then be calculated straightforwardly after the calculation of the densities from

$$\nabla \cdot (\epsilon \mathbf{E}^{k+1}) = \sum_p q_p n_p^{k+1}. \quad (3.4)$$

The constraint (3.3) can be very prohibitive, especially for high plasma densities ($>10^9 \text{ cm}^{-3}$). Implicit evaluation of \mathbf{E} ($l_E = k+1$) circumvents this time step restriction, but is numerically unattractive, since it implies solving all the continuity equations (2.1) and Poisson's equation (2.18) at the same time. In 1-D models fully implicit techniques have been successfully applied [Nit94, Boe95a], but for multidimensional problems these become too cumbersome. However, it can be shown that, in order to avoid restriction (3.3), a strictly implicit evaluation of \mathbf{E} is not necessary: a so-called semi-implicit treatment [Ven93, Ven94, Lap95] will also ensure stability. In this case, Poisson's equation is solved before the continuity equations. Since the space charge density at time t^{k+1} is not known yet, an estimate is used:

$$\nabla \cdot (\epsilon \mathbf{E}^{k+1}) = \sum_p q_p \tilde{n}_p^{k+1}, \quad (3.5)$$

where \tilde{n}_p^{k+1} is an estimate for n_p^{k+1} , arising from the continuity equation (3.2) with $l_n = l_\mu = l_D = m_n = m_k = k$ and only $l_E = k+1$:

$$\tilde{n}_p^{k+1} = n_p^k + \Delta t \nabla \cdot \Gamma_p(n_p^k, \mathbf{E}^{k+1}, \mu_p^k, D_p^k). \quad (3.6)$$

Note that the source term S_p has been omitted, since it does not create any space charge: after substitution in equation (3.4), all source terms would cancel. Using this semi-implicit technique, the time step can be several orders of magnitude larger than the time step given by constraint (3.3), thus giving a tremendous speedup of the calculation.

Transport coefficients and particle source terms are mostly evaluated explicitly ($l_\mu = l_D = m_n = m_k = k$). Fully implicit treatment of all densities in the particle source terms ($m_n = k+1$) is hardly feasible. Furthermore implicit evaluation of transport and rate coefficients ($l_\mu = l_D = m_k = k+1$) is problematic since they are arbitrary functions of the electric field (2.8) or the mean electron energy (2.10), read from lookup tables. For spontaneous decay processes with a high decay frequency, the density is better evaluated implicitly ($m_n = k+1$).

3.3 Implicit treatment of the electron energy source term

Using the semi-implicit treatment of the electric field in the drift-diffusion flux, the particle transport equations can be solved reasonably well. However, it turns out

that the solution of the electron energy balance equation becomes limiting for the time step. Small oscillations in the solution of this equation are amplified and spread rapidly throughout the whole system of equations due to the strong dependence of rate coefficients and electron diffusion coefficient on the electron mean energy. A typical behavior is depicted in Fig. 3.1. It has been stated previously that this problem can be avoided by evaluating the source term for electron energy implicitly, rather than applying the conventional explicit treatment. For example, Ref. [Lap95] reports a semi-implicit treatment of the inelastic energy losses, be it for a different type of energy equation. We present here an implicit technique for the entire source term (2.16) of the electron energy equation (2.11), that is, including the electron heating term.

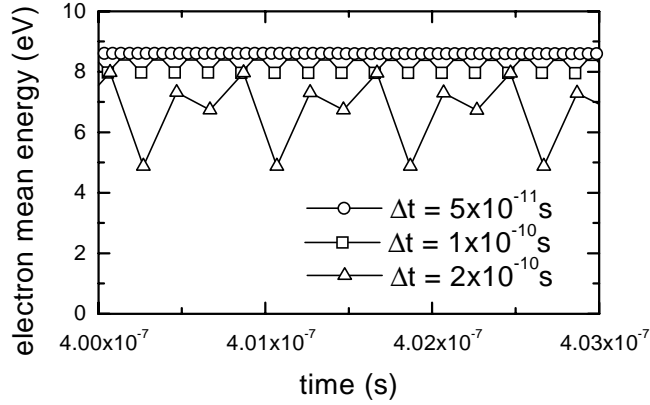


Figure 3.1. Oscillations in the electron mean energy at one position in a simulation of a DC microdischarge, for different values of the time step Δt .

The electron energy source term has a different form than the particle source terms:

$$S_{\varepsilon} = -e\mathbf{E}^{m_{\varepsilon}} \cdot \mathbf{\Gamma}_e^{m_{\varepsilon}}(n_e^{m_{\varepsilon}}, \mathbf{E}^{m_{\varepsilon}}, \mu_e^{m_{\varepsilon}}, D_e^{m_{\varepsilon}}) - n_e^{m_{\varepsilon}} \sum_r \bar{\varepsilon}_r k_r^{m_{\varepsilon}} n_r^{m_{\varepsilon}}. \quad (3.7)$$

In this source term the electric field and the electron density can be taken at time t^k without any problem ($m_{\varepsilon} = m_n = k$), but an explicit evaluation of the electron mobility, electron diffusion coefficient, and especially of the reaction rate coefficients, ($m_{\varepsilon} = m_{\mu} = m_D = m_k = k$) can easily cause and amplify fluctuations. We show now how these quantities can be evaluated implicitly ($m_{\varepsilon} = m_{\mu} = m_D = m_k = k+1$). First, we linearize the energy source term with respect to the electron mobility, electron diffusion coefficient, and rate coefficients:

$$S_{\varepsilon} = -e\mathbf{E}^k \cdot \mathbf{\Gamma}_e^k - n_e^k \sum_r \bar{\varepsilon}_r k_r^k n_r^k - e\mathbf{E}^k \cdot \left(\frac{\partial \mathbf{\Gamma}_e}{\partial \mu_e} \right)^k (\mu_e^{k+1} - \mu_e^k) - e\mathbf{E}^k \cdot \left(\frac{\partial \mathbf{\Gamma}_e}{\partial D_e} \right)^k (D_e^{k+1} - D_e^k) - n_e^k \sum_r \bar{\varepsilon}_r (k_r^{k+1} - k_r^k) n_r^k. \quad (3.8)$$

Then, we linearize the dependencies of these quantities on the mean electron energy:

$$\mu_e^{k+1} = \mu_e^k + \left(\frac{\partial \mu_e}{\partial \bar{\varepsilon}} \right)^k (\bar{\varepsilon}^{k+1} - \bar{\varepsilon}^k), \quad (3.9)$$

and analogous expressions for D_e^{k+1} and k_r^{k+1} . Note that the energy derivatives of μ_e , D_e , and k_r are easily evaluated from the look-up-tables. Finally, we use

$$\begin{aligned}\bar{\varepsilon}^{k+1} &= \bar{\varepsilon}^k + \left(\frac{\partial \bar{\varepsilon}}{\partial n_e}\right)^k (n_e^{k+1} - n_e^k) + \left(\frac{\partial \bar{\varepsilon}}{\partial n_e}\right)^k (n_e^{k+1} - n_e^k) \\ &= \bar{\varepsilon}^k + \frac{1}{n_e^k} (n_e^{k+1} - n_e^k) - \frac{n_e^k}{(n_e^k)^2} (n_e^{k+1} - n_e^k) \\ &= \bar{\varepsilon}^k + \frac{1}{n_e^k} (n_e^{k+1} - n_e^{k+1} \bar{\varepsilon}^k).\end{aligned}\quad (3.10)$$

Substitution of these expressions into equation (3.8) yields

$$\begin{aligned}S_\varepsilon &= -e\mathbf{E}^k \cdot \Gamma_e^k - n_e^k \sum_r \varepsilon_r k_r^k n_r^k - \left[\frac{e}{n_e^k} \mathbf{E}^k \cdot \left(\frac{\partial \Gamma_e}{\partial \mu_e} \right)^k \left(\frac{\partial \mu_e}{\partial \bar{\varepsilon}} \right)^k \right. \\ &\quad \left. + \frac{e}{n_e^k} \mathbf{E}^k \cdot \left(\frac{\partial \Gamma_e}{\partial D_e} \right)^k \left(\frac{\partial D_e}{\partial \bar{\varepsilon}} \right)^k + \sum_r \bar{\varepsilon}_r \left(\frac{\partial k_r}{\partial \bar{\varepsilon}} \right)^k n_r^k \right] (n_e^{k+1} - n_e^{k+1} \bar{\varepsilon}^k).\end{aligned}\quad (3.11)$$

The last term on the right hand side provides an implicit correction of the energy source term for changes in the electron mean energy, which prevents oscillations in the solution of the energy equation. Possible time step restrictions arising from the truncation errors in the linearizations (3.8-10) are usually not severe, since the transport and rate coefficients are smooth functions of the mean electron energy. Note that it is essential for this approach that the continuity equation for electrons be solved before solving the energy equation, so that n_e^{k+1} is known.

We combine this technique with the semi-implicit treatment of the electric field, and end up with the following scheme:

First \mathbf{E}^{k+1} is solved from

$$\nabla \cdot (\varepsilon \mathbf{E}^{k+1}) = \sum_p q_p (n_p^k + \Delta t \nabla \cdot \Gamma_p (n_p^k, \mathbf{E}^{k+1}, \mu_p^k, D_p^k)). \quad (3.12)$$

Then for every species p the density n_p^{k+1} is solved from

$$\frac{n_p^{k+1} - n_p^k}{\Delta t} - \nabla \cdot \Gamma_p (n_p^{k+1}, \mathbf{E}^{k+1}, \mu_p^k, D_p^k) = S_p^k. \quad (3.13)$$

Finally, n_ε^{k+1} is calculated from

$$\begin{aligned}\frac{n_\varepsilon^{k+1} - n_\varepsilon^k}{\Delta t} - \nabla \cdot \Gamma_\varepsilon (n_\varepsilon^{k+1}, \mathbf{E}^{k+1}, \mu_e^k, D_e^k) &= S_\varepsilon^k \\ &\quad - \left[\frac{e}{n_e} \mathbf{E} \cdot \left(\frac{\partial \Gamma_e}{\partial \mu_e} \frac{\partial \mu_e}{\partial \bar{\varepsilon}} + \frac{\partial \Gamma_e}{\partial D_e} \frac{\partial D_e}{\partial \bar{\varepsilon}} \right) + \sum_r \bar{\varepsilon}_r \left(\frac{\partial k_r}{\partial \bar{\varepsilon}} \right) n_r \right]^k (n_\varepsilon^{k+1} - n_e^{k+1} \bar{\varepsilon}^k).\end{aligned}\quad (3.14)$$

An appropriate value for Δt is determined by trial and error. We temporarily reduce the time step for iterations where the densities change by more than a certain percentage, say, 10%.

The time integration scheme (3.12-14) has been extensively tested in 2D simulations of microdischarges. We discuss some typical cases. Figure 3.2 shows a typical microdischarge geometry; this configuration was used for the test calculations presented here.

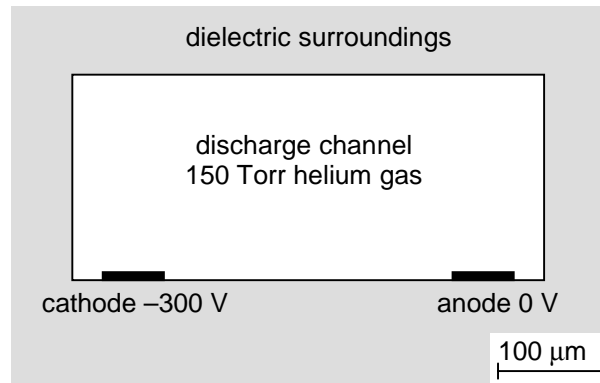


Figure 3.2. Two-dimensional microdischarge geometry used in the test calculations.

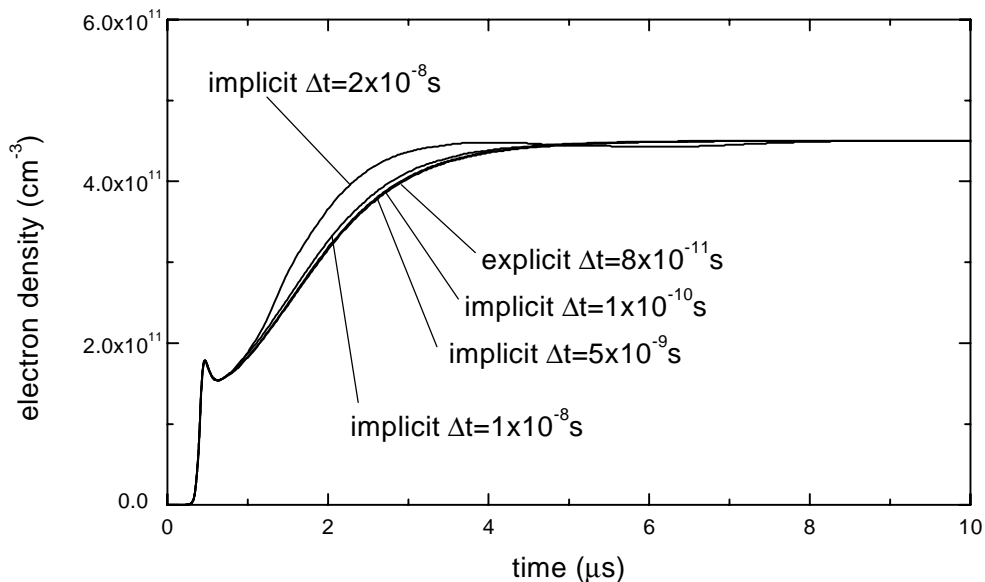


Figure 3.3. Space averaged electron density in the simulation of the development of a DC microdischarge, for different time steps and different treatments of the electron energy source term. Time steps larger than 10^{-10} s were impossible using an explicit energy source term evaluation. The simulated discharge configuration is shown in Fig. 3.2.

First we considered the simulation of the ignition of a DC discharge, which is one of the most transient phenomena in glow discharges. In this case the behavior of the plasma is governed by ionization processes and the development of extremely high space charge fields. Under these conditions an explicit evaluation of the electron energy source term turned out to result in strong fluctuations in the mean electron energy for $\Delta t > 10^{-10}$ s. Applying the implicit treatment to the electron energy source term made it possible to use time steps up to $\Delta t = 10^{-8}$ s, without any significant influence on the calculated results. For larger values of the time step errors in the results could be observed, although even then the calculation remained stable. All calculations yielded exactly the same steady state results, regardless of time step or integration method. Using the implicit method only slightly increased the

computational effort per iteration, so that the speedup gained by the increased time step was tremendous. These calculations are illustrated in Fig. 3.3, which shows the calculated development of the space averaged electron density for different time steps.

Figure 3.4 shows similar curves for the simulation of the afterglow, i.e. the decay of the plasma after the DC voltage over the electrodes has been switched off. The plasma conditions are completely different now: the electric fields and the electron mean energy decrease rapidly and the behavior of the plasma becomes dominated by ambipolar diffusion. Initially the plasma density rises, due to a sudden absence of drift losses while production is still present; then it slowly decreases. Explicit evaluation of the electron energy source term was possible up to $\Delta t = 10^{-9}$ s, but lead to large inaccuracies for $\Delta t > 10^{-10}$ s. Once again implicit evaluation gave good results for $\Delta t = 10^{-8}$ s. The implicit correction of the electron heating part of the energy source term turned out to be essential for these afterglow conditions.

The test results are summarized in Table 3.1. Since the test problems cover a wide range of numerical conditions, similar results can be expected for discharge simulations in general.

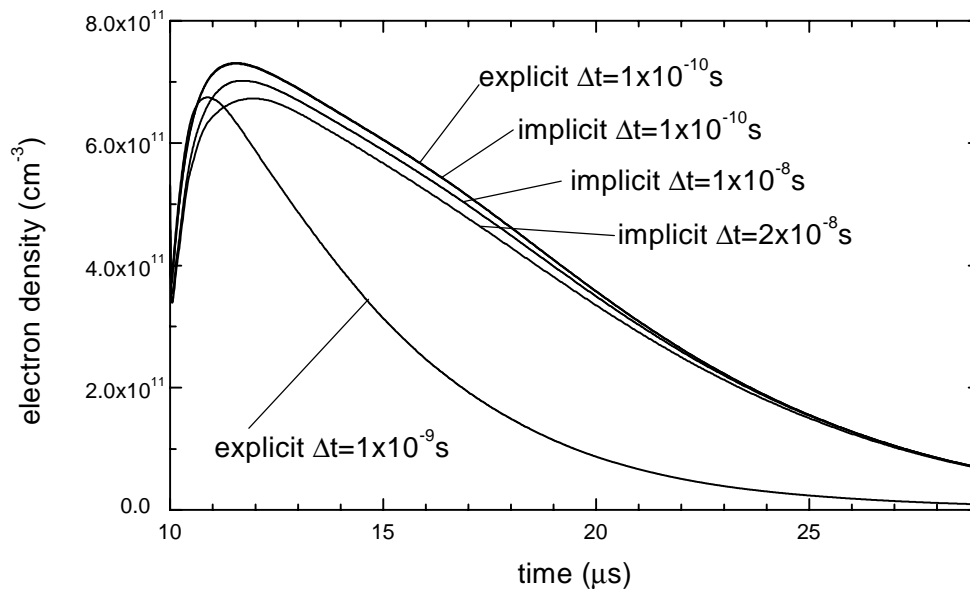


Figure 3.4. Space averaged electron density in the simulation of the afterglow of a microdischarge, for different time steps and different treatments of the electron energy source term. The simulated discharge configuration is shown in Fig. 3.2.

Table 3.1. Comparison between the test results of different time integration schemes.

treatment of electric field	treatment of electron energy source term	typical maximum time step	typical CPU time ratio
explicit	explicit	10^{-11} s, Eq. (17)	1
implicit	explicit	10^{-10} s	1.5×10^{-1}
implicit	implicit	10^{-8} s	2.0×10^{-3}

3.4 Spatial grid and the definition of the discharge configuration

The equations (3.12-14) are solved for two Cartesian spatial dimensions, which we indicate by x and by y , respectively. We use a two-dimensional uniform grid, consisting of lines along the x - and y -directions, equally spaced with intervals Δy and Δx , respectively. In every separate grid cell we define material properties: a cell can be filled with discharge gas, with electrode material at a certain voltage, or with dielectric material with a certain permittivity. In this way, an arbitrarily shaped discharge channel surrounded by an arbitrary configuration of electrodes and dielectric materials can be defined, as is demonstrated in Ref. [Hag99]. The plasma equations (3.13,14) are solved only inside the gas areas. Poisson's equation (3.12) is solved on the entire grid, except inside electrode areas.

Let the x - and y -positions of the grid points be referred by two lower indices, where $x_{I+1,j} = x_{I,j} + \Delta x$ and $y_{I,j+1} = y_{I,j} + \Delta y$. We represent all scalar quantities $X(x,y)$ by their values $X_{I,j}$ at the grid points, and all vector quantities $\mathbf{X}(x,y)$ by the values of their Cartesian components $X_{x,I+1/2,j}$ and $X_{y,I,j+1/2}$ exactly midway between the grid points; see Fig. 3.5 for illustration. The value of a scalar quantity midway between grid points is taken to be the average of its values at the points: $X_{I+1/2,j} = (X_{I+1,j} + X_{I,j})/2$. In the next two sections we describe how the different equations are spatially discretized.

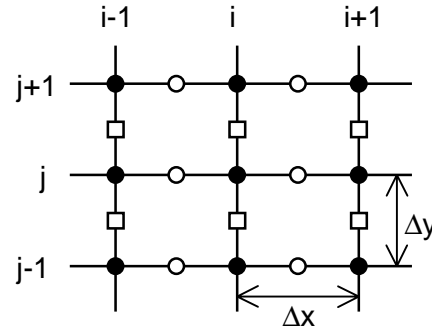


Figure 3.5. Spatial grid used for the numerical solution of the equations. All scalars are evaluated at the grid points marked with solid circles, x -components of vectors at the points marked with open circles, and y -components of vectors at the points marked with open squares.

3.5 Spatial discretization of the transport equations

The transport term in the continuity equations for particles (3.13) and for electron energy (3.14) is discretized as follows:

$$(\nabla \cdot \Gamma)_{i,j} = \frac{\Gamma_{x,i+1/2,j} - \Gamma_{x,i-1/2,j}}{\Delta x} + \frac{\Gamma_{y,i,j+1/2} - \Gamma_{y,i,j-1/2}}{\Delta y}. \quad (3.15)$$

In order to be able to calculate the density in this transport term implicitly, as is required by the time integration scheme, we have to substitute a discretized expression for the drift-diffusion flux. For this purpose we employ the exponential scheme of Scharfetter and Gummel [Scha69], as is done in Refs. [Boe87, Pas93, Boe95, Nie97]. This scheme supports large density gradients, as opposed to the more straightforward central difference scheme [Mor94]. It is based on the analytical solution for a constant drift-diffusion flux between two grid points. For the x -component of the flux it reads

$$\Gamma_{x,i+1/2,j} = -\frac{1}{\Delta x} D_{i+1/2,j} (f_1(z_{x,i+1/2,j}) n_{i+1,j} - f_2(z_{x,i+1/2,j}) n_{i,j}), \quad (3.16)$$

with

$$z_{x,i+1/2,j} = \frac{\text{sgn}(q) \mu_{i+1/2,j} E_{x,i+1/2,j} \Delta x}{D_{i+1/2,j}}, \quad (3.17)$$

and the functions $f_1(z)$ and $f_2(z)$ defined as

$$f_1(z) = \frac{z}{\exp(z) - 1}, \quad (3.18)$$

$$f_2(z) = \frac{z \exp(z)}{\exp(z) - 1} = f_1(z) + z, \quad (3.19)$$

for $z \neq 0$, and $f_1(0) = f_2(0) = 1$. The expression for Γ_y is analogous.

After the substitution of the exponential scheme for the flux, the discretized continuity equation has the form of a five-point equation for the density:

$$a^E_{i,j} n_{i+1,j}^{k+1} + a^W_{i,j} n_{i-1,j}^{k+1} + a^N_{i,j} n_{i,j+1}^{k+1} + a^S_{i,j} n_{i,j-1}^{k+1} + a^C_{i,j} n_{i,j}^{k+1} = A_{i,j}, \quad (3.20)$$

a linear equation that relates the density in a grid point to the densities in the four neighboring grid points. The east, west, north, south, central, and source coefficients of equation (3.20) are given by

$$a^E_{i,j} = -\frac{\Delta t}{\Delta x^2} D_{i+1/2,j} f_1(z_{x,i+1/2,j}), \quad (3.21)$$

$$a^W_{i,j} = -\frac{\Delta t}{\Delta x^2} D_{i-1/2,j} f_2(z_{x,i-1/2,j}), \quad (3.22)$$

$$a^N_{i,j} = -\frac{\Delta t}{\Delta y^2} D_{i,j+1/2} f_1(z_{y,i,j+1/2}), \quad (3.23)$$

$$a^S_{i,j} = -\frac{\Delta t}{\Delta y^2} D_{i,j-1/2} f_2(z_{y,i,j-1/2}), \quad (3.24)$$

$$a^C_{i,j} = 1 - a^E_{i-1,j} - a^W_{i+1,j} - a^N_{i,j-1} - a^S_{i,j+1}, \quad (3.25)$$

$$A_{i,j} = n_{i,j}^k + \Delta t S_{i,j}, \quad (3.26)$$

respectively.

The five-point coefficients (3.21-26) apply to every grid point in the interior of the gas areas of the grid. At the boundaries of the gas areas, the five-point coefficients incorporate the boundary conditions (2.35-39). The boundary condition for the electron flux is discretized as

$$\begin{aligned} (\mathbf{\Gamma} \cdot \mathbf{n})_{i,j} &= (2a_{i,j} - 1) \text{sgn}(q) \mu_{i,j} E_{x,i+1/2,j} n_{i,j} + \frac{1}{2} v_{th,i,j} n_{i,j} \\ &\quad - \frac{1}{2} v_{th,i,j} n_{\gamma,i,j} - 2(1 - a_{i,j}) \sum_p \gamma_p (\mathbf{\Gamma}_p \cdot \mathbf{n})_{i,j}, \end{aligned} \quad (3.27)$$

on a west (left) boundary point. Substitution of this expression in the discretized continuity equation yields the following five-point coefficients for west boundary points:

$$a^E_{i,j} = -\frac{\Delta t}{\Delta x^2} D_{i+1/2,j} f_1(z_{x,i+1/2,j}), \quad (3.28)$$

$$a^w_{i,j} = a^N_{i,j} = a^S_{i,j} = 0, \quad (3.29)$$

$$a^C_{i,j} = \frac{1}{2} - a^w_{i+1,j} + \frac{\Delta t}{\Delta x} (2a_{i,j} - 1) \text{sgn}(q) \mu_{i,j} E_{x,i+1/2,j} + \frac{\Delta t}{2\Delta x} v_{th,i,j}, \quad (3.30)$$

$$A_{i,j} = \frac{1}{2} n^k_{i,j} + \frac{\Delta t}{2} S_{i,j} + \frac{\Delta t}{2\Delta x} v_{th,i,j} n_{\gamma,i,j} + \frac{2\Delta t}{\Delta x} (1 - a_{i,j}) \sum_p \gamma_p (\Gamma_p \cdot \mathbf{n})_{i,j}, \quad (3.31)$$

where the factor 1/2 in the first term of a^C and the first two terms of A results from the fact that transport term (3.15) has been evaluated over the interval $\Delta x/2$, instead of Δx . The expressions for east, north, and south boundaries, and for other particle species, are analogous. For heavy particle species the secondary-emission terms are omitted from the equations (3.27) and (3.31).

A few extra details need to be pointed out about the spatial discretization of the source term for electron energy (3.11). The inner product in the electron heating part of this source term is evaluated as

$$\begin{aligned} (\mathbf{E} \cdot \Gamma_e)_{i,j} &= \frac{1}{2} (E_{x,i+1/2,j} \Gamma_{e,x,i+1/2,j} + E_{x,i-1/2,j} \Gamma_{e,x,i-1/2,j}) \\ &\quad + \frac{1}{2} (E_{y,i,j+1/2} \Gamma_{e,y,i,j+1/2} + E_{y,i,j-1/2} \Gamma_{e,y,i,j-1/2}). \end{aligned} \quad (3.32)$$

An analogous discretization is applied to the inner product in the implicit correction of the electron heating. Here too we use the exponential scheme for the electron flux. This leads to the following discretized expression

$$\begin{aligned} \left[\left(\frac{\partial \Gamma_e}{\partial \mu_e} \right) \left(\frac{\partial \mu_e}{\partial \bar{\varepsilon}} \right) + \left(\frac{\partial \Gamma_e}{\partial D_e} \right) \left(\frac{\partial D_e}{\partial \bar{\varepsilon}} \right) \right]_{x,i+1/2,j} &= -\frac{2}{3e\Delta x} \mu_{e,i+1/2,j} h(z_{x,i+1/2,j}) (n_{e,i+1,j} - n_{e,i,j}) \\ &\quad + \frac{1}{\mu_{e,i+1/2,j}} \left(\frac{\partial \mu_e}{\partial \bar{\varepsilon}} \right)_{i+1/2,j} \Gamma_{e,x,i+1/2,j}, \end{aligned} \quad (3.33)$$

where the function $h(z)$ is defined as

$$h(z) = f_1(z) - \frac{\partial f_1(z)}{\partial z} z = f_2(z) - \frac{\partial f_2(z)}{\partial z} z = \frac{z^2 \exp(z)}{(\exp(z) - 1)^2}. \quad (3.34)$$

In the derivation of equation (3.33) the Einstein relation (2.7,17) has been used.

If we write the discretized energy equation in the five-point form (3.20), the energy source term does not only appear in the source coefficient A , its implicit correction part is also included in the central coefficient a^C . Let ν be defined by the following representation of the energy equation (3.14):

$$\frac{n_\varepsilon^{k+1} - n_\varepsilon^k}{\Delta t} - \nabla \cdot \Gamma_\varepsilon (n_\varepsilon^{k+1}, \mathbf{E}^{k+1}, \mu_\varepsilon^k, D_\varepsilon^k) = S_\varepsilon^k + \nu^k (n_\varepsilon^{k+1} - n_\varepsilon^{k+1} \bar{\varepsilon}^k); \quad (3.35)$$

then the central and source coefficients of the discretized equation will be

$$a^C_{i,j} = 1 - a^E_{i-1,j} - a^w_{i+1,j} - a^N_{i,j-1} - a^S_{i,j+1} - \Delta t \nu_{i,j}^k, \quad (3.36)$$

$$A_{i,j} = n_{\varepsilon,i,j}^k + \Delta t S_{\varepsilon,i,j} - \Delta t \nu_{i,j}^k n_{\varepsilon,i,j}^{k+1} \bar{\varepsilon}_{i,j}^k. \quad (3.37)$$

3.6 Spatial discretization of Poisson's equation

The left hand side of Poisson's equation is discretized by central differencing:

$$\begin{aligned} (\nabla \cdot (\epsilon \mathbf{E}))_{i,j} &= \frac{\epsilon_{i+1/2,j} E_{x,i+1/2,j} - \epsilon_{i-1/2,j} E_{x,i-1/2,j}}{\Delta x} \\ &+ \frac{\epsilon_{i,j+1/2} E_{y,i,j+1/2} - \epsilon_{i,j-1/2} E_{y,i,j-1/2}}{\Delta y}. \end{aligned} \quad (3.38)$$

The right hand side of the semi-implicit version of Poisson's equation (3.12) contains transport terms of charged particle species. To ensure a proper functioning of the semi-implicit technique for the electric field, the discretization of these terms must be consistent with the discretization of the transport equations. We use again the difference expression (3.15). However, discretization of the fluxes according to the exponential scheme (3.16) is inconvenient, because this scheme has the electric field appearing within exponential functions, which makes the required implicit calculation of the field very difficult. This problem is usually straightforwardly circumvented by using a central difference scheme in case, which is linear in the electric field:

$$\Gamma_{x,i+1/2,j} = \left[\text{sgn}(q) \mu_{i+1/2,j} \frac{1}{2} (n_{i+1,j} + n_{i,j}) \right]^k E_{x,i+1/2,j}^{k+1} - \left[D_{i+1/2,j} \frac{n_{i+1,j} - n_{i,j}}{\Delta x} \right]^k. \quad (3.39)$$

We use however another, more consistent approach: we stick to the exponential scheme and linearize this in t^k :

$$\begin{aligned} \Gamma_{x,i+1/2,j} &= \Gamma_{x,i+1/2,j}^k + \left(\frac{\partial \Gamma}{\partial E} \right)_{x,i+1/2,j}^k (E_{x,i+1/2,j}^{k+1} - E_{x,i+1/2,j}^k) \\ &= \left[\text{sgn}(q) \mu_{i+1/2,j} (g_1(z_{x,i+1/2,j}) n_{i+1,j} - g_2(z_{x,i+1/2,j}) n_{i,j}) \right]^k E_{x,i+1/2,j}^{k+1} \\ &\quad - \left[D_{i+1/2,j} h(z_{x,i+1/2,j}) \frac{n_{i+1,j} - n_{i,j}}{\Delta x} \right]^k, \end{aligned} \quad (3.40)$$

where the functions $g_1(z)$, and $g_2(z)$ are defined as

$$g_1(z) = \frac{\partial f_1(z)}{\partial z} = \frac{(1-z)\exp(z)-1}{(\exp(z)-1)^2}, \quad (3.41)$$

$$g_2(z) = \frac{\partial f_2(z)}{\partial z} = \exp(z) \frac{\exp(z)-(1+z)}{(\exp(z)-1)^2}, \quad (3.42)$$

for $z \neq 0$, and $g_1(0) = -1/2$ and $g_2(0) = 1/2$; $h(z)$ is once again given by equation (3.29).

The use of expression (3.40) for the fluxes in the semi-implicit Poisson equation gives better results than the central difference scheme (3.39), especially if large time steps of up to $\Delta t = 10^{-8}$ s are used. As an example, Fig. 3.6 compares both spatial discretization schemes for the afterglow simulation discussed in Section 3.3, where the effect is most apparent. The figure shows that the central difference scheme tends to produce errors, in contrast to the linearized exponential scheme. In all calculations the same uniform Cartesian grid was used. The grid size was appropriate for the exponential scheme, that is, further grid refinement hardly changed the results obtained with this scheme. The central difference scheme obviously requires a finer grid. We did not see the effect in steady state calculations: both discretization methods lead to virtually the same steady state results, even for very large time steps.

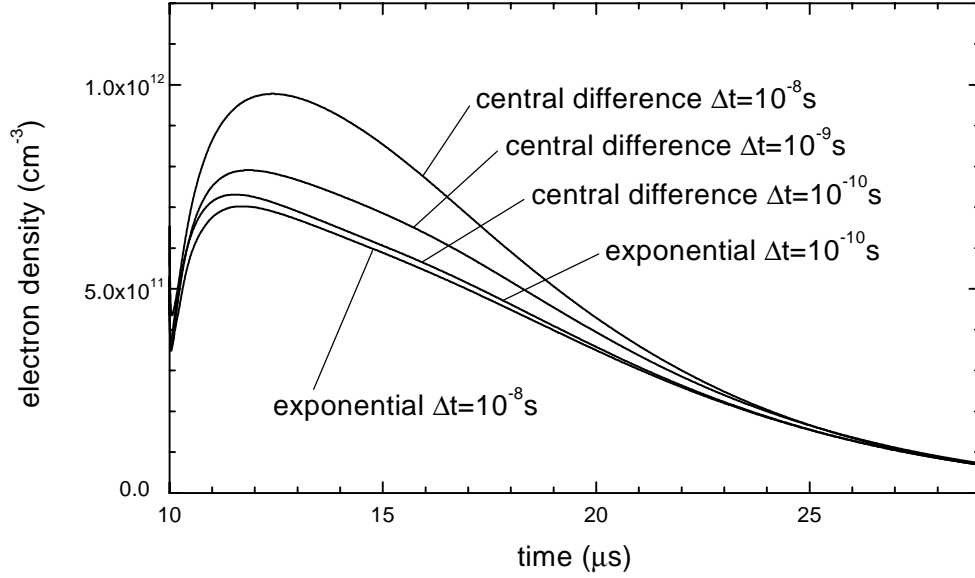


Figure 3.6. Space averaged electron density in the simulation of the afterglow of a microdischarge. The simulated discharge configuration is shown in Fig. 3.2. The figure compares the performances of two spatial discretization schemes for the fluxes in the semi-implicit Poisson equation (3.12), the central difference scheme (3.39) and the linearized exponential scheme (3.40), for different time steps. In all calculations the electron energy source term was handled implicitly.

For the calculation of the electric field, we make use of the electric potential and substitute the difference

$$E_{x,i+1/2,j} = -\frac{V_{i+1,j} - V_{i,j}}{\Delta x} \quad (3.43)$$

and an analogous expression for $E_{y,I,j+1/2}$ into the equations (3.38) and (3.40). On this substitution Poisson's equation becomes a five-point equation for the potential

$$a^E_{i,j}V_{i+1,j} + a^W_{i,j}V_{i-1,j} + a^N_{i,j}V_{i,j+1} + a^S_{i,j}V_{i,j-1} + a^C_{i,j}V_{i,j} = A_{i,j}, \quad (3.44)$$

where

$$a^E_{i,j} = \frac{1}{\Delta x^2} \epsilon_{i+1/2,j} - \frac{\Delta t}{\Delta x^2} \sum_p [q|\mu_{i+1/2,j}(n_{i+1,j}g_1(z_{x,i+1/2,j}) - n_{i,j}g_2(z_{x,i+1/2,j}))], \quad (3.45)$$

$$a^W_{i,j} = \frac{1}{\Delta x^2} \epsilon_{i-1/2,j} - \frac{\Delta t}{\Delta x^2} \sum_p [q|\mu_{i-1/2,j}(n_{i,j}g_1(z_{x,i-1/2,j}) - n_{i-1,j}g_2(z_{x,i-1/2,j}))], \quad (3.46)$$

$$a^N_{i,j} = \frac{1}{\Delta y^2} \epsilon_{i,j+1/2} - \frac{\Delta t}{\Delta y^2} \sum_p [q|\mu_{i,j+1/2}(n_{i,j+1}g_1(z_{y,i,j+1/2}) - n_{i,j}g_2(z_{y,i,j+1/2}))], \quad (3.47)$$

$$a^S_{i,j} = \frac{1}{\Delta y^2} \epsilon_{i,j-1/2} - \frac{\Delta t}{\Delta y^2} \sum_p [q|\mu_{i,j-1/2}(n_{i,j}g_1(z_{y,i,j-1/2}) - n_{i,j-1}g_2(z_{y,i,j-1/2}))], \quad (3.48)$$

$$a^C_{i,j} = -a^E_{i,j} - a^W_{i,j} - a^N_{i,j} - a^S_{i,j}, \quad (3.49)$$

$$\begin{aligned}
A_{i,j} = & -\sum_p \left[qn_{i,j} + \frac{\Delta t}{\Delta x^2} qD_{i+1/2,j} h(z_{x,i+1/2,j}) (n_{i+1,j} - n_{i,j}) \right. \\
& - \frac{\Delta t}{\Delta x^2} qD_{i-1/2,j} h(z_{x,i-1/2,j}) (n_{i,j} - n_{i-1,j}) + \frac{\Delta t}{\Delta y^2} qD_{i,j+1/2} h(z_{y,i,j+1/2}) (n_{i,j+1} - n_{i,j}) \\
& \left. - \frac{\Delta t}{\Delta y^2} qD_{i,j-1/2} h(z_{y,i,j-1/2}) (n_{i,j} - n_{i,j-1}) \right] . \quad (3.50)
\end{aligned}$$

Poisson's equation is solved not only inside the gas areas, but also in the surrounding dielectrics. Within the dielectric areas the space charge and charged particle transport terms are omitted from the five-point coefficients (3.44-50). Surface charge on dielectric walls is taken into account by Gauss's law, which is discretized as

$$\epsilon_{i+1/2,j} E_{x,i+1/2,j} - \epsilon_{i-1/2,j} E_{x,i-1/2,j} = \sigma_{i,j}, \quad (3.51)$$

for west walls. Here the surface charge density is to be evaluated semi-implicitly, similar to the space charge density in Poisson's equation:

$$\sigma_{i,j}^{k+1} = \sigma_{i,j}^k + \Delta t \sum_p q_p \Gamma_{p,x,i+1/2,j}, \quad (3.52)$$

where the fluxes are given by equation (3.40). Dividing by Δx casts equation (3.51) into the form of the discretized Poisson's equation. For the grid points on left walls we find the following five-point coefficients:

$$a^E_{i,j} = \frac{1}{\Delta x^2} \epsilon_{i+1/2,j} - \frac{\Delta t}{\Delta x^2} \sum_p \left[|q| \mu_{i+1/2,j} (n_{i+1,j} g_1(z_{i+1/2,j}) - n_{i,j} g_2(z_{i+1/2,j})) \right]_p^k, \quad (3.53)$$

$$a^W_{i,j} = \frac{1}{\Delta x^2} \epsilon_{i-1/2,j}, \quad (3.54)$$

$$a^N_{i,j} = \frac{1}{\Delta x^2} \epsilon_{i,j+1/2}, \quad (3.55)$$

$$a^S_{i,j} = \frac{1}{\Delta x^2} \epsilon_{i,j-1/2}, \quad (3.56)$$

$$a^C_{i,j} = -a^E_{i,j} - a^W_{i,j} - a^N_{i,j} - a^S_{i,j}, \quad (3.57)$$

$$A_{i,j} = -\frac{\sigma_{i,j}}{\Delta x} - \frac{\Delta t}{\Delta x^2} \sum_p \left[qD_{i+1/2,j} h(z_{i+1/2,j}) (n_{i+1,j} - n_{i,j}) \right]_p^k. \quad (3.58)$$

At the utter edges of the grid, the field inside dielectrics is taken to be parallel to the edges: on the left edge we assume that $V_{Ij} = V_{I+1,j}$, i.e. $a^C_{Ij} = 1$, $a^E_{Ij} = -1$, and $a^W_{Ij} = a^N_{Ij} = a^S_{Ij} = A_{Ij} = 0$. Note that this boundary condition is artificial and unphysical.

3.7 The solution of five-point equations

The discretization described in the previous sections transforms the transport equations and Poisson's equation into sets of linear five-point equations

$$a^E_{i,j} u_{i+1,j} + a^W_{i,j} u_{i-1,j} + a^N_{i,j} u_{i,j+1} + a^S_{i,j} u_{i,j-1} + a^C_{i,j} u_{i,j} = A_{i,j}, \quad (3.59)$$

which need to be solved at every time step. Many numerical techniques exist for the solution of such sets of five-point equations, varying in their efficiency and simplicity. For our purpose iterative techniques – which iteratively improve an estimated solution until a convergence criterion is met – are very efficient, because a good estimate for the solution is always available from the previous time step. A well known iterative

method that is often used in two-dimensional discharge modeling is the classical successive overrelaxation (SOR) technique [Pre92].

Rather than SOR, we use the Modified Strongly Implicit (MSI) method developed by Schneider and Zedan [Sch81]. Besides being extremely simple to implement, this iterative method is very efficient and usually far more powerful than SOR. However, when applied in the way it is presented in the original article [Sch81], the MSI method sometimes fails to find a solution for the transport equations. By trial and error, we have found a rough remedy for this problem. In this section we report our modifications to the MSI method, without pretending to understand why they work.

The original MSI method is implemented as follows:

First the following coefficients are calculated for every grid point:

$$b_{i,j} = \frac{a^S_{i,j}}{1 - \alpha f_{i,j-1} f_{i+1,j-1}} \quad (3.60)$$

$$c_{i,j} = -b_{i,j} f_{i,j-1}, \quad (3.61)$$

$$d_{i,j} = \frac{a^W_{i,j} - b_{i,j} g_{i,j-1}}{1 + 2\alpha g_{i-1,j}}, \quad (3.62)$$

$$\phi^1_{i,j} = c_{i,j} f_{i+1,j-1}, \quad (3.63)$$

$$\phi^4_{i,j} = d_{i,j} g_{i-1,j}, \quad (3.64)$$

$$e_{i,j} = a^C_{i,j} - b_{i,j} h_{i,j-1} - c_{i,j} g_{i+1,j-1} - d_{i,j} f_{i-1,j} + 2\alpha(\phi^1_{i,j} + \phi^4_{i,j}), \quad (3.65)$$

$$f_{i,j} = \frac{a^E_{i,j} - c_{i,j} h_{i+1,j-1} - 2\alpha\phi^1_{i,j}}{e_{i,j}}, \quad (3.66)$$

$$g_{i,j} = -\frac{d_{i,j} h_{i-1,j}}{e_{i,j}}, \quad (3.67)$$

$$h_{i,j} = \frac{a^N_{i,j} - \alpha\phi^4_{i,j}}{e_{i,j}}, \quad (3.68)$$

where α is a parameter which can be chosen between 0 and 1.

Then, an iterative procedure is followed to improve an estimated solution for u . Each iteration requires four steps:

- The residual vector r is calculated as

$$r_{i,j} = A_{i,j} - a^E_{i,j} u_{i+1,j} - a^W_{i,j} u_{i-1,j} - a^N_{i,j} u_{i,j+1} - a^S_{i,j} u_{i,j-1} - a^C_{i,j} u_{i,j}. \quad (3.69)$$

- An intermediate vector v is found by a forward substitution

$$v_{i,j} = \frac{r_{i,j} - b_{i,j} r_{i,j-1} - c_{i,j} r_{i+1,j-1} - d_{i,j} r_{i-1,j}}{e_{i,j}}. \quad (3.70)$$

- A backward substitution of v gives the change vector δ :

$$\delta_{i,j} = v_{i,j} - f_{i,j} v_{i+1,j} - g_{i,j} v_{i-1,j+1} - h_{i,j} v_{i,j+1}. \quad (3.71)$$

- The change δ is added to u :

$$u_{i,j} = u_{i,j} + \delta_{i,j}. \quad (3.72)$$

The steps (3.69-72) are repeated until the norm of the residual $\|r\|$ is small enough to satisfy the convergence criterion

$$\|r\| < 10^{-6} (\|A\| + \|a^c\| \|u\|). \quad (3.73)$$

Note that the coefficients b through h remain unchanged during this process.

The rate of convergence depends upon the choice for α . In most cases $\alpha = 0.9$ gives the fastest convergence. However, when solving a transport equation the procedure sometimes diverges for any $\alpha > 0$. We never saw this problem with Poisson's equation, and remark that Poisson's equation and the test problem considered by Schneider and Zedan have in common that $a^C_{Ij} = -a^E_{Ij} - a^W_{Ij} - a^N_{Ij} - a^S_{Ij}$, which is not the case for the transport equations. Setting α to 0 prevents possible divergence, but slows down the usual rate of convergence by a factor of 5-10 compared to using $\alpha = 0.9$. However, we found out that using

$$b_{i,j} = \begin{cases} 2a^S_{i,j} & 1 - \alpha f_{i,j-1} f_{i+1,j-1} < \frac{1}{2} \\ \frac{a^S_{i,j}}{1 - \alpha f_{i,j-1} f_{i+1,j-1}} & 1 - \alpha f_{i,j-1} f_{i+1,j-1} \geq \frac{1}{2} \end{cases}, \quad (3.74)$$

$$d_{i,j} = \begin{cases} 2a^W_{i,j} & 1 + 2\alpha g_{i-1,j} < \frac{1}{2} \\ \frac{a^W_{i,j} - b_{i,j} g_{i,j-1}}{1 + 2\alpha g_{i-1,j}}, & 1 + 2\alpha g_{i-1,j} \geq \frac{1}{2} \end{cases}, \quad (3.75)$$

rather than equations (3.60) and (3.62), also avoids most cases of divergence. In the equations (3.74-75) the denominators of the coefficients b and d are artificially prevented from approaching zero. We use these modifications in combination with $\alpha = 0.9$. In the very rare case that divergence still occurs, i.e. $\|r\|$ increases rather than decreases, we abort the iterative procedure and resume it after having recalculated the coefficients b through h with $\alpha = 0$.

Chapter 4

The fluid simulation of PALC discharges *

4.1 Introduction

In this chapter we use the fluid model presented in Chapters 2-3, to simulate the microdischarges in PALC displays. Our aim is more to demonstrate the possibilities of the fluid model than to find actual improvements of the PALC technology. For a description of the PALC operation principle we refer to Chapter 1.

All calculations presented here are based on the standard geometry shown in Fig. 4.1, which represents a cross section through three consecutive discharge channels of a PALC display. Three channels are taken into account in order to be able to study cross-talk effects: electrical influences of adjacent channels on each other. In addition, a large region of the bottom glass plate is included in order to obtain the correct electric field at the bottom wall of the discharge channels. As a discharge gas we consider pure helium and helium–hydrogen mixtures; the species and reactions taken into account can be found in Table 2.1. The simulation of one single PALC discharge and afterglow takes 2 – 10 minutes of CPU time on a Pentium II PC.

We first present the simulation of a discharge pulse (Section 4.2) and an afterglow (Section 4.3) in a PALC channel. Then we present the calculation of the surface charge and the resulting transmission, that develops during a series of discharge pulses and afterglows in three consecutive channels, corresponding to a realistic addressing procedure (Section 4.4). Where applicable, we compare the simulation results with experimental data, taken from Ref. [Slo99].

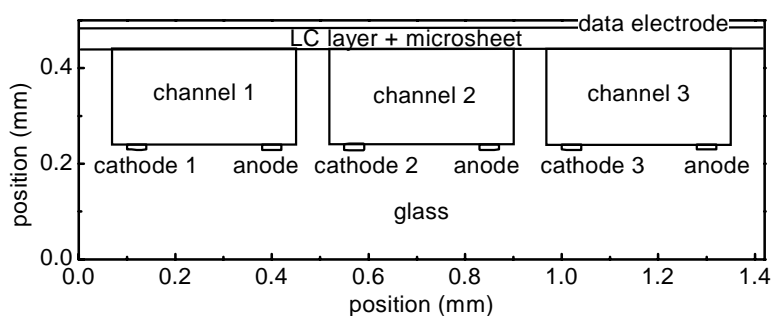


Figure 4.1. Standard geometry used for the calculations. The dielectric constant of the glass plate with inter-channel walls is 6.0, the LC layer with microsheet has an effective dielectric constant of 5.0.

This chapter, in slightly altered form, has been published in: G. J. M. Hagelaar, G. M. W. Kroesen, U. van Slooten, and H. Schreuders, "Modeling of the microdischarges in plasma addressed liquid crystal displays," *J. Appl. Phys.* **88** (5), 2252-2262 (2000).

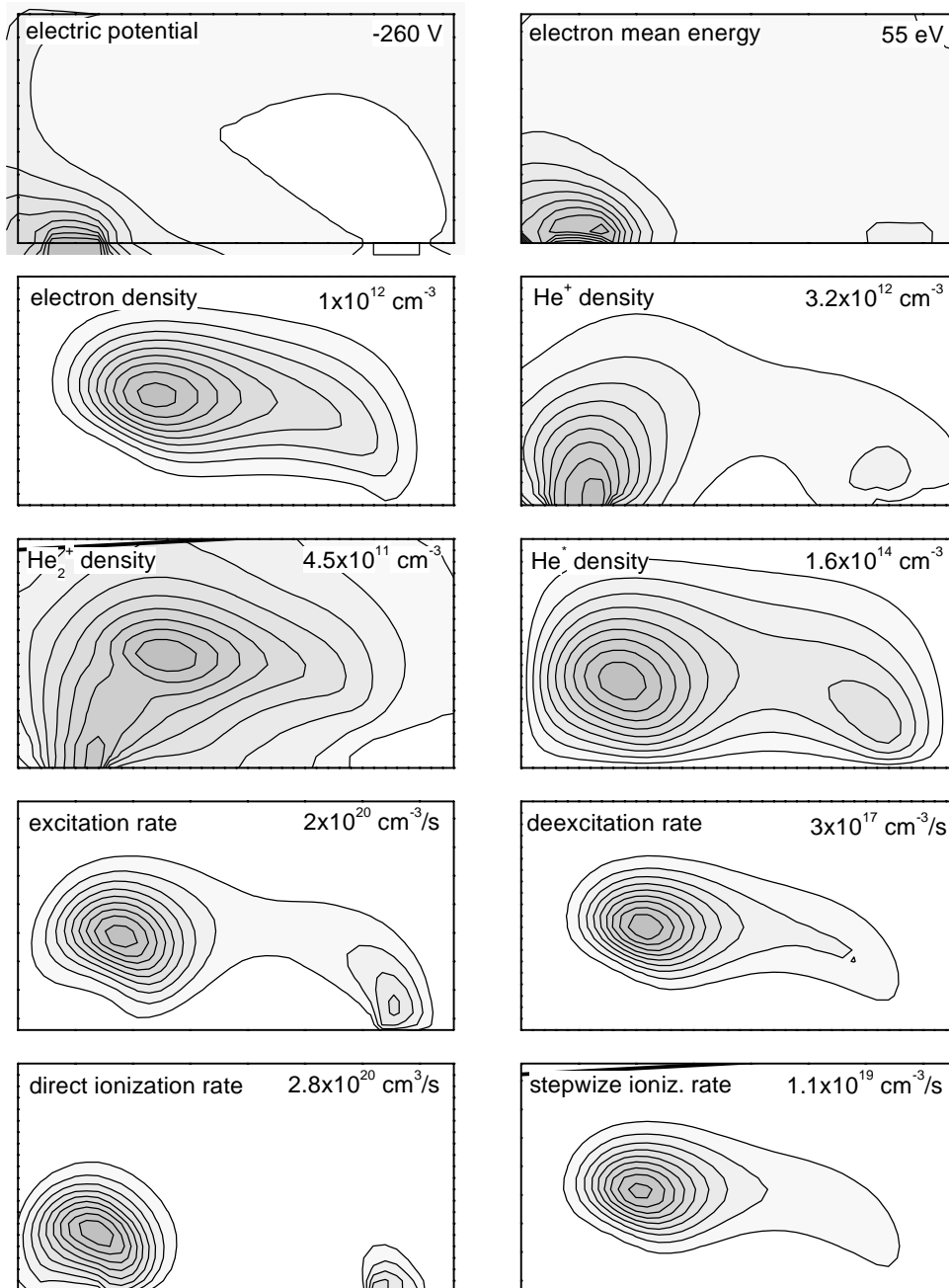


Figure 4.2. Electric potential, electron mean energy, particle densities, and electron impact reaction rates in a DC discharge in pure helium. These plots correspond to the middle channel of the geometry shown in Fig. 4.1. The gas pressure is 150 Torr. Cathode 2 is set to -260 V, all other electrodes are grounded. The resulting current is 3.0 mA/cm. The increment of the contours is $1/10$ times the maximum value indicated in the top right corner of each plot; the darkest regions correspond to this maximum value.

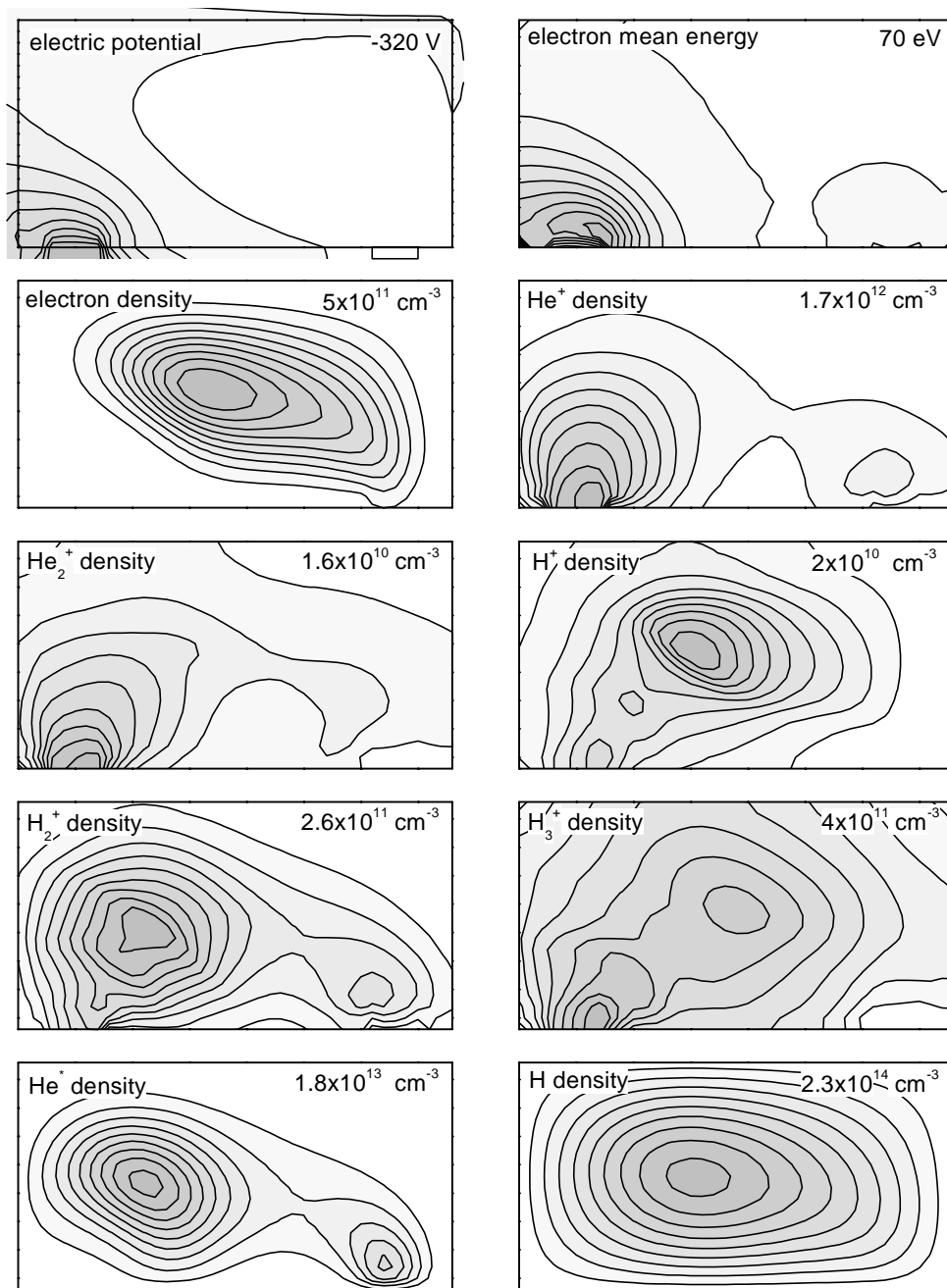


Figure 4.3. Electric potential, electron mean energy, and particle densities in a DC discharge in a mixture of 97% helium and 3% hydrogen. These plots correspond to the middle channel of the geometry shown in Fig. 4.1. The gas pressure is 105 Torr. Cathode 2 is set to -320 V , all other electrodes are grounded. The resulting current is 3.0 mA/cm . The increment of the contours is $1/10$ times the maximum value indicated in the top right corner of each plot; the darkest regions correspond to this maximum value.

4.2 Discharge pulse

A PALC discharge is generated by a DC voltage pulse on the channel electrodes. Figs. 4.2 and 4.3 show the calculated steady state particle densities and electron mean energy under typical conditions at the end of the pulse, for helium and a mixture of 97% helium and 3% hydrogen. These results clearly show a so-called cathode fall: a region in front of the cathode where the total positive ion density exceeds the electron density by orders of magnitude. The strong positive space charge density of the cathode fall screens the remainder of the channel largely from the applied electric field. This remaining region contains a quasi-neutral plasma. In the cathode fall region an extremely high electric field heats the electrons to a mean energy of about 50 eV, resulting in high electron impact ionization and excitation rates. As a result particle species which are mainly created by electron impact reactions reach their maximum density around the cathode fall region, whereas species created in heavy particle reactions, such as He_2^+ , are mainly present in the plasma region. As can be seen comparing Fig. 4.2 with Fig. 4.3, the cathode fall in the helium–hydrogen mixture is very similar to the one in helium, but in the plasma region the role of the helium ions is taken over by the hydrogen ions.

By performing steady state DC discharge calculations for different discharge voltages, it is possible to calculate current-voltage (I-V) curves, which can be compared with experimental data. Exact quantitative agreement cannot be expected, in view of the fact that the I-V curves are extremely sensitive to many delicate parameters, such as secondary emission coefficients. However, trends in calculated I-V curves turn out to be in very good agreement with trends in measured I-V curves. As an example, Figs. 4.4 and 4.5 present a study of the influence of the channel height and the electrode width on the I-V curve of a pure helium discharge. Figure 4.4 shows that channel height does not affect the I-V curve as long as it is well above 200 μm . For smaller channel heights the cathode fall region is somewhat squeezed by the channel walls, which leads to an increase in the discharge voltage.

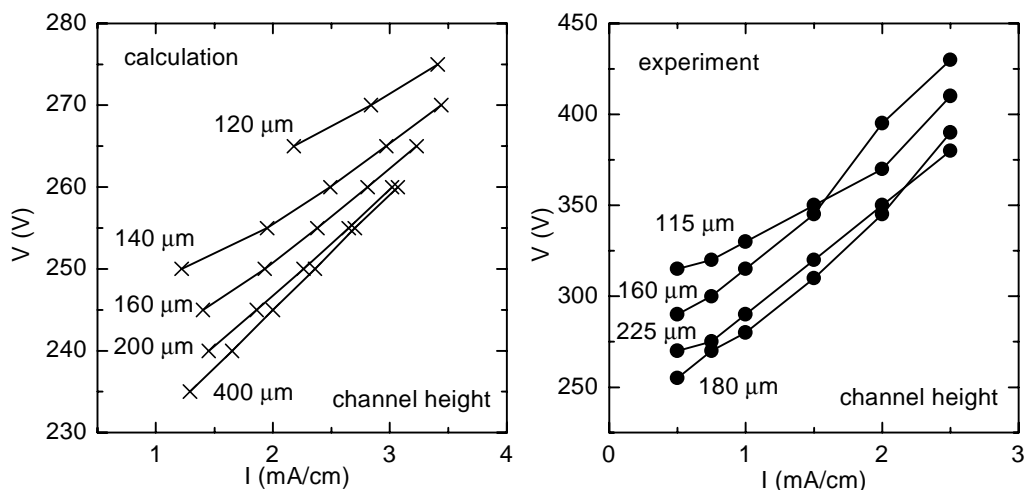


Figure 4.4. Calculated and measured I-V curves of pure helium at 150 Torr, for different the channel heights. The simulated discharge configurations are all similar to the one shown in Fig. 4.1; the discharges are created only in the middle channel.

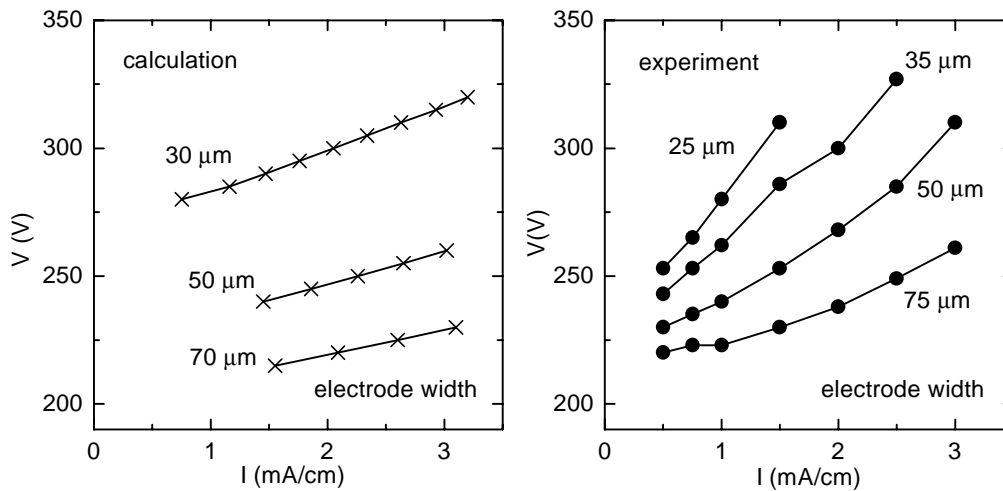


Figure 4.5. Calculated and measured I-V curves of pure helium at 150 Torr, for different electrode widths. The simulated discharge configurations are all similar to the one shown in Fig. 4.1; the discharges are created only in the middle channel.

4.3 Afterglow

During the period immediately following the discharge pulse – the so-called afterglow – the plasma in the channel decays. In the simulations we assume the electrode voltage to go down abruptly to 0 V at the beginning of the afterglow; this assumption seems to be a reasonable approximation of the reality. Figs. 4.6 and 4.7 show the simulated decay of the different particle species in the afterglow in pure helium and in a mixture of 97% helium and 3% hydrogen, respectively. Initially the densities of most charged species increase somewhat, due to the sudden decrease in drift losses, while production still continues. During the first part of the afterglow the electrons and ions are coupled together by space charge fields, resulting in ambipolar diffusion. As the plasma density decreases, the space charge fields become weaker, until the ambipolar diffusion breaks and the electrons run off, leaving the ions behind.

In pure helium however, the decay is not determined by diffusion alone. In this gas the decay of charged species is enormously slowed down by metastable-metastable ionizations R9 and R10 (Table 2.1), which continue far into the afterglow. As can be seen in Fig. 4.6, the electrons produced by these processes leave the channel very quickly, indifferent to the ambipolar coupling, due to their relatively high energies. (See Section 2.4.) The produced ions then lead to enhanced trapping of the less energetic thermalized electrons remaining from the discharge. In helium–hydrogen mixtures the helium metastables are strongly quenched by Penning reactions R7 and R8 so that the metastable-metastable ionizations have no influence.

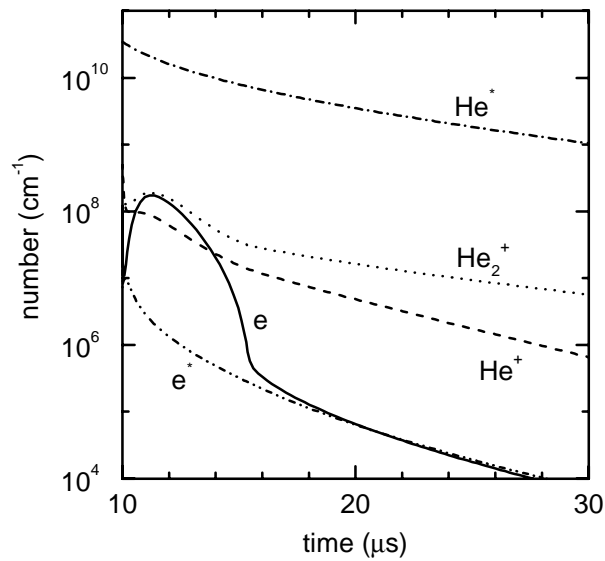


Figure 4.6. Decay of the numbers of particles in the afterglow in pure helium, per cm of channel length. The particle numbers can be converted into space averaged densities by division by $7.6 \times 10^{-4} \text{ cm}^2$. Two electron groups are shown separately in this figure: e are the (thermalized) electrons produced by electron impact ionization, e^* are the (non-thermalized) electrons originating from metastable-metastable ionization. (See Section 2.4.) The discharge configuration is shown in Fig. 4.1; all electrodes are grounded. The gas pressure is 150 Torr. This afterglow belongs to the discharge shown in Fig. 4.2.

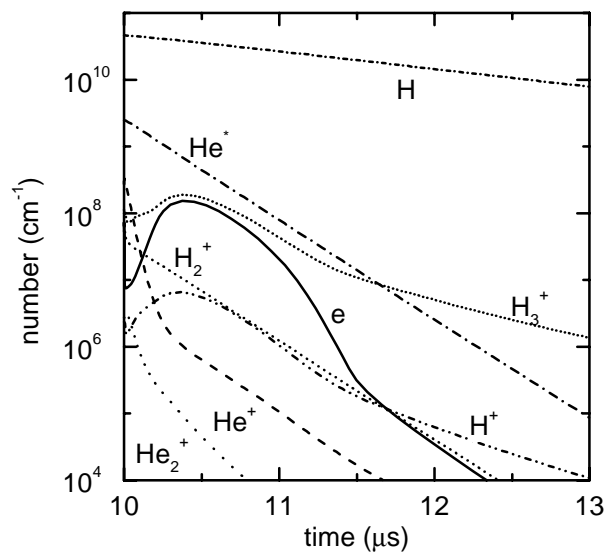


Figure 4.7. Decay of the numbers of particles in the afterglow in a mixture of 97% helium and 3% hydrogen, per cm of channel length. The particle numbers can be converted into space averaged densities by division by $7.6 \times 10^{-4} \text{ cm}^2$. The discharge configuration is shown in Fig. 4.1, all electrodes are grounded. The gas pressure is 105 Torr. This afterglow belongs to the discharge shown in Fig. 4.3.

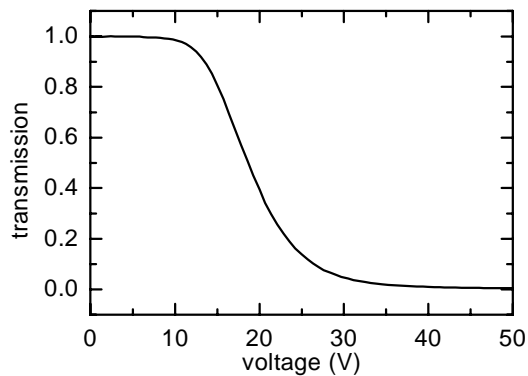


Figure 4.8. Typical transmission-voltage curve. Note that all light is transmitted if the microsheet is uncharged.

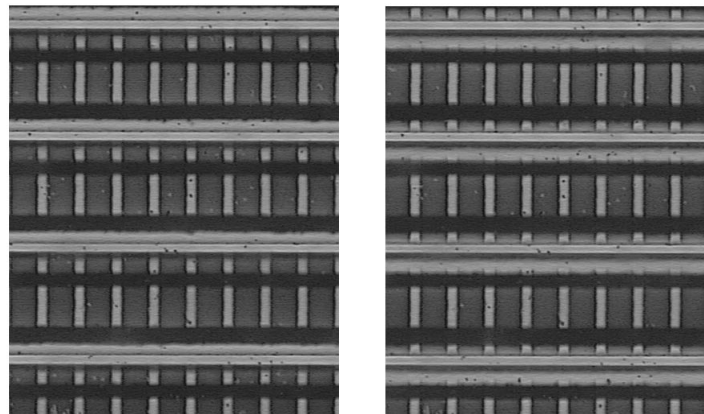


Figure 4.9. Two charge coupled device camera images of the same part of a PALC display. The channels are directed horizontally; three and a half channels are shown. The two images correspond to two different addressing procedures: in the left picture the channels were addressed from the top to the bottom, in the right one from the bottom to the top. The horizontal black stripes are the opaque channel electrodes. All the light stripes result from insufficient charging of the microsheet: the sharp horizontal light stripes correspond to the inter-channel ribs, the vertical light stripes to the gaps between the data electrodes. Additional horizontal vague light stripes can be seen inside the channels, close to the ribs, indicating charging inhomogeneities. In the left picture these effects mainly take place at the bottom sides of the channels, in the right picture at the top sides. These images are taken from Ref. [Slo99].

4.4 Addressing

In true PALC operation, small voltages are applied to the data electrodes during the discharge pulse and the afterglow, which leads to the buildup of surface charge on the microsheet. The surface charge invokes an electric field in the LC layer, resulting in a certain transmission of the polarizing layers. The percentage of light transmitted by the polarizers as a function of the of the total voltage across the LC layer and the microsheet is given by a so-called transmission-voltage curve. Using the transmission-voltage curve shown in Fig. 4.8, it is possible to calculate transmission profiles of simulated PALC channels, which can be compared with experimental results. Transmission measurements on real PALC panels, such as shown in Fig. 4.9, have raised the suspicion that the buildup of surface charge in a certain channel is

influenced by the surface charge present in the adjacent channels (electrical cross-talk). A proper calculation of the surface charge and the resulting transmission profile therefore requires the full simulation of not only the channel in question, but also of the two neighboring channels.

We use the three channel geometry of Fig. 4.1. Following a realistic addressing procedure, the channels are addressed one by one, from the left to the right, every time inverting the sign of the voltage on the data electrodes (row inversion). The exact model addressing scheme is represented by Fig. 4.10. We apply a data voltage of ± 20 V, corresponding to the maximum slope of the transmission-voltage curve, where the transmission is most sensitive to charging errors. The calculated electric potential at the end of the three channel addressing scheme is plotted in Fig. 4.11. It can clearly be seen, that the surface charge field in the LC-layer and microsheet is directed oppositely for the consecutive channels, due to the row inversion technique. Note that the outer sides of first and the last channel are not properly modeled, given the artificial boundary conditions for the electric field at the edges of the simulation domain; only the middle channel has been treated correctly.

Figure 4.12 shows the final transmission profile of this middle channel. In the center of the channel a homogeneous transmission has been achieved, but near the inter-channel walls (ribs), transmission inhomogeneities occur. The charging is incorrect especially on the right hand side of the channel. This asymmetric effect is in full agreement with the experimental observations shown in Fig. 4.9. It results from electrical cross-talk: At the moment the surface charge in the middle channel is established, the right neighbor channel contains a repelling surface charge with the same polarity, whereas the left neighbor channel has an attracting surface charge with opposite polarity. In fact, the phenomenon depends on the addressing procedure; if the channels are addressed in reverse order (so: from right to left), the main charging errors occur on the other side of the channel.

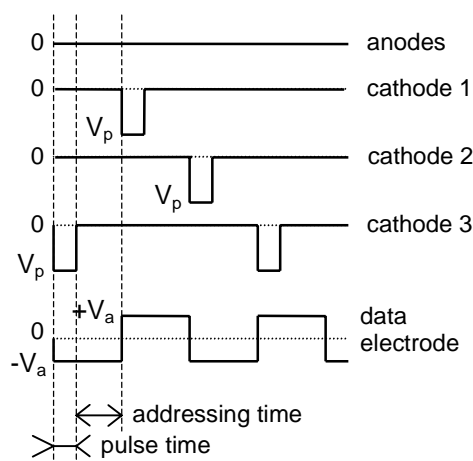


Figure 4.10. Electrode potentials as a function of time in a realistic addressing procedure. This figure relates to the three channel geometry shown in Fig. 4.1. The last three discharge pulses (in the channels 1, 2, and 3, respectively) represent one picture frame, where the rows are addressed from left to right. The first pulse (in channel 3) belongs to the previous frame.

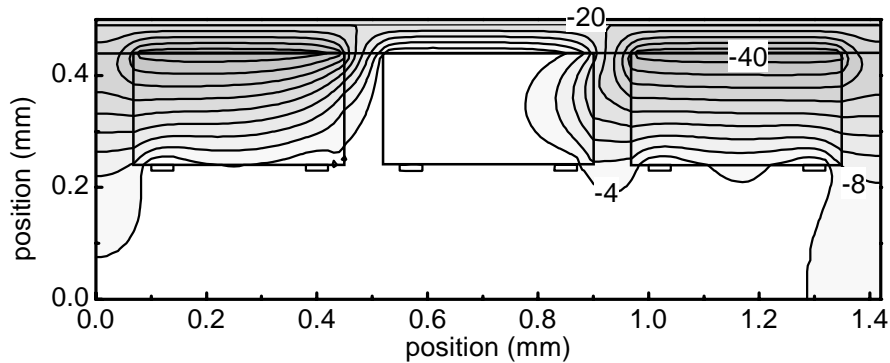


Figure 4.11. Calculated electric potential in the three channel geometry of Fig. 4.1, at the end of the addressing procedure represented by Fig. 4.10. The unit of the indicated potentials is Volt. The increment of the contours is 4 V.

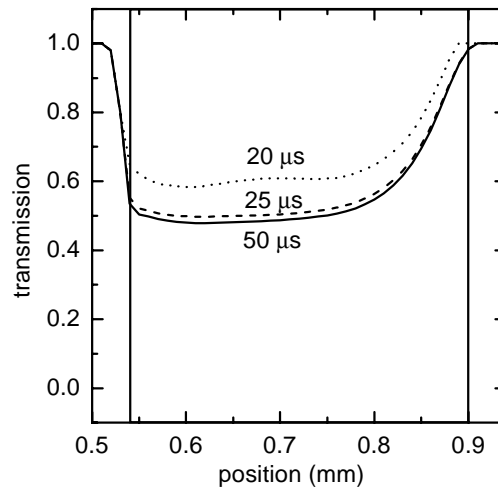


Figure 4.12. Calculated transmission profiles of a PALC channel filled with pure helium, for different addressing times. This graph corresponds to the middle channel of the geometry shown in Fig. 4.1. The vertical lines indicate positions of the channel walls. The gas pressure is 150 Torr. The pulse voltage is 260 V, the addressing voltage -20 V.

Figure 4.12 also illustrates that a minimum of addressing time is required for a proper charging: If the addressing time is too short for the plasma to decay, the row inversion will partially erase the surface charge, leading to an increase of the transmission. According to Fig. 4.12, at least $30 \mu\text{s}$ of addressing time are needed for pure helium channels. The minimal required addressing time is determined by the decay rate of the plasma; one can define a plasma decay time as the addressing time corresponding to a 1% increase in transmission in the center of the channel. Figure 4.13(a) shows a comparison of calculated and measured decay times for helium at different pressures. The helium decay time goes up as the pressure increases, due to an increase of the metastable density and a decrease of the diffusion coefficients. In Fig. 4.13(b) the calculated and measured decay times for different helium-hydrogen mixtures are compared. Adding hydrogen to helium strongly decreases the decay time,

due to the quenching of the helium metastables. For all calculations the agreement with experiment is excellent.

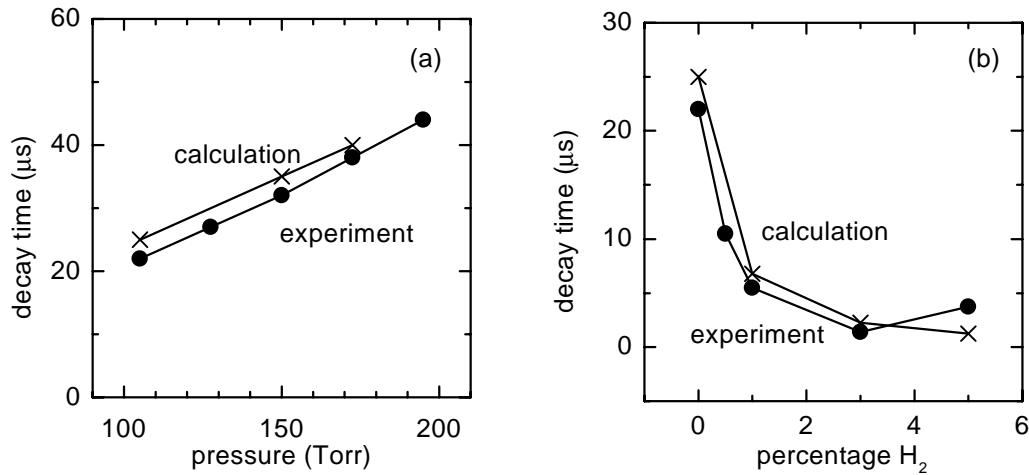


Figure 4.13. Decay time as a function of (a) gas pressure, where the discharge gas is pure helium, and (b) percentage of hydrogen, where the gas pressure is 105 Torr. Here the decay time is defined as the addressing time corresponding to a transmission error of 1%. (See text.) For all calculations the discharging current is 3.0 mA/cm and the data voltage -20 V. The experimental data are taken from Ref. [Slo99].

4.5 Conclusions

The fluid model presented in Chapters 2-3 is capable of simulating the full PALC operation. We have reproduced a series of discharge pulses and afterglows in three consecutive PALC channels, filled with pure helium or helium-hydrogen mixtures. The simulations show that at the end of a discharge pulse a cathode fall and a plasma region are present in the channel in question. Calculated I-V curves of the PALC discharges are in good agreement with measurements. The simulations reproduce non-uniformities in the charging of the microsheat, known from experiments, and related to electrical cross-talk between adjacent channels. Calculated plasma decay times are in excellent agreement with measured decay times. In pure helium, the decay is slowed down enormously by a continuous plasma production through metastable-metastable ionization; in helium-hydrogen mixtures the helium metastables are quenched so that this effect does not take place.

Chapter 5

Energy loss mechanisms in PDP discharges^{*}

5.1 Introduction

One of the major drawbacks of PDPs is their low luminous efficacy: about 1 lm/W, compared to 4 lm/W for the conventional CRT displays. Energy loss in color PDPs occurs in various ways: Only about 40% of the UV photons emitted by the discharges is captured by the phosphors, where an additional 80% of photon energy is lost in the conversion to visible light, mainly due to the difference in wavelength of the visible light and the UV radiation. Next, only about half of the visible light emitted by the phosphors leaves the display on the front side, the other half is absorbed somewhere in the display. However, the largest energy loss occurs in the microdischarges themselves: less than 10% of the electrical input energy is used for the emission of UV photons. In this chapter we analyze the energy loss mechanisms in the PDP discharges, using the fluid model presented in Chapters 2-3. Once again, our aim is more to demonstrate the possibilities of the model than to find technological improvements. For a description of the PDP technology we refer to Chapter 1.

We simulate the discharges occurring in a coplanar-electrode type PDP. [Hir98] The considered model geometry, shown in Fig. 5.1, represents a discharge cell, or actually an entire row, of the display. Due to its two-dimensionality, the model geometry is only an approximation of the real PDP geometry, which has important three-dimensional features. The barrier ribs that separate the columns of the display are not represented in the model; instead, the model cell has side walls along the sustain electrodes. Simulating a real driving scheme, we apply a square wave voltage to the two sustain electrodes (common and scan), with an amplitude below the breakdown voltage. Each simulation is started with a write pulse, which initiates the discharges and switches the cell on. The exact model driving scheme is shown in Fig. 5.2. An external circuit, involving back-coupling from the current to the electrode voltage, is not included in the model. We do however take into account a small rise time (~ 100 ns) for all voltage changes; this seems to be a reasonable approximation of the reality. The discharge gas is a mixture of a small percentage of xenon in neon, at a pressure of 450 Torr. We take into account the extensive reaction scheme presented in Table 2.2, which describes both the electrical behavior of the discharge and the mechanisms of UV generation. The simulation of a single discharge takes 10-20 minutes on a modern PC.

Section 5.2 presents the simulation results illustrating to operation of a typical PDP discharge. In Section 5.3 we analyze how the electrical energy is dissipated in the discharge. In Section 5.4 we study how the energy dissipation and the resulting discharge efficiency are influenced by several discharge parameters.

^{*} This chapter, in slightly altered form, has been submitted for publication.

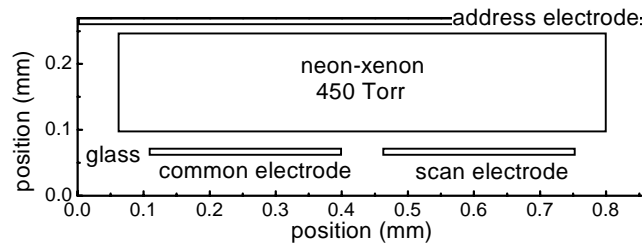


Figure 5.1. Model geometry used in the calculations. This geometry represents a discharge cell of a coplanar-electrode PDP. The top of the geometry corresponds to the back plate of the display, the bottom to the front plate. The sustain electrodes are indicated as the common and scan electrodes. The dielectric constant of the glass is 11.0.

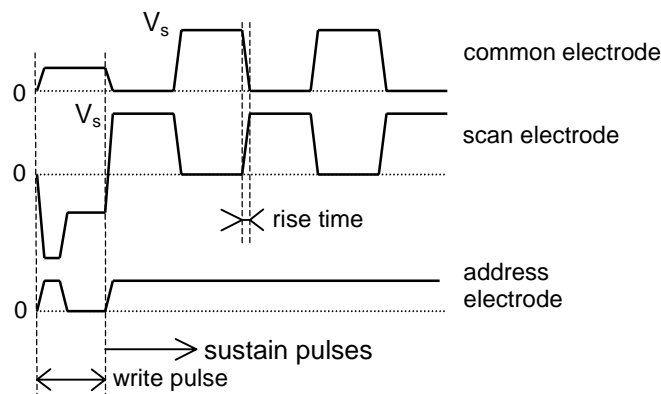


Figure 5.2. Electrode potentials as a function of time in the model driving scheme. This figure relates to the model geometry shown in Fig. 5.1, where the common and scan electrodes are the sustain electrodes. Typically the amplitude of the sustain voltage is $V_s = 180\text{--}300\text{ V}$, its frequency 50-250 kHz.

5.2 Simulation of a PDP discharge

Once a PDP cell has been switched on, a transient discharge occurs each time the sustain voltage changes polarity. Each discharge is quenched by the accumulation of surface charge on the dielectric layer that covers the electrodes. Figs. 5.3 and 5.4 show the electric potential and the xenon excitation rate in the model geometry, during simulation of a typical PDP discharge. By the end of the discharge that precedes the one considered in these figures, stored surface charge screens the discharge gas almost entirely from the applied voltage. After the sustain voltage has been switched, the same surface charge reinforces the applied voltage, rather than canceling it. The total voltage across the discharge gas is now so high that the ignition of a new discharge takes place, despite the fact that the sustain voltage itself is below the breakdown voltage.

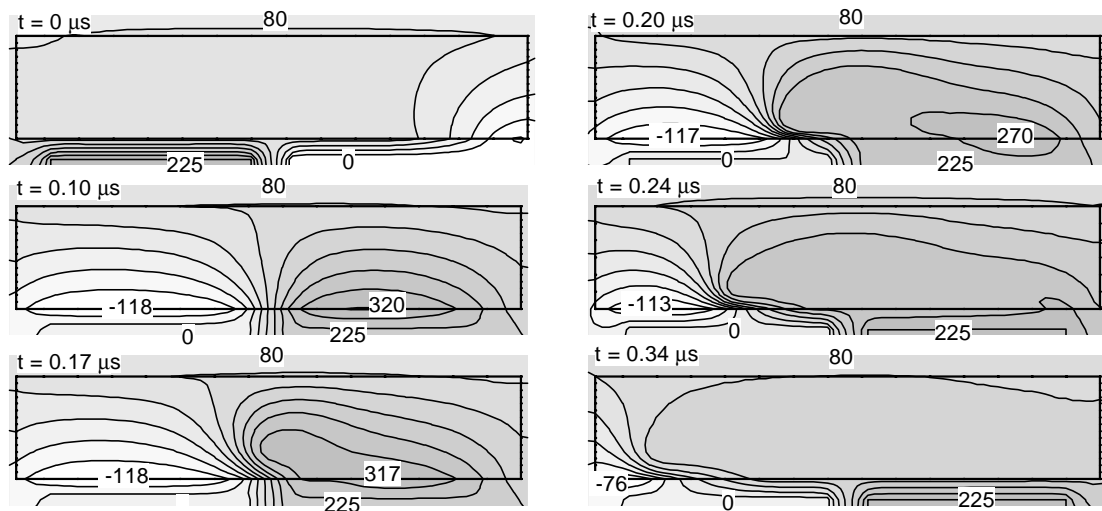


Figure 5.3. Time evolution of the electric potential profile during a PDP discharge. The geometry is shown in Fig. 5.1. The sustain voltage is 225 V, the sustain frequency is 50 kHz, the pressure is 450 Torr, and the xenon percentage is 5%. The moment $t = 0$ corresponds to the end of the previous sustain pulse; the sustain voltage is switched between $t = 0 \mu\text{s}$ and $t = 0.10 \mu\text{s}$, with a rise time of $0.10 \mu\text{s}$. The increment of the contours is 1/10 times the difference of the maximum and minimum values, which are indicated in each plot. The unit of the indicated potentials is V.

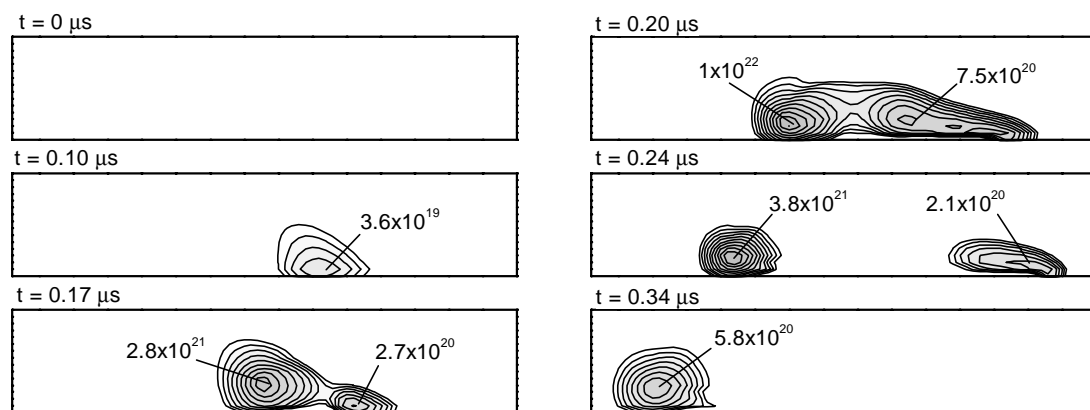


Figure 5.4. Time evolution of the excitation rate of the resonant $\text{Xe}^*(^3P_1)$ state during a PDP discharge. This figure shows results of the same simulation as Fig. 5.3; the discharge conditions are indicated in the caption of that figure. For all plots the contours correspond to a logarithmic scale covering the range from 10^{18} to $10^{22} \text{ cm}^{-3} \text{ s}^{-1}$; the increment of the contours is a factor of 2.51. The unit of the values indicated in the plots is $\text{cm}^{-3} \text{ s}^{-1}$.

It appears from Figs. 5.3 and 5.4 that the discharge starts in the center of the geometry, where the electrodes are close together. As soon as a new surface charge distribution is established in the center of the geometry, the discharge spreads outward. Eventually the entire electrodes are screened by the new surface charge distribution, and the discharge stops. Note that the current through the electrodes is a displacement current, resulting from the changes in the electric fields in the dielectric layer that covers them. During the discharge, extremely strong electric fields are present in the plasma sheath front of the cathode, which has the character of a cathode fall. Ionization and excitation mainly take place in the vicinity of this cathode sheath.

Figure 5.5 shows the calculated time evolution of the (space integrated) densities of the most important species during the discharge. The densities rapidly increase at the beginning of the sustain pulse, and then gradually decay. Neon ions are only present during the very first part of the discharge; during the plasma decay Xe_2^+ becomes the most important ion species.

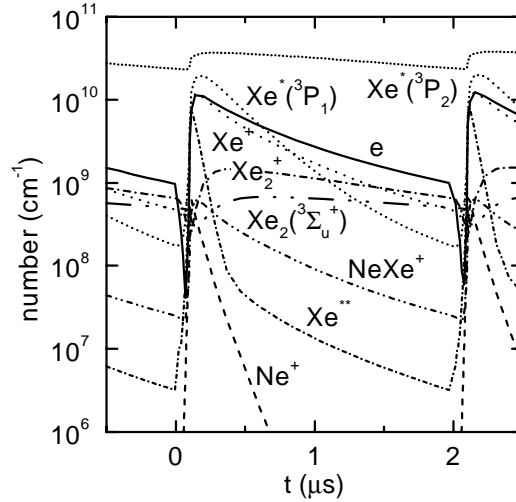


Figure 5.5. Time evolution of the numbers of particles of the most important species. The particle numbers per cm of row length on the vertical axis can be converted into averaged densities by division by $1.11 \times 10^{-3} \text{ cm}^2$. This figure shows results of the same simulation as Fig. 5.3; the discharge conditions are indicated in the caption of that figure.

5.3 Analysis of the energy dissipation

During the discharge, electrical energy is transferred to the plasma through the acceleration of the charged particles. The energy that is thus consumed by the particle species p is

$$W_p = \int_{\text{time discharge}} \iiint_{\text{volume}} q_p \Gamma_p \cdot \mathbf{E} d^3V dt, \quad (5.1)$$

where q is the particle charge, Γ is the particle flux, and \mathbf{E} is the electric field. Note that the sum of these energies must be equal to the total electrical energy input:

$$\sum_p W_p = \int_{\text{time}} I \times V dt, \quad (5.2)$$

where I is the (displacement) current through a sustain electrode and V is the sustain voltage. We confirmed that this relation is reproduced by the fluid model within 0.01%, which illustrates its numerical consistency. The main energy consumption takes place in the plasma sheaths, mostly on the cathode side of the discharge, where the sheath contains an extremely strong electric field, as can be seen in Fig. 5.3.

Figure 5.6 shows the calculated energy consumption of the various charged particle species in a typical PDP discharge. The larger part of the energy turns out to be consumed by ions. This energy is lost for the production of UV photons: under the PDP discharge conditions, ionization or excitation by ion impact seem negligible,

which implies that all the ion energy is eventually transferred to the gas and the surface. Note that ion impact ionization or excitation are not included in the model; even if they would occur, we would not see them in the simulations. The electron energy, on the other hand, is largely used for the excitation and ionization. The energy that is used for a reaction r is

$$W_r = \int_{\text{time discharge}} \iiint_{\text{volume}} \bar{\epsilon}_r R_r d^3V dt \quad (5.3)$$

Figure 5.7 shows the how the electron energy is used in the different reactions.

Of all the processes in Fig. 5.7, it is mainly the excitation of xenon atoms that eventually leads to the generation of UV photons. There are several possible mechanisms: First, the resonant state $\text{Xe}^*(^3P_1)$ decays directly to the ground state, emitting UV photons at a wavelength of 147 nm. Second, both the resonant $\text{Xe}^*(^3P_1)$ and metastable $\text{Xe}^*(^3P_2)$ state may attach to xenon gas atoms and form excited dimers Xe_2^* ; these dimers decay radiatively into ground state atoms. The photons thus emitted by the higher vibrational levels $\text{Xe}_2^*(O_u^+)$ are distributed around 150 nm, those emitted by the lower vibrational levels $\text{Xe}_2^*(^3\Sigma_u^+, ^1\Sigma_u^+)$ around 173 nm. The higher atomic states Xe^{**} and Xe^{***} do not directly lead to UV photons, but cascade down to the $\text{Xe}^*(^3P_1, ^3P_2)$ levels. In this case some energy is lost in the form of infrared radiation or gas heating.

The energy that is emitted from the discharge in the form of UV photons with a wavelength λ is

$$W_\lambda = \int_{\text{time discharge}} \iiint_{\text{volume}} (hc/\lambda) R_\lambda d^3V dt \quad (5.4)$$

where h is Planck's constant, c is the velocity of light, and R_λ is the rate of the decay process leading to the emission. The relative importance of the different UV wavelengths (147, 150, and 173 nm) depends on heavily on the partial xenon pressure. Figure 5.8 shows the fraction of the UV energy emitted at 147 nm, $W_{147 \text{ nm}}/(W_{147 \text{ nm}}+W_{150 \text{ nm}}+W_{172 \text{ nm}})$, as a function of the xenon content. The simulation results are in excellent agreement with the experimental values of Ref. [Sni99], determined by integrating the measured emission spectrum.

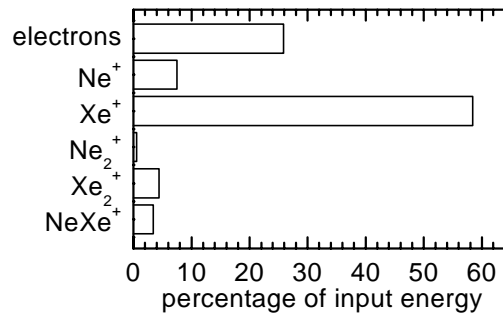


Figure 5.6. Breakdown of the electrical input energy into the heating of the different charged particle species. The total energy consumption is 3.4×10^{-7} J per discharge (pulse) per cm of row length. The sustain voltage is 225 V, the sustain frequency is 250 kHz, the xenon percentage is 5%.

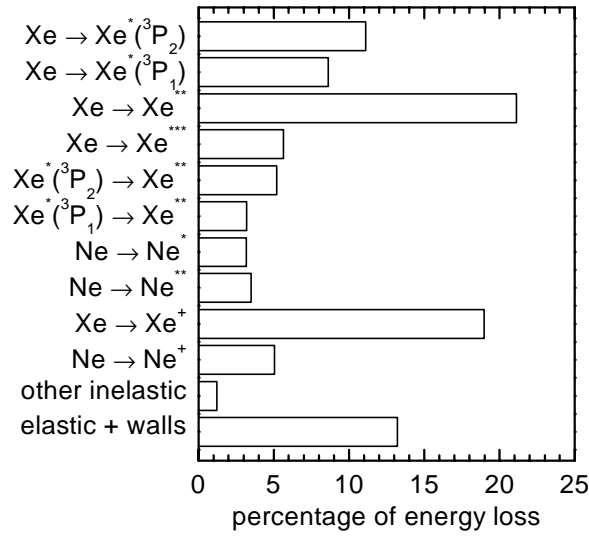


Figure 5.7. Breakdown of the loss of electron energy into the different electron impact excitation and ionization processes. The discharge conditions are indicated in the caption of Fig. 5.6.

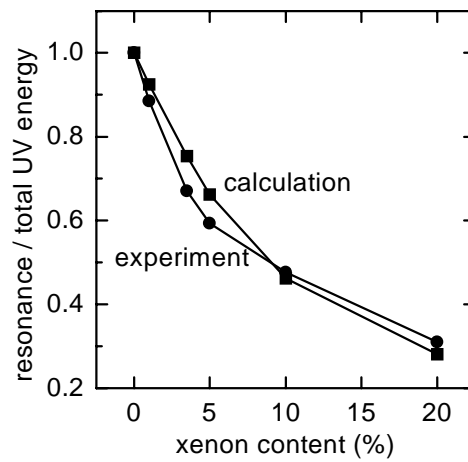


Figure 5.8. Ratio of the energy carried by 147 nm resonance photons and the total energy carried by UV photons. This plot compares the results of fluid simulations with the experimental data of Ref. [Sni99]. The discharge conditions are the same as with Fig. 5.6.

5.4 Parametric studies

The efficiency of the discharge in generating UV photons is defined as

$$\eta = \frac{\sum_{\lambda} W_{\lambda}}{\sum_p W_p}, \quad (5.5)$$

In view of the analysis given in the previous section, it is interesting to split the discharge efficiency into two partial efficiencies:

$$\rho_1 = \frac{W_e}{\sum_p W_p}, \quad (5.6)$$

$$\rho_2 = \sum_{\lambda} W_{\lambda} / W_e, \quad (5.7)$$

where W_e is the electrical energy transferred to the electrons, and $\eta = \rho_1 \rho_2$. The partial efficiency ρ_1 is the efficiency of the discharge in heating the electrons, ρ_2 is the efficiency of the electrons in generating UV radiation.

We now investigate how the η , ρ_1 , and ρ_2 are influenced by various discharge parameters. Wherever possible, we compare the simulation results with experimental data on the PDP efficacy, taken from Ref. [Ove00]. The efficacy is a measure for the light output of the display – weighted according to the sensitivity of the human vision – per unit of electrical input energy; it is thus not only determined by the discharge efficiency, but also by other factors, such as the efficiency of the phosphors in converting the UV radiation into visible light. Here we assume that these other factors stay constant.

We start with the influence of the secondary emission coefficient. In present day PDPs, where the surface is coated with magnesium oxide, this coefficient has been estimated to be around 0.45 for neon ions and below 0.001 for xenon ions. [Pun98a] Figure 5.9 shows that both η and ρ_1 increase with increasing secondary emission coefficient; ρ_2 is nearly unaffected. This result is not very surprising: The secondary emission coefficient directly determines the relative contributions of the electrons and the ions to the current density in the cathode fall, where the main particle heating occurs. The relative contribution of the electrons – and consequently ρ_1 – increases monotonically with increasing secondary emission coefficient. Of main importance is the secondary emission coefficient of the neon ions. For xenon ions, the secondary emission coefficient is so low that its exact value does not really matter: xenon hardly contributes to the secondary emission anyway.

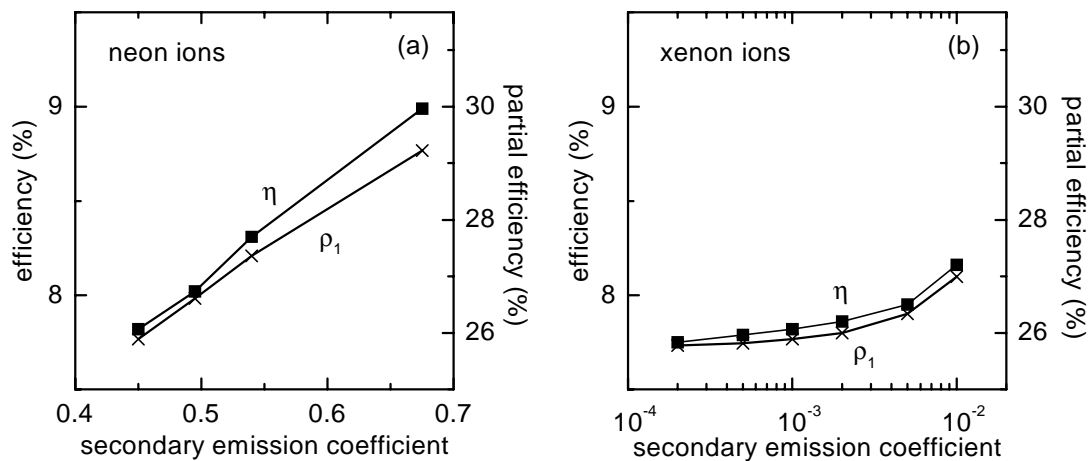


Figure 5.9. Calculated efficiency as a function of the secondary emission coefficient, for (a) neon ions and (b) xenon ions. The sustain voltage is 225 V, the sustain frequency is 250 kHz, the xenon percentage is 5%.

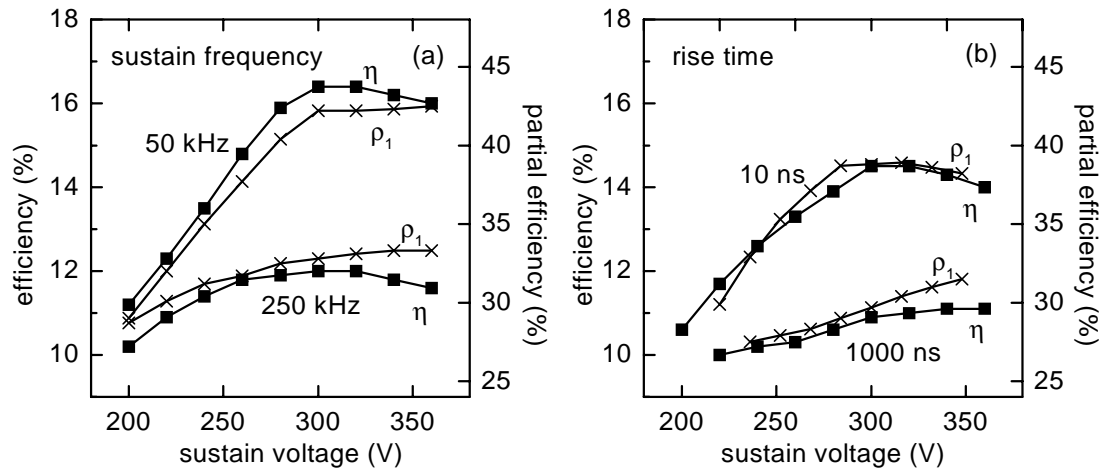


Figure 5.10. Calculated efficiency as a function of the sustain voltage, for (a) two different frequencies and a rise time of 100 ns, and (b) two different rise times and a frequency of 250 kHz. The xenon percentage is 5%.

The effect of the sustain voltage is shown in Fig. 5.10. For not too high sustain voltages, both η and ρ_1 increase with increasing voltage. This trend is also seen in the efficacy measurements shown in Fig. 5.11(a). The model reveals the mechanism behind this trend: As the voltage increases, the electric fields and the electron energies in the discharge go up. Since neon has a higher ionization energy than xenon, this leads to an increase of the relative contribution of neon to the total ion flux, which implies an increase of the average secondary emission coefficient. As we have seen before, this is favorable for the electron heating efficiency ρ_1 .

Figure 5.10(a) also shows that the sustain frequency has a strong effect on the calculated efficiency. This fact is known from experiments; see Fig. 5.11(b): Beyond a certain sustain frequency, the discharge efficiency drops dramatically. Also here, the underlying mechanism is easily found with the model: At low frequencies (50 kHz), there is a short while between the switching of the sustain voltage and the breakdown. At high frequencies (250 kHz), the plasma does not completely decay in between the discharges, which facilitates their ignition: breakdown now already occurs during the switching of the voltage. This is illustrated by Fig. 5.12. Due to the premature breakdown, the surface charge on the dielectric layer is already changed before the sustain voltage reaches its full value, so that the final voltage across the gas is lower. As we have seen before, this results in a lower ρ_1 . This observation suggests, that for high frequencies (250 kHz) the rise time of the sustain voltage might influence the efficiency. According to the simulation results shown in Fig. 5.10(b), this is indeed the case. For 50 kHz no influence of the rise time is found. We remark that these results are only of qualitative value: in general, the exact time between the switching of the voltage and the breakdown is not very accurately predicted by fluid models. [Pun98]

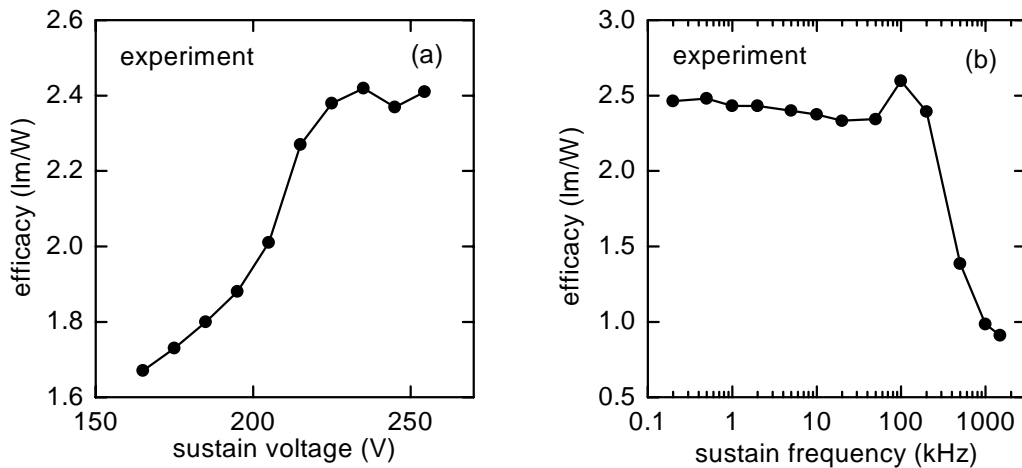


Figure 5.11. Measured luminous efficacy as a function of (a) the sustain voltage, where the frequency is 250 kHz, and (b) the sustain frequency, where the voltage is 225 V. The xenon percentage is 10%.

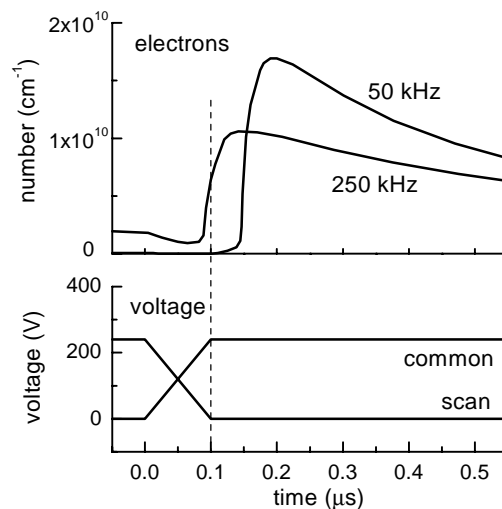


Figure 5.12. Comparison between the time evolution of the electron density for two different sustain frequencies. The xenon percentage is 5%.

As we have seen, the amplitude, frequency, and rise time of the sustain voltage mainly affect η via ρ_1 , leaving ρ_2 nearly unchanged. A parameter that can be expected to directly affect ρ_2 is the xenon content of the gas mixture. Figure 5.13(a) shows that the calculated efficiency increases with increasing percentage of xenon. This trend has been reported in the literature, e.g. in Ref. [Meu95], but is not fully reflected by the efficacy measurements shown in Fig. 5.13(b). We remark that it is known that the phosphor performance strongly depends on the UV wavelength, which is influenced as well by the xenon percentage. (See Fig. 5.8.) It appears from Fig. 5.13(a) that not only ρ_2 , but also ρ_1 is responsible for the increase of η with increasing xenon content.

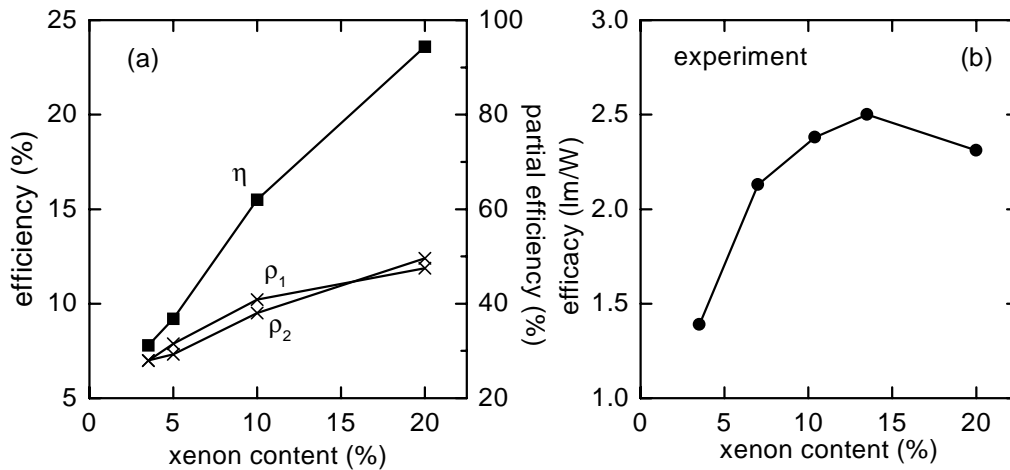


Figure 5.13. Influence of the percentage of xenon on (a) the calculated efficiency and (b) the measured efficacy. The sustain voltage is 260 V, the sustain frequency is 250 kHz.

5.5 Conclusions

The fluid model presented in Chapters 2-3 is capable of simulating the microdischarges in a coplanar-electrode PDP. We have reproduced a write pulse and a series of sustain pulses in one cell of the display.

From the simulation results, we have analyzed how the electrical input energy is dissipated in the cell. The largest part of the electrical energy is transferred to ions and subsequently to the gas and the surface. The electrical energy transferred to electrons is mostly used for ionization and excitation. The part used for xenon excitation largely ends up in UV radiation. The calculated fraction of the UV energy that is carried by resonance photons is in excellent agreement with experimental results.

We have studied how the energy loss mechanisms are influenced by several discharge parameters. The amplitude, frequency, and rise time of the sustain voltage mainly affect the losses due to ion heating. The xenon content also affects the conversion of electron energy into UV energy. The trends in the calculated discharge efficiency are in good agreement with measured trends in the luminous efficacy.

Chapter 6

A Monte Carlo modeling study of the electrons in PALC discharges*

6.1 Introduction

Fluid models, such as the model presented in Chapters 2-3 of this thesis, are widely used in the research of microdischarges for display technology. [Meu95, Pun98, Choi95, Vee96] These models provide a complete, self-consistent description of the discharge, at relatively low computational cost, using moments of the Boltzmann equation to describe the plasma particle transport, coupled to Poisson's equation to describe the electric field. However, the fluid models are based on restrictive assumptions for the electron energy distribution function (EEDF), thus failing to account for the possible non-equilibrium nature of the electrons in microdischarges. [Sur90, Ilc97]

Fluid models use mobilities μ , diffusion coefficients D , and reaction rate coefficients k as input parameters. In general these coefficients depend on the energy distributions of the plasma particles. For instance, the ionization rate coefficient k_i is determined by the EEDF:

$$k_i = \int_0^{\infty} \sigma_i(\varepsilon) \sqrt{2\varepsilon/m_e} f(\varepsilon) d\varepsilon, \quad (6.1)$$

where ε is the electron energy, σ_i is the ionization cross section, m_e is the electron mass, and f is the EEDF. However, in the fluid models the input coefficients are assumed to be functions of the local electric field E : [Meu95, Pun98, Vee96]

$$\mu = \mu(E), \quad D = D(E), \quad k = k(E), \quad (6.2)$$

or of the local electron mean energy $\bar{\varepsilon}$: [Cho95, Mey90, Boe95]

$$\mu_e = \mu_e(\bar{\varepsilon}), \quad D_e = D_e(\bar{\varepsilon}), \quad k = k(\bar{\varepsilon}). \quad (6.3)$$

The first approach (6.2), known as the local field approximation, is valid if the energy that plasma particles gain through acceleration by the electric field is locally balanced by collisional energy losses. In case of the second approach (6.3), the electron mean energy is evaluated in the fluid model as a function of time and space from an electron energy equation. This allows the electrons to be somewhat out of local field equilibrium; (6.3) is less strict than (6.2). The assumption (6.3) obviously only applies to coefficients involving electrons, hence the subscripts “ e ”.

The functions (6.2) or (6.3) that concern electrons, are obtained *a priori* from uniform-field EEDF calculations. As an example, Fig. 6.1 shows the equilibrium EEDF in helium, for various reduced fields and electron mean energies, as calculated with the Boltzmann solver BOLSIG [BoI96]. Such EEDFs are typically at the basis of the electron transport coefficients and the reaction rate coefficients used in fluid models.

* This chapter, in slightly altered form, will be published in: G. J. M. Hagelaar and G. M. W. Kroesen, “A Monte Carlo modeling study of the electrons in the microdischarges in plasma addressed liquid crystal displays,” Plasma Sources Sci. Techn..

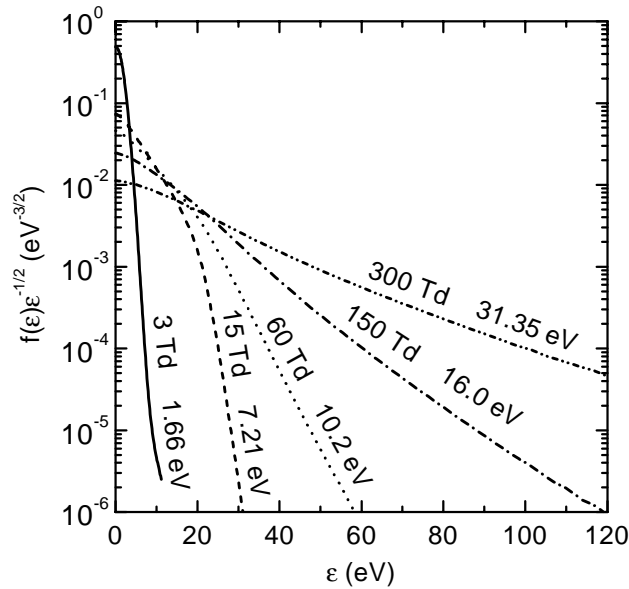


Figure 6.1. Equilibrium EEDF in helium, for different reduced electric fields and electron mean energies. These data are the result of calculations with the Boltzmann solver BOLSIG [Bol96]. Note that, following the convention, the figure shows $f(\epsilon)\epsilon^{-1/2}$ rather than $f(\epsilon)$, so that a Maxwellian distribution would be represented as a straight line.

The fluid model presented in Chapters 2-3 of this thesis includes an energy equation, with the assumption (6.3) made for the electron transport coefficients and the rate coefficients for excitation and ionization. In this chapter we investigate the validity of this fluid approach for PALC simulations, using a Monte Carlo model.

The Monte Carlo model simulates the path of individual electrons in the plasma. Since it only describes the electron transport, this model does not give a complete description of the discharge and requires the input of several plasma quantities, of which the most important is the electric field. We use the electric field obtained with the fluid model for this purpose. No attempt is made to couple the Monte Carlo results back to the fluid model and correct the electric field in a self-consistent way. Although our approach is therefore incomplete, it still permits a qualitative analysis, leading to more insight in the electron behavior and the shortcomings of the fluid model. Having the same electric field in the fluid and Monte Carlo calculations allows a direct local comparison of the results obtained with both methods.

This chapter is organized as follows: In Section 6.2 we outline the microdischarges in PALC displays and the fluid simulation of these discharges. Sections 6.3 and 6.4 provide a detailed description of the Monte Carlo model. Sections 6.5 and 6.6 present and discuss the results of the Monte Carlo calculations.

6.2 PALC discharges

The PALC operation principle is explained in Chapter 1 and will not be discussed here. We limit ourselves to outlining the PALC discharge geometry. The PALC discharges occur in dielectric discharge channels, between two thin metal electrodes that run all along the bottom of each channel. The inter-electrode gap is

about 250 μm . Compared to this, the length of the channels is virtually infinite, so that a two-dimensional (2D) description is fully satisfactory. Figure 6.2 shows a cross section through a typical PALC discharge channel; this is the geometry we will consider here. As a discharge gas we consider helium, this gas being used in most PALC displays. The gas pressure is typically 150 Torr. Two discharge regimes are of importance for the PALC operation: a direct current (DC) discharge between the channel electrodes and the afterglow of such DC discharge.

Figure 6.3 shows results of the fluid simulation of a DC discharge in a PALC channel. This simulation uses the relations (6.3), based on the equilibrium EEDFs shown in Fig. 6.1. Besides electrons, the fluid simulation involves atomic and molecular helium ions, and metastable excited helium atoms. According to Fig. 6.3, almost the entire applied voltage of 300 V stands across a small region in front of the cathode. The extremely high electric field in this cathode fall heats the electrons to an average energy of over 50 eV, resulting in a high local ionization rate. In view of the strong spatial variations of the electric field in the cathode fall, the assumption (6.3) can be expected to be a poor description of the reality in and around this region.

In the afterglow the situation is very different. The electric potential now constitutes a weak well for electrons. Figure 6.4 shows the potential and metastable density profiles 10 μs after the discharge was switched off, as calculated with the fluid model. In the helium afterglow, the enormous concentration of metastable excited atoms that develops during the discharge, is gradually converted into charged particles by metastable-metastable ionizations:



Although of minor importance during the discharge, the electrons and ions produced by these processes dominate the afterglow. [Ilc97] The electrons are generated with 15 or 17.4 eV of initial energy. For these energetic electrons, elastic energy loss is very inefficient, while at the same time ionization and excitation are out of the question in the absence of an accelerating electric field. Hence also for these electrons, the assumption (6.3) seems doubtful.

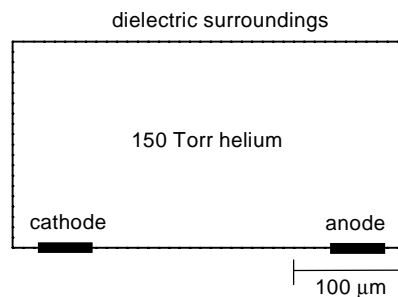


Figure 6.2. Schematic representation of the cross section through a typical PALC channel. This discharge geometry was used in the calculations.

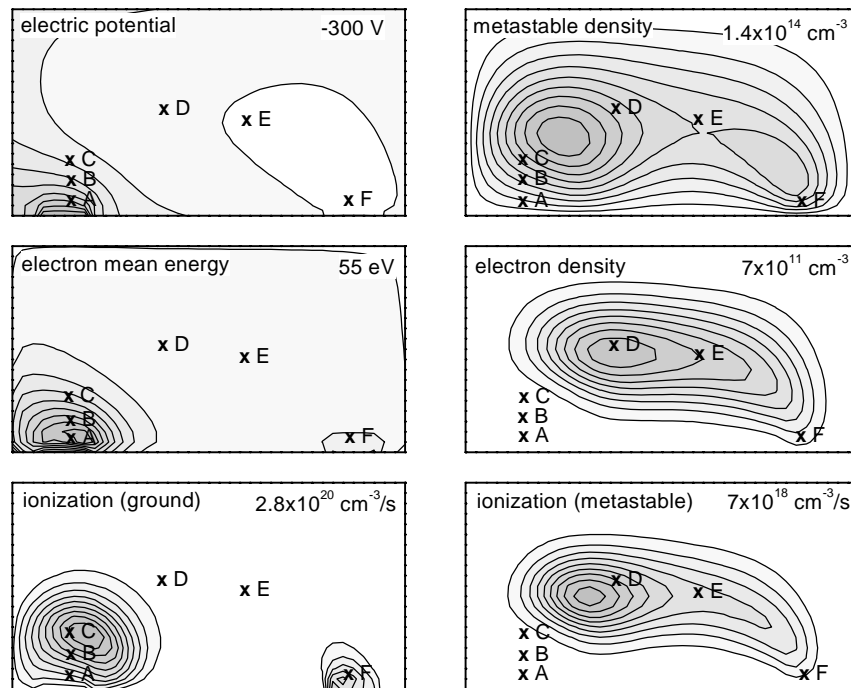


Figure 6.3. Spatial profiles of various plasma quantities in the fluid simulation of a DC discharge in the PALC geometry shown in Fig. 6.2. The applied voltage is 300 V, the helium pressure is 150 Torr. The marked points A through F are referred to elsewhere in this article. The increment of the contours is 1/10 times the maximum value indicated in the top right corner of each plot. The darkest regions correspond to this maximum value.

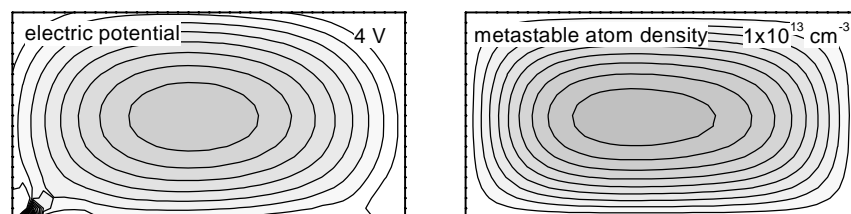


Figure 6.4. Spatial profiles of the electric potential and metastable density in the fluid simulation of the afterglow of the DC discharge shown in Fig. 6.3, 10 μ s after switching off the DC voltage. The increment of the contours is 1/10 times the maximum value indicated in the top right corner of each plot. The darkest regions correspond to this maximum value.

6.3 Overview of the Monte Carlo model

In the Monte Carlo model, a large number of electrons are followed, one by one, on their way through the plasma. The electric field that accelerates the electrons is obtained from the electric potential profile calculated with the fluid model. The occurrence and effect of collisions are treated by random numbers. Only electron interactions with ground state helium atoms and helium atoms in the metastable states

2^3S and 2^1S are taken into account. The 2^3S and 2^1S states are grouped together for this purpose into one composite metastable state He^* , of which the density is taken from the fluid model. The density of the ground state atoms is assumed to be constant at $4.924 \times 10^{18} \text{ cm}^{-3}$, corresponding to 150 Torr at 300 K. Besides elastic collisions, we take into account seven different excitation processes, with threshold energies ranging from 19.82 to 24.02 eV, de-excitation of He^* , and the ionization of the ground and metastable states, with threshold energies of 24.58 and 4.37 eV, respectively. Electron-electron and electron-ion interactions are neglected. The velocity of the atoms is assumed to be negligible compared to the electron velocity. Furthermore the center of mass of the collision partners is assumed not to move in the laboratory system.

The electrons are sampled randomly from various electron sources, and followed until they reach the channel walls. Three different electron sources are taken into account: secondary electron emission from the surface, and the two metastable-metastable ionization reactions (6.4) and (6.5). The rates of the source processes are taken from the fluid calculations; for the processes (6.4-5) these are proportional to the square of the metastable density, with the rate coefficients 9×10^{-10} and $2 \times 10^{-9} \text{ cm}^3/\text{s}$ [Ste82] as the respective proportionality constants. The initial energy of the sampled electrons is assumed to be 5 eV for those created by secondary emission [Mcd64], and 15 and 17.4 eV for those created by the metastable-metastable ionizations (6.4-5), respectively. The initial electron velocity is assumed to be isotropic. In addition to the electrons sampled from the secondary emission and metastable-metastable ionization sources, the new free electrons are followed from all electron impact ionization events occurring in the Monte Carlo simulation. This way the electron impact ionization sources are evaluated self-consistently in the Monte Carlo model. Reflection of electrons at the channel walls is neglected.

The plasma quantities that are taken from the fluid calculations – the electric potential, metastable density, and secondary emission rate – are assumed to be quasi-stationary, remaining unchanged during the time the electrons need to reach the channel walls; This makes these input quantities a function of space only. Since the fluid model only yields these data in the grid points of a 2D uniform Cartesian grid, interpolation is required. The grid points are spaced by $\Delta x = 10 \mu\text{m}$ horizontally and $\Delta y = 10 \mu\text{m}$ vertically. Within each grid cell we interpolate the potential V as

$$V(x, y) = a_{i,j}x + b_{i,j}y + c_{i,j}xy + d_{i,j}, \quad (6.6)$$

where x and y are horizontal and vertical position coordinates, and the indices I and j indicate a certain grid cell. The coefficients a through d are determined by the potentials in the four corners of the grid cell. The Cartesian components E_x and E_y of the electric field within the grid cell are then given by

$$E_x(x, y) = -a_{i,j} - c_{i,j}y, \quad (6.7)$$

$$E_y(x, y) = -b_{i,j} - c_{i,j}x. \quad (6.8)$$

The metastable atom density is interpolated analogous to (6.6).

For the storage of Monte Carlo simulation results, the entire discharge is divided in small 2D cells. We use the grid cells of the fluid model for this purpose. For every cell, certain information is recorded, such as the total (cumulative) time the electrons spend in the cell, and the electron energy and collision frequencies, integrated over this time. Afterwards this information is converted into the electron density, the electron mean energy, and the collision rates. In a similar way, the EEDF is determined in every cell, by storing the time of electron presence separately for a large number of small energy intervals.

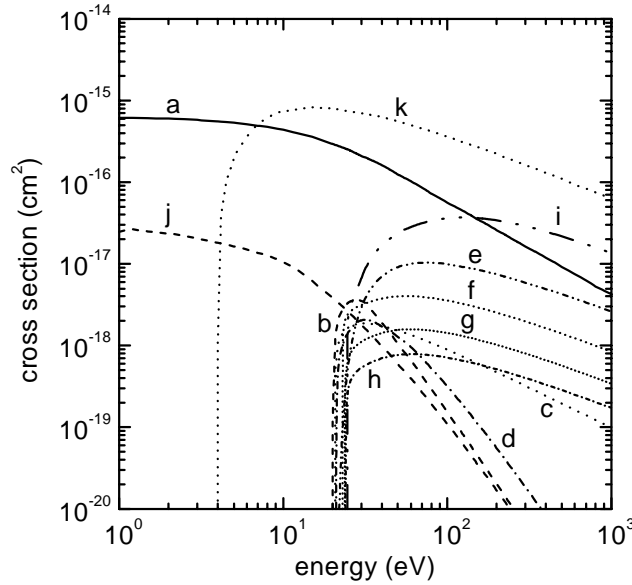


Figure 6.5. Cross sections of the electron collisions with helium atoms included in the Monte Carlo calculations. (a) elastic collisions, (b) excitation 2^3S , (c) excitation 2^1S , (d) excitation 2^3P , (e) excitation 2^1P , (f) total excitation $3 S,P,D$, (g) total excitation $4 S,P,D$, (h) total excitation $5 S,P,D$, (i) ionization 1^1S (ground state), (j) de-excitation $2 S$ (metastable states), (k) ionization $2 S$ (metastable states). These data were taken from Ref. [Bol96], except for the curve k, which was taken from Ref. [Jan87]. Curve j was obtained from b and c by detailed balancing.

6.4 The simulation of an electron path

In this section we describe in detail how the path of an individual electron is simulated. Consider a test electron somewhere in the plasma at a moment $t = t_0$. The probability P that the electron has no collision before time t is given by

$$P(t) = \exp\left(-\int_{t_0}^t v_t(t') dt'\right), \quad (6.9)$$

where v_t is the total collision frequency

$$v_t(\mathbf{x}, \varepsilon) = \sum_k v_k(\mathbf{x}, \varepsilon) = \sum_k n_k(\mathbf{x}) \sigma_k(\varepsilon) \sqrt{\frac{2\varepsilon}{m_e}}, \quad (6.10)$$

which may change in time as the electron moves, since it may depend on the position \mathbf{x} and the electron energy ε . The summation in (6.10) is over all possible collision types, where v_k is the collision frequency, n_k is the density of the target species and σ_k is the collision cross section. The cross sections $\sigma_k(\varepsilon)$ of all collision types that we take into account are shown in Fig. 6.5. The probability that the first collision (after t_0) occurs within an infinitesimal time interval dt starting at t is then

$$p(t)dt = P(t) - P(t+dt) = v_t(t) \exp\left(-\int_{t_0}^t v_t(t') dt'\right) dt. \quad (6.11)$$

A random collision time t_c can be determined according to this probability distribution from the following equation:

$$\int_{t_0}^{t_c} v_t(t) \exp\left(-\int_{t_0}^t v_t(t') dt'\right) dt = r_1 \int_{t_0}^{\infty} v_t(t) \exp\left(-\int_{t_0}^t v_t(t') dt'\right) dt, \quad (6.12)$$

where r_1 is a random number, uniformly distributed between 0 and 1, as generated by a random number computer routine. The calculation of t_c from equation (6.12) is greatly simplified by the use of the so-called null collision method [Sku68]. This method introduces an imaginary collision type: the null collision, which has no effect whatsoever on the electron. The frequency v_0 of the null collision is chosen such that the total collision frequency is completely independent of the electron energy and position, and thus constant in time:

$$v_t' = v_0(\mathbf{x}, \varepsilon) + v_t(\mathbf{x}, \varepsilon) = \max_{\mathbf{x}, \varepsilon} v_t(\mathbf{x}, \varepsilon), \quad (6.13)$$

where v_t is the total frequency of the real collisions (6.10), and v_t' is the total collision frequency including v_0 . Using v_t' instead of $v_t(t)$, equation (6.12) reduces to

$$t_c = t_0 - \frac{1}{v_t'} \ln(1 - r_1). \quad (6.14)$$

Between t_0 and t_c the electron moves freely. Its path is calculated by integrating the equation of motion

$$\frac{d^2 \mathbf{x}}{dt^2} = -\frac{e}{m_e} \mathbf{E}(\mathbf{x}), \quad (6.15)$$

where e is the elementary charge and \mathbf{E} is the electric field. The electric field being an arbitrary function of \mathbf{x} , this integration cannot be carried out analytically, and is done numerically, using small time steps Δt . We use the so-called leapfrog method: [Bir91]

$$\mathbf{x}_{l+1} = \mathbf{x}_l + \mathbf{v}_l \Delta t - \frac{e}{2m_e} \mathbf{E}(\mathbf{x}_l) (\Delta t)^2, \quad (6.16)$$

$$\mathbf{v}_{l+1} = \mathbf{v}_l - \frac{e}{2m_e} (\mathbf{E}(\mathbf{x}_l) + \mathbf{E}(\mathbf{x}_{l+1})) \Delta t, \quad (6.17)$$

where the subscript l refers to a moment in time, with $t_{l+1} = t_l + \Delta t$. The time step is chosen such, that the distance traveled within this time step is much smaller than the size of the grid cells of the fluid model: $\Delta t < 0.01 \Delta x/v_x$ and $\Delta t < 0.01 \Delta y/v_y$, v_x and v_y being the horizontal and vertical velocity components. The leapfrog method (6.16-17) can be shown to conserve the particle energy for one-dimensional parabolic electric potential profiles. For arbitrary potential profiles however, the integration may lead to numerical heating or cooling of the electron. We circumvent this effect by rescaling the electron velocity from time to time, keeping the sum of the potential and kinetic energy constant in between the collisions.

Once the energy ε_c and the position \mathbf{x}_c at the moment of the collision are known, the nature k_c of the collision is determined from another uniformly distributed random number r_2 between 0 and 1, taking into account the relative probabilities of the various collision types:

$$\sum_{k=0}^{k_c-1} v_k(\mathbf{x}_c, \varepsilon_c) < r_2 v_t' < \sum_{k=0}^{k_c} v_k(\mathbf{x}_c, \varepsilon_c). \quad (6.18)$$

Since we use the null collision method to find t_c , one of the possible collision types in equation (6.18) is the null collision, which has no effect on the electron. The other collision types affect the electron velocity and energy.

The change in the direction of the electron velocity is described by two angles, an azimuthal angle ϕ , and a scattering angle θ . For the sake of symmetry, the azimuthal

angle is distributed isotropically. A random azimuthal angle ϕ_c is found straightforwardly as

$$\phi_c = 2\pi r_3, \quad (6.19)$$

where r_3 is a uniformly distributed random number between 0 and 1. In contrast, the scattering angle is generally anisotropically distributed. The probability for an electron with incident energy ε_c to be scattered over an angle θ , is determined by the differential cross section $I(\varepsilon_c, \theta)$. One can calculate a random scattering angle θ_c from a uniformly distributed random number r_4 between 0 and 1, using the following equation:

$$2\pi \int_0^{\theta_c} I(\varepsilon_c, \theta) \sin \theta d\theta = r_4 \sigma(\varepsilon_c). \quad (6.20)$$

For the various collision types, we use the angular dependence included in various theoretical approximations of I , as described in the following. For elastic collisions, we assume that

$$I(\varepsilon_c, \theta) = \frac{\sigma(\varepsilon_c) \eta(\eta + 1)}{\pi(2\eta + 1 - \cos \theta)^2}, \quad (6.21)$$

which results from an approximation to Born's approximation [Mot65, Mas69]. In this equation, η is a Coulomb screening parameter which depends on the electron energy ε_c :

$$\eta = 10.9Z^{2/3}(\text{eV})/\varepsilon_c, \quad (6.22)$$

with Z the atom number of the target species and ε_c in eV. According to equations (6.21-22), the elastic scattering is roughly isotropic for low energies, whereas in the high energy limit the electrons are forwardly scattered. Substituting (6.21) in (6.20), we find the following expression for a random elastic scattering angle θ_c : [Pit98]

$$\cos \theta_c = \frac{\eta + 1 - (2\eta + 1)r_4}{\eta + 1 - r_4}. \quad (6.23)$$

For inelastic collisions leading to optically allowed atomic transitions, we use

$$I(\varepsilon_c, \theta) = \frac{\sigma(\varepsilon_c) \beta}{2\pi \ln[(1 + \beta)/(1 - \beta)](1 + \beta^2 - 2\beta \cos \theta)}, \quad (6.24)$$

where $\beta = \sqrt{1 - \varepsilon_{mn}/\varepsilon_c}$, ε_{mn} being the atomic transition energy. This equation was obtained from a small-angle approximation to Born's approximation [Mas69], and states that low energy electrons are more isotropically scattered, while high energy electrons tend to be more forwardly scattered. Substitution in equation (6.20) gives us the following random scattering angle:

$$\cos \theta_c = \frac{1 + \beta^2 - (1 - \beta)^2 \exp[2r_4 \ln[(1 + \beta)/(1 - \beta)]]}{2\beta}. \quad (6.25)$$

For inelastic collisions involving prohibited atomic transitions, we assume the electron scattering to be always isotropic, regardless of the energy:

$$I(\varepsilon_c, \theta) = \frac{\sigma(\varepsilon_c)}{4\pi}, \quad (6.26)$$

so that a random scattering angle is given by

$$\cos \theta_c = 1 - 2r_4. \quad (6.27)$$

In addition to changing the direction of the electron velocity, the collision affects the electron energy. For elastic collisions, the energy ε_1 after the collision is given by [Mcd64]

$$\varepsilon_1 = [1 - 2(m_e/M)\cos\theta_c]\varepsilon_c, \quad (6.28)$$

where m_e is the electron mass and M is the mass of the target particle. The electron energy after an inelastic collision is straightforwardly

$$\varepsilon_1 = \varepsilon_c - \varepsilon_{mn}. \quad (6.29)$$

In case of ionization, this energy is redistributed between the original electron (primary electron) and the new free electron (secondary electron). The probability for an electron with incident energy ε_c to produce a secondary electron at energy ε , is determined by $I_\varepsilon(\varepsilon_c, \varepsilon)$, the differential cross section with respect to the secondary electron energy. A random value ε_2 for the energy of the secondary electron is found from a uniformly distributed random number r_5 between 0 and 1, using the following equation:

$$\int_0^{\varepsilon_2} I_\varepsilon(\varepsilon_c, \varepsilon) d\varepsilon = r_5 \sigma_i(\varepsilon_c), \quad (6.30)$$

where σ_i is the ionization cross section. We use the empirical formula found by Opal and co-workers [Opa71], as in Ref. [Yos83]:

$$I_\varepsilon(\varepsilon_c, \varepsilon) = \frac{\sigma_i(\varepsilon_c)}{\omega \arctan((\varepsilon_c - \varepsilon_i)/(2\omega))(1 + \varepsilon^2/\omega^2)}, \quad (6.31)$$

in which ε_i is the ionization threshold and ω is a fitting parameter. For helium, $\omega = 15$ eV is an appropriate choice. Substituting (6.31) into (6.30) and integrating yields

$$\varepsilon_2 = \omega \tan[r_5 \arctan((\varepsilon_c - \varepsilon_i)/(2\omega))] \quad (6.32)$$

The energy of the primary electron is then

$$\varepsilon_1 = \varepsilon_c - \varepsilon_i - \varepsilon_2. \quad (6.33)$$

Given the scattering angle θ_c , the azimuthal angle ϕ_c , and the new energy ε_1 , the electron velocity after the collision can be calculated. The Cartesian components of the velocity \mathbf{v}_1 after the collision are given by

$$v_{1,x} = \frac{v_1}{v_c} \left(\frac{v_{c,x}v_{c,z}}{u} \sin\theta \cos\phi - \frac{v_{c,y}v_c}{u} \sin\theta \sin\phi + v_{c,x} \cos\theta \right), \quad (6.34)$$

$$v_{1,y} = \frac{v_1}{v_c} \left(\frac{v_{c,y}v_{c,z}}{u} \sin\theta \cos\phi + \frac{v_{c,x}v_c}{u} \sin\theta \sin\phi + v_{c,y} \cos\theta \right), \quad (6.35)$$

where $u = \sqrt{v_{c,x}^2 + v_{c,y}^2}$, $v_c = \sqrt{2\varepsilon_c/m_e}$ and $v_1 = \sqrt{2\varepsilon_1/m_e}$.

The procedure described in this section is repeated until the electron reaches the wall.

6.5 Results for a DC discharge

We simulated the paths of one million electrons in a DC discharge in a PALC channel, assuming the electric potential and metastable density profiles shown in the top two plots of Fig. 6.3. Figure 6.6 shows the resulting electron density, mean energy and ionization profiles. These plots can be compared directly with the last four plots of Fig. 6.3. At first sight the agreement between the results of the Monte Carlo and fluid

models is quite reasonable. Especially the electron density obtained with both methods is very similar. The largest difference occurs in the rate of ground state ionization. In the fluid model this reaction is limited to the cathode fall region, whereas in the Monte Carlo model it is spread out over a much larger area. Yet the volume integrals of both ionization rates are virtually the same, which gives some sort of explanation for the similarity of the electron densities.

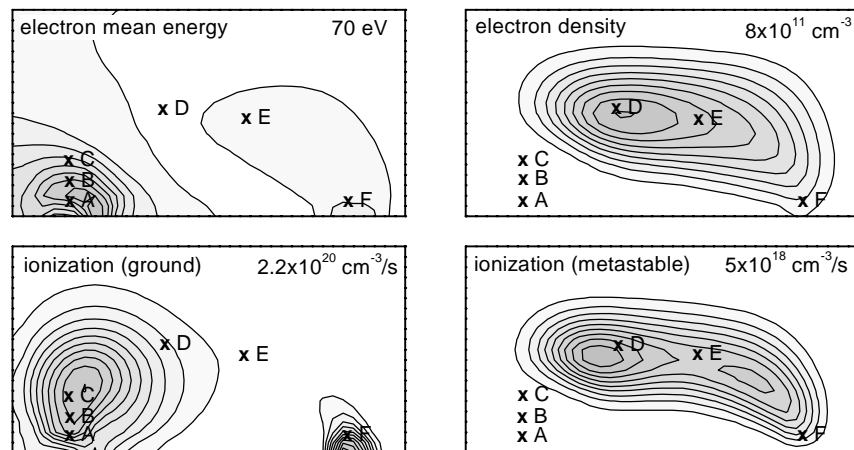


Figure 6.6. Results of the Monte Carlo simulation of electrons in a DC discharge in a PALC channel. This figure corresponds to the fluid calculation represented in Fig. 6.3. The marked points A through F are referred to in the text and in Fig. 6.7. The increment of the contours is 1/10 times the maximum value indicated in the top right corner of each plot. The darkest regions correspond to this maximum value.

The differences between the fluid and Monte Carlo model results become clear if we take a look at the EEDF. Figure 6.7 shows the EEDF at different points in the DC discharge. In addition to the EEDF obtained with the Monte Carlo model, this figure shows the equilibrium EEDFs that correspond to the local electric field and to the local electron mean energy calculated with the fluid model. This latter EEDF is the one that is implicitly assumed in the fluid model, through the relations (6.3).

In the point A in the cathode fall, the EEDF calculated with the Monte Carlo model has no tail: no electrons have an energy over 130 eV. This non-equilibrium phenomenon results from the fact that the electrons started out from the cathode with only 5 eV of energy, and have been subject to acceleration only for a limited time since then. The peak at the high energy end of the distribution represents a group of fast electrons that have not yet undergone any collision up to this point. Note that the peak is somewhat broadened by the non-negligible size of the cell over which was averaged; the position of the peak corresponds to the average potential difference between this cell and the cathode. Moving away from the cathode, from point A to point B to point C, the fast electron peak is decreasing and shifted towards higher energy. A second, slightly lower, peak can be observed at about 25 eV lower energy than the first peak. The energy difference between the peaks corresponds to the ionization energy of helium atoms; obviously the second peak represents the electrons emitted from the cathode, that have ionized once.

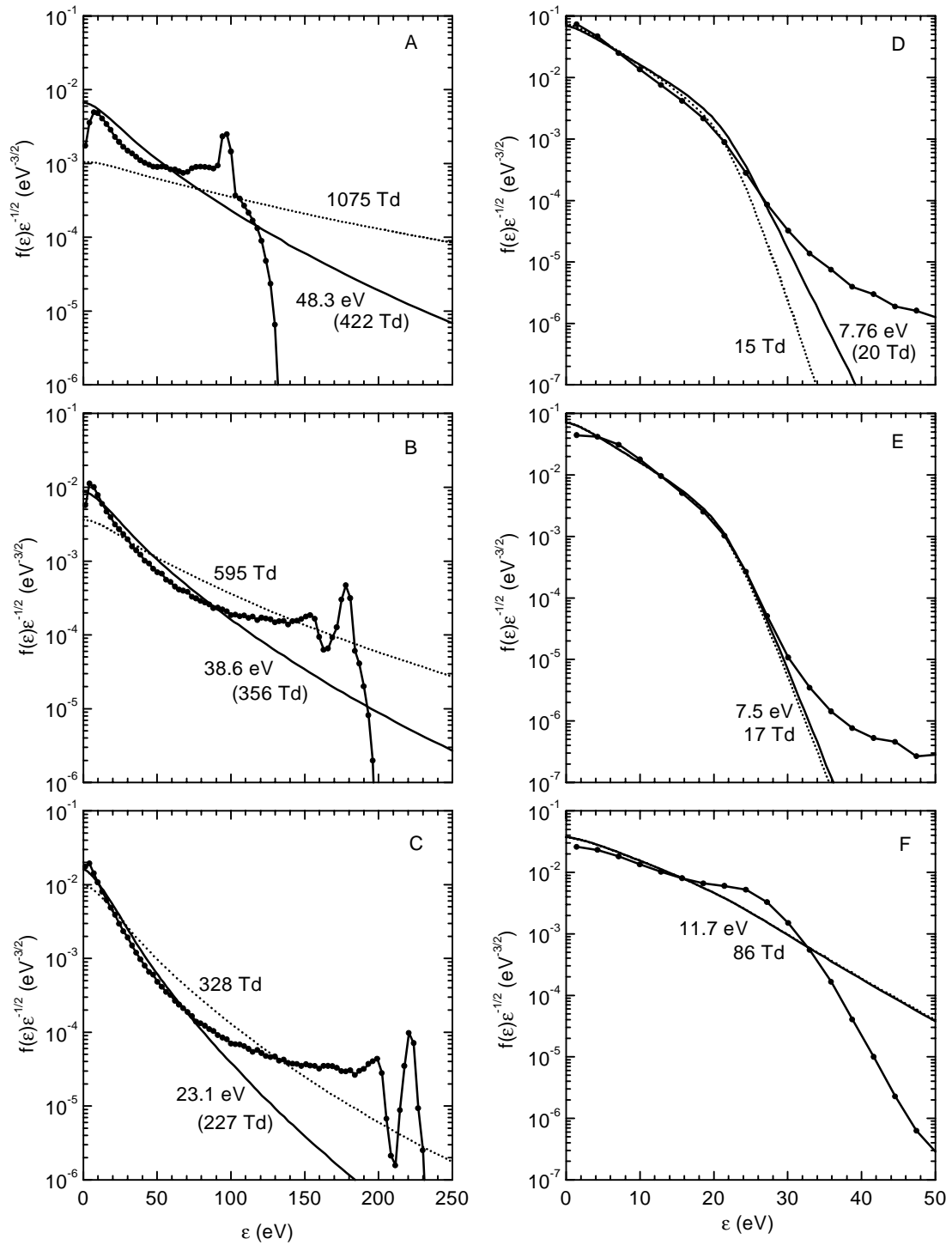


Figure 6.7. The EEDF at different points in a DC discharge in the PALC geometry. The exact positions corresponding to the plots A through F are marked in the Figs. 6.3 and 6.6. In each of the plots, the EEDF obtained with the Monte Carlo model is represented by connected dots (●). The solid line (—) shows the EEDF that is implicitly assumed in the fluid model by the relations (6.3). The dashed line (---) represents the equilibrium EEDF corresponding to the local electric field. The mean energies and reduced fields pertaining to the equilibrium EEDFs are indicated with the curves.

Still further away from the cathode, in point D, the vast majority of the electrons is in some low energy bulk distribution, which looks remarkably like the equilibrium EEDF up to an energy of about 30 eV. Beyond that energy, a remainder of the fast electron groups from the cathode is still present. At the center of the plasma E, the resemblance with the equilibrium EEDF is even better, but even here the fast electrons still exist. Finally, in the point F in front of the anode, the tail of the EEDF is depopulated again. In this so-called anode fall region the electric field is considerably higher than in the center of the channel, which causes the electron mean energy to increase as the electrons approach the anode. Due to the very limited size of the anode fall, field equilibrium cannot be established, and the high energy tail remains underpopulated. Although less pronounced, this phenomenon is very similar to the absence of the high energy tail observed in the cathode fall.

The EEDF assumed by the fluid model does not incorporate the non-equilibrium phenomena seen in the Monte Carlo results, such as the existence of groups of fast electrons that have undergone none or only a few collisions, and the absence of the high energy tail. However, in the cathode fall it gives a much better description than the local field equilibrium EEDF. In the plasma and the anode fall the EEDF assumed by the fluid model is equal to the EEDF of local field equilibrium. In general, the low energy bulk of the electrons is much better described than the fast electrons that are capable of ground state ionization. This is the reason why the agreement between the Monte Carlo and fluid model results is much better for the electron density and the excited state ionization than for the ground state ionization.

Note that although the bulk electron density seems to be correct in the fluid model, the errors in the ionization profile may affect the ion density in the cathode fall, and consequently also the electric field.

6.6 Results for the afterglow

The Monte Carlo simulation of electrons in the afterglow poses several problems: First, the afterglow is not a stationary situation. The assumption that the electric potential and the metastable density are constant, is therefore only justified in case the lifetime of individual free electrons is negligible compared to the plasma decay time, which is in the order of 10^{-5} s (see Chapter 4). Moreover, in the afterglow the electric potential constitutes weak well for electrons. Due to the neglect of electron-electron interactions and the helium atom temperature, low energy electrons tend to get eternally trapped in this potential well, eventually losing all their energy. This artifact can only be prevented by tricks that affect the reliability of the Monte Carlo calculations.

However, the dominant electrons in the helium afterglow are generated by metastable-metastable ionizations (6.4-5) with 15 or 17.4 eV of initial energy. For this particular group of electrons, the problems mentioned above are not severe. We simulated the paths of one million of these electrons in the afterglow, assuming the electric potential and metastable density profiles shown in Fig. 6.4. We followed the electrons for a maximum time of 10^{-8} s; if an electron had not yet reached the wall by then, it was assumed to just miraculously disappear. This trick to avoid eternal trapping was only needed for less than 100 electrons, which is a negligible number.

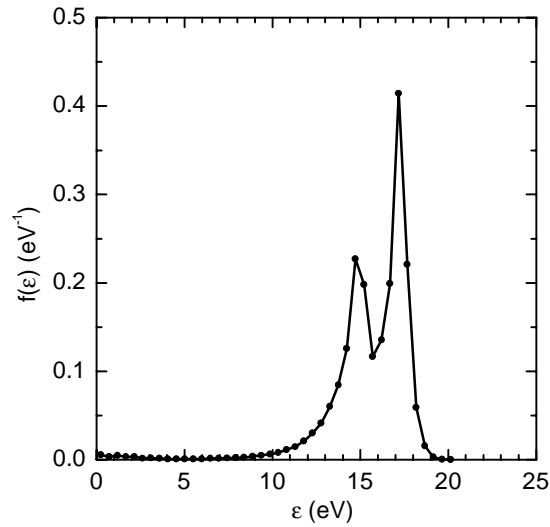


Figure 6.8. The EEDF of the electrons produced by metastable-metastable ionizations in the afterglow, calculated with the Monte Carlo model.

Figure 6.8 shows the calculated EEDF in the center of the channel; on other positions in the channel it looks very similar. This EEDF is entirely different from any equilibrium EEDF. Apparently, most electrons lose only a small part of their initial energy. Based on this observation, we decided to consider the electrons produced by metastable-metastable processes as a separate group in the fluid model. Instead of making assumption (6.3), we assumed that the mobility and diffusion coefficient of this electron group have constant values:

$$\mu_e = 4.56 \times 10^3 \text{ cm}^2/\text{Vs}, D_e = 4.56 \times 10^4 \text{ cm}^2/\text{s}, \quad (6.36)$$

based on a Dirac δ function at 15 eV for the EEDF. With this approach, the results of the fluid model are in excellent agreement with the Monte Carlo results. This is illustrated by Fig. 6.9, which shows for both models the calculated density of the electrons produced by metastable-metastable ionization.

In fact, the potential and metastable density profile shown in Fig. 6.4 – input data for the Monte Carlo model – were obtained by distinguishing the two electron groups in the fluid model. Note that this last point is crucial for the validity of the Monte Carlo analysis given here: If, in the fluid model, we would have treated all electrons by the assumptions (6.3), that would have been completely inconsistent with the Monte Carlo results. This would have made these results invalid, since they are based on the potential profile obtained with the fluid model. Using the assumptions (6.36), however, there is no essential inconsistency between the fluid model and the Monte Carlo results.

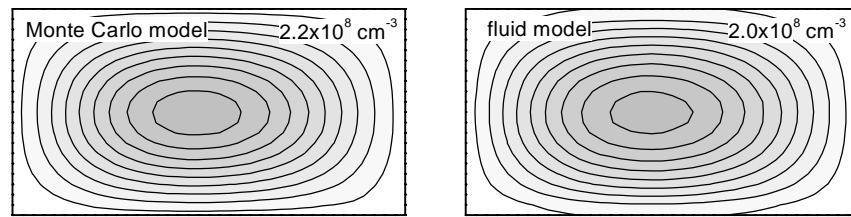


Figure 6.9. Comparison between the electron density profiles in the afterglow, calculated with the Monte Carlo model, and with the fluid model, where the electrons were assumed to be mono-energetic at 15 eV. The increment of the contours is 1/10 times the maximum value indicated in the top right corner of each plot. The darkest regions correspond to this maximum value.

6.7 Conclusions

We have developed a Monte Carlo model for the electrons in the microdischarges occurring in PALC displays. We have used the model to obtain insight in the validity of the fluid approach for the simulation of PALC discharges, with helium as a discharge gas. In general the Monte Carlo results are in reasonable agreement with the results of fluid simulations.

In a DC discharge in a PALC channel, the EEDF calculated with the Monte Carlo model displays several non-equilibrium phenomena, such as peaks of fast electrons that have undergone none or only a few collisions, and the absence of the high energy tail. The EEDF that is implicitly assumed by the fluid model does not include these features, but still gives a much better description than the EEDF of local field equilibrium. The poorest description is given of the high energy electrons capable of ground state ionization. Whereas the bulk electron density in the fluid model is correct, the ionization rate is too much localized in front of the cathode.

The electrons that are created by metastable-metastable ionization during the helium afterglow in a PALC channel, hardly lose any of their initial energy before they are lost at the channel walls. The Monte Carlo calculations reveal that the EEDF of these electrons is completely different from any equilibrium EEDF, and is better approximated by a Dirac δ function at 15 eV. If we use this simple approximation in the fluid model, the calculated results are in very good agreement with the results of the Monte Carlo model.

Chapter 7

The energy distribution of ions and fast neutrals^{*}

7.1 Introduction

In both PALC and PDP displays, an incident flux of energetic plasma particles causes damage to the materials surrounding the microdischarges, thus limiting the lifetime of the displays. Understanding and prediction of this phenomenon requires knowledge of the energy distribution of the plasma particles impinging on the material surfaces. Of particular interest are ions and fast neutrals with an energy beyond the sputtering threshold, which varies from 10 to 100 eV, depending on surface material and incident particle species. [Mat84]

Research on microdischarges leans heavily on discharge modeling tools, in view of experimental difficulties due to their small size. By the use of self-consistent fluid models a good picture can be obtained of the electric fields and the particle densities and fluxes in microdischarges. [Meu95, Pun98, Choi95, Vee97] However, these fluid models do not describe the energy distributions of the plasma particles. In this chapter, we attempt to predict – on the basis of the results of fluid models – the energy distribution of ions and fast neutrals impinging on the surface. We pursue both an elementary theoretical approach (Sections 2 and 3) and a more comprehensive Monte Carlo approach (Section 4).

Although many different designs exist for the PDP and PALC discharges, they all have very similar discharge characteristics. The inter-electrode gap is on the order of a few hundred microns, the gas pressure is a few hundred Torr. Typical discharge voltages are a few hundred Volts, where the reduced electric field can reach values of up to $500 \text{ V cm}^{-1} \text{ Torr}^{-1}$ locally in front of the surface. Figure 7.1 shows some typical profiles of the electric potential in the microdischarge sheaths. The sheaths are always highly collisional: typically the ion mean free path is in the submicron range, about two orders of magnitude smaller than the sheath thickness. This implies that the ion energy distribution is determined by the local electric field rather than the total sheath voltage, and that the ion mean energy is only a small fraction of this voltage.

The discharge gas used in PDP and PALC displays is typically a rare gas or a mixture of rare gases. The main ion species are ionized discharge gas atoms. Typical ionization rate profiles are shown in Fig. 7.1. Molecular ions, such as He_2^+ and Xe_2^+ , are also found, but tend to get dissociated in the sheaths: beyond a certain energy limit on the order of 1 eV, the dissociation cross sections become so large that survival is extremely unlikely. [Mai75, Gro73]

We thus focus on atomic rare gas ions, moving toward the surface in a highly collisional sheath.

^{*} This chapter, in slightly altered form, has been published in: G. J. M. Hagelaar, G. M. W. Kroesen, and M. H. Klein, "Ion energy distribution in microdischarges for display technology," *J. Appl. Phys.*, (2000).

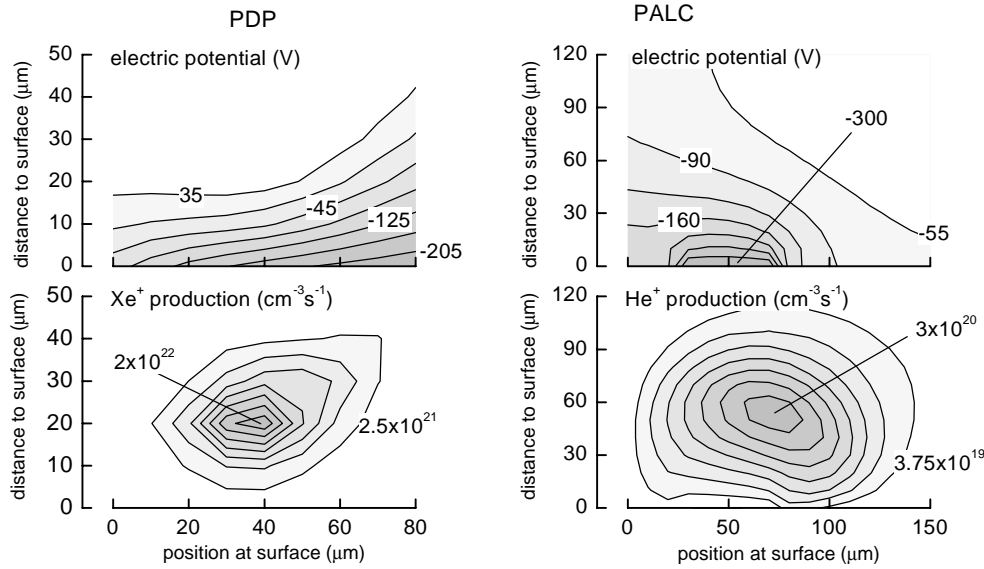


Figure 7.1. Contour plots of the electric potential and the ion formation rate in front of the surface, at the position and the moment where the incident ion flux is the highest and the most energetic. A typical situation is shown for an AC PDP discharge in Ne-Xe 5% (left) and for a PALC discharge in He (right). These profiles were obtained with a fluid model.

7.2 The ion energy distribution

On their path the ions undergo collisions predominantly with neutral gas particles that are virtually at rest. Two different collision types are to be distinguished. Firstly, there are elastic collisions, leading to the (more or less isotropic) scattering of the ions in the center of mass (CM) system of the colliding particles. Secondly, when moving in their parent gas, the ions are subject to symmetric charge transfer collisions. In such a collision the ion charge is transferred to a parent gas particle, while the velocities of both particles remain largely unaffected: after the collision the ion is virtually at rest. A symmetric charge transfer collision is equivalent to an elastic collision where the ion is scattered over 180° in the CM system. [Phe94] As appears from Fig. 7.2, the cross sections of these collision processes are approximately constant over the energy range of interest. The symmetric charge transfer cross section is usually considerably larger than the cross section for elastic collisions.

If symmetric charge transfer is the dominant collision process, the ion energy distribution can be predicted with an elementary theoretical approach. Consider an ion with mass m and charge q in a uniform electrostatic field E , being subject to a constant acceleration qE/m . Assume that the ion loses all its energy when it collides. The ion energy as a function of the time t after a collision is then

$$\varepsilon = \frac{q^2 E^2}{2m} t^2. \quad (7.1)$$

When looking at an ensemble of such ions, the fraction of them with an energy in between ε and $\varepsilon + d\varepsilon$ is proportional to the average time \overline{dt} that one ion spends in this energy interval during a free path:

$$f(\varepsilon)d\varepsilon \propto \overline{dt}. \quad (7.2)$$

According to equation (7.1), the ion reaches the energy interval after

$$t = \frac{\sqrt{2m\varepsilon}}{qE}, \quad (7.3)$$

that is, if it does not collide before. It then stays in the interval for a while dt

$$dt = \left(\frac{dt}{d\varepsilon} \right) d\varepsilon = \frac{1}{qE} \sqrt{\frac{m}{2\varepsilon}} d\varepsilon. \quad (7.4)$$

On average, the time spent in the interval is

$$\overline{dt} = P(t)dt, \quad (7.5)$$

where P is the probability that no collision takes place before time t , which is related to the collision frequency ν according to

$$P(t) = \exp\left(-\int_0^t \nu(t')dt'\right). \quad (7.6)$$

Assuming the gas particles to be at rest, the collision frequency is a function of ε :

$$\nu(\varepsilon) = N\sigma(\varepsilon)\sqrt{\frac{2\varepsilon}{m}}, \quad (7.7)$$

where N is the gas particle density and σ the collision cross section. On combining the equations (7.2-7), one finds straightforwardly that

$$f(\varepsilon)d\varepsilon \propto \frac{1}{\sqrt{\varepsilon}} \exp\left(-\frac{N}{qE} \int_0^\varepsilon \sigma(\varepsilon')d\varepsilon'\right) d\varepsilon. \quad (7.8)$$

The appropriate proportionality constant in relation (7.8) can be found by normalizing the distribution to unity. For a constant collision cross section this yields

$$f(\varepsilon)d\varepsilon = \frac{1}{\sqrt{\pi\omega\varepsilon}} \exp\left(-\frac{\varepsilon}{\omega}\right) d\varepsilon, \quad (7.9)$$

where the parameter ω is given by

$$\omega = \frac{qE}{N\sigma}. \quad (7.10)$$

Averaging ε over the distribution (7.9) shows that ω is equal to twice the ion mean energy. Note that the distribution function (7.9) is essentially different from the Maxwellian distribution function: the Maxwellian function is zero at $\varepsilon = 0$, whereas function (7.9) goes to infinity for $\varepsilon \rightarrow 0$. Realize furthermore that all the ions move in the direction of the electric field: the ion motion is as anisotropic as can be. The ion drift velocity w is hence found by simply averaging the velocity $(2\varepsilon/m)^{1/2}$ over distribution (7.9):

$$w = \int_0^\infty \sqrt{\frac{2\varepsilon}{m}} f(\varepsilon)d\varepsilon = \sqrt{\frac{2\omega}{\pi m}}. \quad (7.11)$$

Rearranging (11) yields an alternative expression for ω :

$$\omega = \frac{\pi}{2} m w^2, \quad (7.12)$$

which is of great practical use, because it provides a way to estimate the ion energy distribution merely from the ion drift velocity, which is calculated in fluid models.

Expression (7.9) represents the energy distribution of the ion density. It is important to realize, that this is not the energy distribution of the ion flux hitting the surface. In view of the fact that all ions move in exactly the same direction, the latter

distribution can be found by weighting (7.9) with the ion velocity $(2\varepsilon/m)^{1/2}$. After normalization, we find

$$g(\varepsilon)d\varepsilon = \frac{1}{\omega} \exp\left(-\frac{\varepsilon}{\omega}\right)d\varepsilon \quad (7.13)$$

for the ion flux energy distribution. It follows from averaging ε over distribution (7.13) that the average energy of the incident ions is equal to ω , twice the ion mean energy.

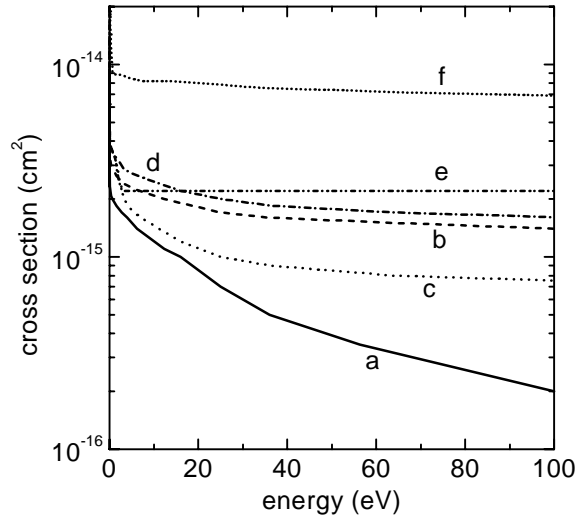


Figure 7.2. Cross sections of some ion-neutral collisions relevant to PDP and PALC discharges. a: elastic He^+ -He, b: charge transfer He^+ -He, c: elastic Ne^+ -Ne, d: charge transfer Ne^+ -Ne, e: elastic Xe^+ -Ne, f: charge transfer Xe^+ -Xe. The data are taken from Refs. [Mcd64] and [Sak91]. A constant value derived from mobility data [Eli84] is assumed for cross section e, except at low energy, where it is assumed to be the same as c. The energy on the horizontal axis is the ion impact energy.

7.3 Fast neutrals

The ion-neutral collisions lead to the formation of energetic neutral particles. The ion flux is thus accompanied by a flux of fast neutrals. In this section we estimate the importance of this fast neutral flux. We consider the case that there is only one species of gas particles and that symmetric charge transfer is the predominant collision process for ions, as before. After a charge transfer collision the neutral particle has the initial ion energy, which it loses again via elastic collisions with gas particles that are virtually at rest. The energy transferred to a gas particle in an elastic collision is [Mcd64]

$$\Delta\varepsilon = \frac{1}{2}(1 - \cos\theta)\varepsilon, \quad (7.14)$$

where ε is the initial energy of the fast neutral and θ is the scattering angle in the CM system. In case the scattering is isotropic, the probability of $\cos\theta$ is uniformly distributed between -1 and 1 . Equation (7.14) then implies that the probability of $\Delta\varepsilon$ is uniformly distributed between 0 and ε : the energy is redistributed completely randomly over the two colliding particles.

The density $N'(\varepsilon)d\varepsilon$ of the fast neutrals with an energy in between ε and $\varepsilon + d\varepsilon$ can be found by balancing the rates of their production and loss. Production of neutrals in the energy interval occurs by symmetric charge transfer and by elastic collisions of other fast neutrals with an energy larger than ε . The neutrals leave the energy interval through elastic collisions. Balancing the rates of these three processes, we write

$$N\sigma(\varepsilon)\sqrt{\frac{2\varepsilon}{m}}n_i f(\varepsilon)d\varepsilon + \int_{\varepsilon}^{\infty} \left[\frac{2d\varepsilon}{\varepsilon'} NQ(\varepsilon')\sqrt{\frac{2\varepsilon'}{m}}N'(\varepsilon') \right] d\varepsilon' = NQ(\varepsilon)\sqrt{\frac{2\varepsilon}{m}}N'(\varepsilon)d\varepsilon, \quad (7.15)$$

where n_i is the (total) ion density and Q is the cross section for elastic neutral-neutral collisions. The second term on the left – representing the elastic production rate – contains the factor $2d\varepsilon/\varepsilon'$. This is the probability that after an elastic collision between a neutral with energy $\varepsilon' > \varepsilon$ and a neutral at rest, one of the two particles ends up in the energy interval $d\varepsilon$, assuming the energy redistribution to be completely random.

The density $N'(\varepsilon)d\varepsilon$ can be found from equation (7.15) by substituting $N'(\varepsilon) = \varepsilon^{1/2}h(\varepsilon)/Q(\varepsilon)$ or $N'(\varepsilon) = \varepsilon^{-5/2}h(\varepsilon)/Q(\varepsilon)$, differentiating the entire equation with respect to ε , and solving the resulting differential equation for $h(\varepsilon)$. After back-substitution of $h(\varepsilon)$ we find that

$$N'(\varepsilon)d\varepsilon = \frac{\sigma(\varepsilon)}{Q(\varepsilon)}n_i f(\varepsilon)d\varepsilon + \frac{2}{Q(\varepsilon)}n_i \varepsilon^{-5/2} \int_{\varepsilon}^{\infty} [\sigma(\varepsilon')\varepsilon'^{3/2} f(\varepsilon')] d\varepsilon' d\varepsilon \quad (7.16)$$

The first term of this expression is the density one would find from equation (7.15) without the elastic production term: obviously it represents the neutrals that have been produced directly by charge transfer collisions. For constant cross sections σ and Q the ion energy distribution is given by (7.9), and equation (7.16) becomes

$$N'(\varepsilon)d\varepsilon = \frac{\sigma}{Q} \left(1 + \frac{2\omega}{\varepsilon} + \frac{2\omega^2}{\varepsilon^2} \right) n_i f(\varepsilon)d\varepsilon \quad (7.17)$$

where $f(\varepsilon)$ is once again given by equation (7.9).

The flux $\Gamma'(\varepsilon)d\varepsilon$ of the fast neutrals with an energy in between ε and $\varepsilon + d\varepsilon$ is the product of their density (7.17) and their average velocity. Since not all neutrals move in exactly the same direction, the average velocity is somewhat smaller than $(2\varepsilon/m)^{1/2}$. An upper limit for the flux is thus found as

$$\Gamma'(\varepsilon)d\varepsilon < \frac{\sigma}{Q} \left(1 + \frac{2\omega}{\varepsilon} + \frac{2\omega^2}{\varepsilon^2} \right) n_i \sqrt{\frac{2\varepsilon}{m}} f(\varepsilon)d\varepsilon = \frac{\sigma}{Q} \left(1 + \frac{2\omega}{\varepsilon} + \frac{2\omega^2}{\varepsilon^2} \right) \Gamma_i g(\varepsilon)d\varepsilon, \quad (7.18)$$

where Γ_i is the (total) ion flux and $g(\varepsilon)$ is given by equation (7.13). Note however that the neutrals represented by the first term of equation (7.16) *do* all move in exactly the same direction, so that a lower limit for the flux is given by

$$\Gamma'(\varepsilon)d\varepsilon > \frac{\sigma}{Q} n_i \sqrt{\frac{2\varepsilon}{m}} f(\varepsilon)d\varepsilon = \frac{\sigma}{Q} \Gamma_i g(\varepsilon)d\varepsilon. \quad (7.19)$$

Since σ is generally larger than Q this means that the fast neutral flux impinging on the surface exceeds the ion flux, for every energy.

7.4 Monte Carlo calculations

Although the above theoretical treatment gives a good feel for the ion and neutral energy distributions, it is far from complete: the influence of (isotropic) elastic ion-neutral collisions is neglected, the electric field and cross sections are assumed to be

constant, etc. A more complete picture of the energetic ions and neutrals can be obtained by Monte Carlo modeling. In this section we present the Monte Carlo calculation of the ion and fast neutral energy distributions in some typical microdischarge configurations.

The Monte Carlo model is basically the same as the model described in Chapter 6 of this thesis. It simulates the individual paths of a large number of ions and fast neutrals. The ions are sampled randomly from an ionization rate profile that has been calculated *a priori* with a fluid model, and then followed until they reach the surface. The electric field that accelerates the ions is also taken from the fluid calculation. The two-dimensional fluid model that we use for this purpose is described in Chapters 2-3 of this thesis. In addition to the ions, the neutrals with an energy higher than 1 eV are followed from all collision events occurring in the simulations. Both symmetric charge transfer collisions and isotropic elastic collisions are taken into account. The cross sections of the ion-neutral collisions are considered as functions of the impact energy, as represented in Fig. 7.2. For the cross sections of neutral-neutral collisions we assume constant values, derived from a hard-sphere model: [Hir54] $1.36 \times 10^{-15} \text{ cm}^2$ for He-He, $1.87 \times 10^{-15} \text{ cm}^2$ for Ne-Ne, $3.85 \times 10^{-15} \text{ cm}^2$ for Ne-Xe, and $6.53 \times 10^{-15} \text{ cm}^2$ for Xe-Xe.

The trajectory of an ion or fast neutral is simulated by the following procedure:

- 1) A random value is chosen for the time until the next collision, taking into account the appropriate probability distribution given by the total collision frequency. For ions we use the null collision method. [Sku68]
- 2) The free path covered during this time is calculated by integrating the equation of motion.
- 3) The type of the collision is determined randomly, taking into account the relative probability of all possible collision types.
- 4) The velocities of the colliding particles are transformed to the CM system.
- 5) The effect of the collision is simulated. In case of symmetric charge transfer, the ion and neutral velocities are simply swapped. In case of an isotropic elastic collision, the velocities are turned to random (but mutually opposite) directions.
- 6) The velocities are transformed back to the laboratory system.
- 7) In case the laboratory energy of the original target particle now exceeds 1 eV, it is considered as a fast neutral and is followed too.

The procedure 1-7 is repeated until the ion or fast neutral reaches the surface. Neutrals are not followed anymore once their energy has dropped below 1 eV. Reflection at the surface is not considered. For more details on the Monte Carlo model we refer to Chapter 6.

We applied the Monte Carlo model described above to a standard PALC discharge in pure helium. This case is relatively simple. The microdischarge operates in the DC mode, where the main ion surface bombardment occurs at the cathode. The gas pressure is 150 Torr. The only ion species of importance is He^+ . The two-dimensional profiles of the electric potential and the ionization rate – input data of the Monte Carlo simulations – are shown in Fig. 7.1. We simulated the trajectories of ten million ions and all the neutrals beyond 1 eV formed in collisions. Figure 7.3 shows the calculated energy distribution $g(\epsilon)$ of the incident ion flux, as well as the energy distribution $\Gamma'(\epsilon)/\Gamma_I$ of the incident fast neutral flux. Note that the neutral energy distribution is not normalized to unity, but scaled along with the ion energy distribution. Besides the Monte Carlo results, the theoretical distribution function (7.13) and the upper limit (7.18) are represented, where the parameter ω was found

from the calculated drift velocity by equation (7.12). The fast neutral flux in the Monte Carlo simulation turns out to be close to the upper limit (7.18).

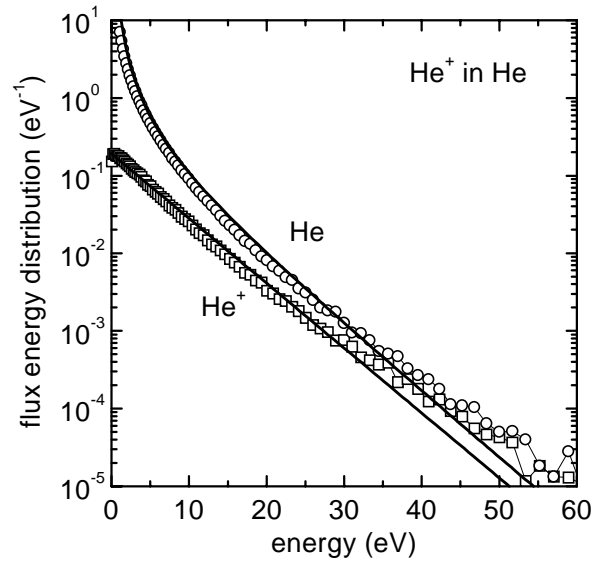


Figure 7.3. Energy distribution of the He^+ flux and the accompanying fast neutral flux impinging on the cathode in a PALC discharge in pure He. The neutral flux energy distribution is not normalized to unity but related to the ion flux as $\Gamma'(\epsilon)/\Gamma_i$. The connected symbols represent the result of a Monte Carlo calculation, the lines are the theoretical functions (7.13) and (7.18).

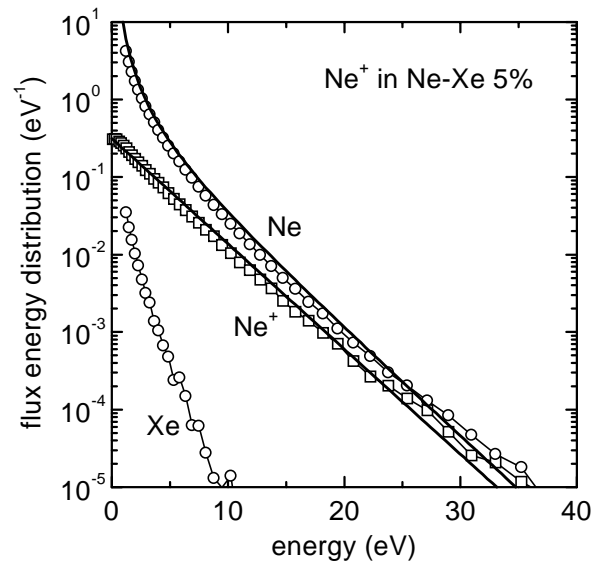


Figure 7.4. Energy distribution of the Ne^+ flux and the accompanying fast neutral fluxes impinging on the surface in a AC DPD discharge in Ne-Xe 5%, at the moment and the position where they reach their maximum value. The neutral flux energy distribution is not normalized to unity but related to the ion flux as $\Gamma'(\epsilon)/\Gamma_i$. The connected symbols represent the result of a Monte Carlo calculation, the lines are the theoretical functions (7.13) and (7.18).

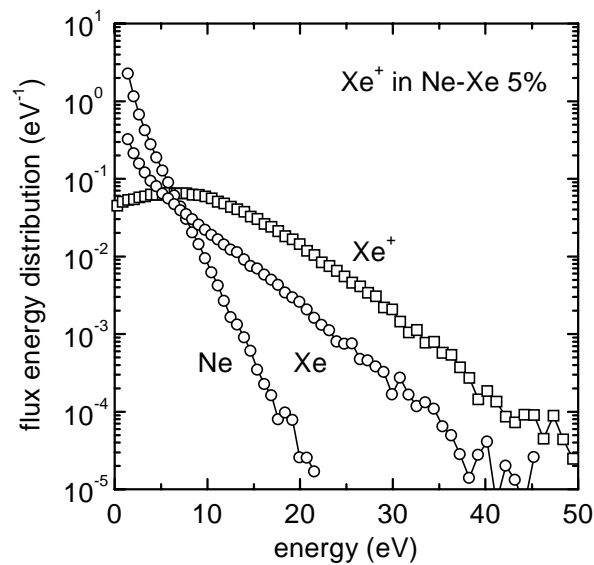


Figure 7.5. Energy distribution of the Xe^+ flux and the accompanying fast neutral fluxes impinging on the surface in a AC PDP discharge in Ne-Xe 5%, at the moment and the position where they reach their maximum value. The neutral flux energy distribution is not normalized to unity but related to the ion flux as $\Gamma^+(\varepsilon)/\Gamma_i$. These data were calculated with a Monte Carlo model.

Then we considered a typical design [Hir98] for a surface-type AC PDP in a mixture of 95% Ne and 5% Xe. This case is more complicated. In contrast to the PALC discharge, the microdischarge in the PDP design has a transient character. However, the typical lifetime of individual ions is shorter than the typical time scale for the electric field variations. The gas pressure is 450 Torr. Two ion species are important: Ne^+ and Xe^+ . Figure 7.1 shows the electric potential and Xe^+ formation rate at the moment and position of maximum ion flux. The Ne^+ formation rate is not shown here but is similar to that of Xe^+ . The calculated energy distributions are shown in Figs. 7.4 and 7.5. For Ne^+ the equations (7.13) and (7.18) are once again a good approximation of the Monte Carlo results.

For Xe^+ however the situation is entirely different. For these ions the parent gas only constitutes a small percentage of the total gas mixture, so that the Xe^+ energy distribution is determined by elastic collisions with Ne rather than by symmetric charge transfer. The equations (7.13) and (7.18-19) do hence not apply. At low energy ($\varepsilon < 10$) the Xe^+ distribution is underpopulated compared to the exponential function (7.13). In contrast to what we found for Ne^+ , the fast neutrals produced by Xe^+ are less important than the ions themselves. This is not surprising, since elastic collisions are far less efficient as to forming fast neutrals than charge transfer collisions. Figure 7.6 demonstrates that if we increase the Xe percentage, the influence of symmetric charge transfer collisions rapidly grows: the Xe^+ energies decrease and the energy distribution approaches the form (7.13). For 20% xenon, equation (7.13) already gives quite a reasonable description.

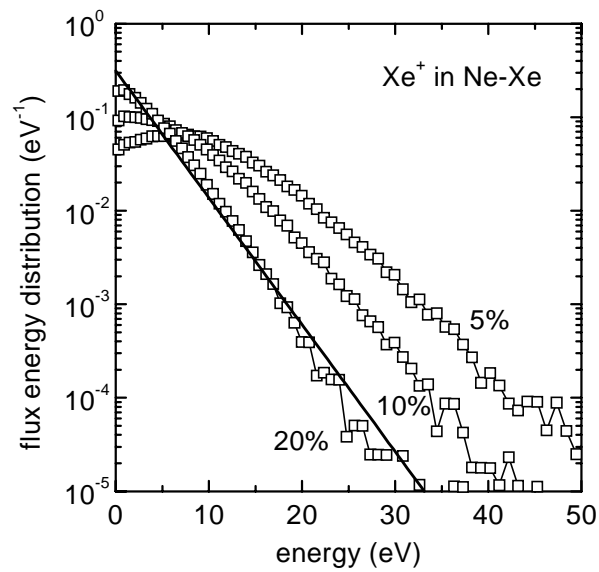


Figure 7.6. Energy distribution of the Xe^+ flux impinging on the surface in an AC PDP discharge in Ne-Xe, for different percentages of Xe. The connected squares represent the results of Monte Carlo calculations, the line gives the theoretical estimate (7.13) for 20% xenon.

7.5 Conclusions

For ions that mainly undergo charge transfer collisions, the energy distribution can be found from the drift velocity as a simple theoretical function, which is essentially different from the Maxwellian distribution function. Also the energy distribution of the fast neutrals formed in symmetric charge transfer collisions is well described by a theoretical function. The motion of both ions and fast neutrals is strongly orientated along the electric field. In general the fast neutral flux is larger than the ion flux itself. The simple functions fail to describe the energy distribution of ions that mainly undergo elastic collisions. Full Monte Carlo calculations are required in that case.

Chapter 8

Resonance radiation transport in PDP discharges*

8.1 Introduction

Fluid models are widely used to calculate the yield of UV radiation from the microdischarges in PDPs. Examples of such calculations can be found in Refs. [Meu95, Rau99a] and in Chapter 5 of this thesis. The most important UV radiation utilized in PDPs is the resonance radiation emitted by the $\text{Xe}^*(^3P_1)$ state atoms at a wavelength of 147 nm. The PDP discharge conditions are such that these resonance photons are many times absorbed and re-emitted before leaving the discharge. This phenomenon is known as imprisonment or trapping of resonance radiation. The most obvious effect of the radiation trapping is that the photons emerge from the discharge on a time scale that is much longer than the natural lifetime of the resonant state. Another effect is that the density of the resonant state atoms is enormously increased. This affects the entire kinetics of the excited species in the discharge, because the rates of several important reactions – including collisional quenching of the resonant state and the formation of dimers – depend on the density of the resonant state atoms. For illustration, Table 8.1 gives an overview of the most important reactions involving $\text{Xe}^*(^3P_1)$ in PDP discharges in neon-xenon; the time dependent rates of some of these reactions are shown in Fig. 8.1. To properly predict the production of UV radiation in PDP discharges, fluid models have to account for the effects of radiation trapping.

Table 8.1. The most important reactions involving $\text{Xe}^*(^3P_1)$, in typical PDP discharges in neon-xenon. The numbering of the reactions is taken from Table 2.2.

#	Reaction
	production
R22	$e + \text{Xe} \rightarrow e + \text{Xe}^*(^3P_1)$
R72	$\text{Xe}^{**} + \text{Ne} \rightarrow \text{Xe}^*(^3P_1) + \text{Ne}$
R74	$\text{Xe}^{**} + \text{Xe} \rightarrow \text{Xe}^*(^3P_1) + \text{Xe}$
R83	$\text{Xe}^{**} \rightarrow \text{Xe}^*(^3P_1) + h\nu (800 \text{ nm})$
	loss
R26	$e + \text{Xe}^*(^3P_1) \rightarrow e + \text{Xe}^{**}$
R69	$\text{Xe}^*(^3P_1) + \text{Ne} \rightarrow \text{Xe}^*(^3P_2) + \text{Ne}$
R77	$\text{Xe}^*(^3P_1) + \text{Xe} + \text{Ne} \rightarrow \text{Xe}_2^*(O_u^+) + \text{Ne}$
R78	$\text{Xe}^*(^3P_1) + 2\text{Xe} \rightarrow \text{Xe}_2^*(O_u^+) + \text{Xe}$
R81	$\text{Xe}^*(^3P_1) \rightarrow \text{Xe} + h\nu (147 \text{ nm})$

* This chapter, in slightly altered form, will be published in: G. J. M. Hagelaar, M. H. Klein, R. J. M. M. Snijkers, and G. M. W. Kroesen, "Resonance radiation transport in plasma display panels," J. Appl. Phys..

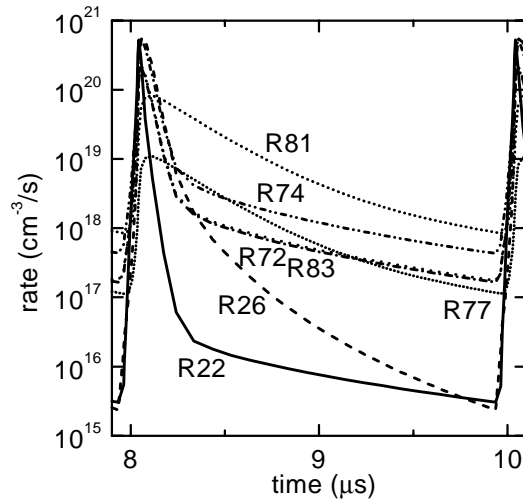


Figure 8.1. Time evolution of the space averaged reaction rates of the most important processes involving the $\text{Xe}^*(^3P_1)$ state, in a fluid simulation of a typical PDP discharge in neon-xenon (5%). The curves are tagged with the numbers of the corresponding reactions in Tab. 8.1. The time interval from 8 to 10 μs corresponds to one sustain pulse.

The exact calculation of the density of the resonant state atoms under the influence of radiation trapping requires the solution of an integro-differential equation, such as Holstein's equation [Hol51]. However, solving such equation in time dependent fluid models is practically infeasible. Most fluid models [Meu95, Mcg98, Rau99] describe the resonant state by an ordinary differential equation – a rate equation or a continuity equation – where they characterize the radiative decay by an effective lifetime

$$\tau_{\text{eff}} = g\tau_0, \quad (8.1)$$

rather than the natural lifetime τ_0 . Here g is a trapping factor, which represents the average number of absorption-re-emission events that a resonance photon undergoes before escaping from the discharge. (Some authors use g^{-1} to indicate what we call g .) The trapping factor is usually derived from a known solution of Holstein's equation for some symmetric geometry. Standard expressions for trapping factors under various assumptions can be found in Refs. [Mol92, Mol93]. The trapping factor approach (8.1) simulates – in a computationally very attractive way – the major effects of radiation trapping: it slows down the release of resonance photons and increases the density of the resonant state atoms. It does, however, not describe the spatial evolution of the resonant state density.

An alternative and more accurate way to describe the radiation trapping is by a Monte Carlo model for resonance photons. Besides the density of the resonant state atoms, a photon Monte Carlo model predicts the spectral lineshape of the resonance radiation escaping from the discharge. This offers the possibility of direct experimental validation of the model. In this chapter we present such a Monte Carlo model of the resonance photons in PDPs. The photon Monte Carlo model requires the input of the rates of collision processes that lead to the formation of the resonant state. For this purpose we use the results of the fluid model presented in Chapters 2-3 of this thesis. For reasons of simplicity, the Monte Carlo model is not self-consistently coupled to the fluid model; it just uses reaction rates that have been calculated *a priori* with the fluid model. This approach is legitimate because the rates concerned are only weakly

coupled to the radiation trapping problem. In the fluid model, the radiation trapping is accounted for with the trapping factor approach (8.1).

In this chapter, we do the following: After describing the Monte Carlo model in Section 8.2, we compare, in Section 8.3, the calculated resonant state atom density profile with the density profile resulting from the trapping factor approach in the fluid model. Then, in Section 8.4, we compare the calculated emission spectrum with experimental data. The conclusions are given in Section 8.5. All calculations presented are based on the two-dimensional model geometry shown in Fig. 8.2, which represents a cross section through one row of a coplanar-electrode PDP. The considered discharge conditions are also indicated in Fig. 8.2: the discharge gas is a mixture of neon and a small percentage of xenon, at a pressure of 450 Torr, and the square wave voltage applied to the sustain electrodes has an amplitude of 260 V and frequency of 250 kHz.

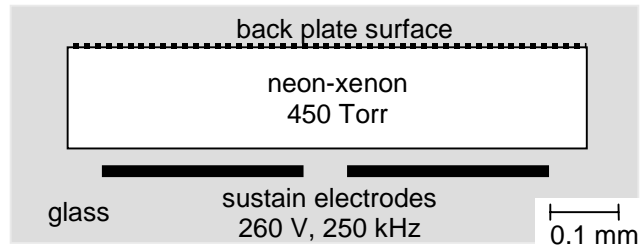


Figure 8.2. Two-dimensional model geometry considered in the calculations, representing one discharge cell of a coplanar-electrode type PDP. The surface on the top corresponds to the back plate of the display, where the phosphors are located.

8.2 The photon Monte Carlo model

In the Monte Carlo model, a large number of resonant state excitation events is sampled from the total excitation rate profile calculated with the fluid model. The resonance photons that result from these excitation events, are followed – one by one – until they escape from the discharge. Since the escape time of the photons is much longer than the typical time scale for changes in the excitation rate, the Monte Carlo model is not suitable to study the time dependence of the radiation transport. We can, however, still calculate the time averaged photon transport. Below we describe how a photon path is simulated.

We start from the time averaged effective excitation rate profile, shown in Fig. 8.3. It is the sum of the rates of the reactions R22, R72, R74, and R83, diminished with the rate of reaction R26. An excitation event is randomly sampled from this profile. A random lifetime τ of the resulting resonant state is determined, according to

$$\tau = -\frac{1}{\nu} \ln(1 - r_1), \quad (8.2)$$

where r_1 is a random number, uniformly distributed between 0 and 1, as generated with a random number computer routine, and ν is given by

$$\nu = \frac{1}{\tau_0} + \nu_c. \quad (8.3)$$

Here $\tau_0 = 3.46$ ns is the natural lifetime of $\text{Xe}^*(^3P_1)$ [Ber79] and ν_c is the total frequency of the collision processes R69, R77, R78, and R81. Note that ν_c is constant in time. The time dependent frequency of electron induced quenching R26 is not included in ν_c ; this reaction is taken into account in the effective excitation rate profile. (Fig. 8.1) This crude treatment of the electron induced quenching is somewhat justified by the fact that this process, like the excitation, takes place only during a short fraction of the time, as can be seen in Fig. 8.1. Another random number r_2 is used to determine whether a photon is emitted or the resonant state is lost in a collision process: if $r_2 > \tau\nu_c$ the photon is emitted, otherwise the resonant state is lost.

In the event that a photon is emitted, a random photon frequency is chosen. We assume that the frequency distribution is mainly determined by the broadening of the $\text{Xe}^*(^3P_1)$ level due to collisions between the gas atoms, and is given by the Lorentz profile

$$L(\omega) = \frac{\Delta\omega_p/(2\pi)}{(\omega - \omega_0)^2 + \Delta\omega_p^2/4}, \quad (8.4)$$

where ω is the angular frequency, ω_0 is the central angular frequency (1.28×10^{16} Hz), and $\Delta\omega_p$ is the full width at half maximum. For the width of the profile we use the experimental data from Ref. [Iga98]:

$$\Delta\omega_p = 2.55 \times 10^{-14} n_{\text{Xe}} + 1.00 \times 10^{-15} n_{\text{Ne}}, \quad (8.5)$$

where n_{Xe} and n_{Ne} are the xenon and neon density in m^{-3} . The influence of the Doppler effect on the frequency distribution is neglected compared to the collisional broadening (8.4), which seems a good approximation for partial xenon pressures beyond 10 Torr. A random angular frequency ω is chosen from the distribution (8.4) as

$$\omega = \omega_0 + \frac{\Delta\omega_p}{2} \tan\left(\frac{\pi}{2}(2r_3 - 1)\right), \quad (8.6)$$

where r_3 is a random number.

Given the photon frequency, the absorption coefficient is calculated from

$$\kappa(\omega) = \frac{\lambda_0^2 g_2}{4\tau_0 g_1} n_{\text{Xe}} L(\omega), \quad (8.7)$$

where $L(\omega)$ is once again the Lorentz profile (8.4), $\lambda_0 = 147$ nm is the central wavelength, and $g_1 = 1$ and $g_2 = 3$ are the statistical weights of the ground and resonant states, respectively. A random value for the traveled distance until absorption is found as

$$\lambda = -\frac{1}{\kappa} \ln(1 - r_4), \quad (8.8)$$

in analogy to equation (8.2). Using two additional random numbers r_5 and r_6 , a random direction is determined for the photon emission, after which the position of the absorption is calculated. The lifetime of the resulting resonant state is again determined from equation (8.2), and so on. The procedure is repeated until the photon reaches the wall or the resonant state is lost in a collision. Note that, each time the photon is re-emitted, we assume that its frequency is independent of the frequency before the absorption. This condition is known as complete frequency redistribution.

For the storage of Monte Carlo simulation results, the geometry is divided in small two-dimensional cells. We make use of the numerical grid of the fluid model. In each grid cell we record the cumulative lifetime of the resonant state. From this, the

resonant state atom density can be directly derived. In a similar way, the photon frequency distribution is determined in every cell, by recording the cumulative time of photon presence separately for a large number of frequency intervals.



Figure 8.3. Time averaged profile of the effective excitation rate of $\text{Xe}^* (^3P_1)$, as calculated with the fluid model. The discharge geometry and conditions are shown in Fig. 8.2; the xenon percentage is 5%. The averaging was done over one address pulse and five sustain pulses. The increment of the contours is $9.2 \times 10^{18} \text{ cm}^{-3}$.

8.3 Comparison with the trapping factor approach

We simulated the paths of 10^7 photons, initially emitted according to the effective excitation rate profile of Fig. 8.3. The gas pressure is 450 Torr, the xenon percentage 5%. Fig. 8.4(a) shows the calculated spatial density profile of the resonant state atoms. For comparison, Fig. 8.4(b) shows the resonant state density as it results from the trapping factor approach in the fluid model. According to the Monte Carlo model, the resonant state atoms are much more distributed over space than they are in the fluid model. This result is not surprising: With the trapping factor approach, the created resonant states are not spatially redistributed, so that their density profile directly reflects the effective excitation profile of Fig. 8.3. The spatial integral of the density – the total number of resonant state atoms per cm of row length – is approximately the same for both models: in the Monte Carlo model it is $4.9 \times 10^9 \text{ cm}^{-1}$, compared to $5.1 \times 10^9 \text{ cm}^{-1}$ for the fluid model.

One has to keep in mind that the density in the fluid model depends directly on the choice for the trapping factor g . Typically, g is estimated from the solution of Holstein's equation for a plane-parallel slab geometry [Hol51, Mol92]:

$$g = \frac{1}{1.146} \sqrt{\pi \kappa_0 d}, \quad (8.9)$$

where κ_0 is the absorption coefficient for the central frequency and d is the thickness of the slab. Equation (8.9) is based on the same assumptions as the ones we make in the Monte Carlo model, and the additional assumption that $\kappa_0 d \gg 1$. On substituting $d = 1.50 \times 10^{-4} \text{ m}$, the height of the model geometry, and $\kappa_0 = 6.70 \times 10^7 \text{ m}^{-1}$, calculated from the equations (8.4,5,7), we find $g = 155$. It is interesting to compare this trapping factor to the escape time of the photons in the Monte Carlo model. To obtain a proper comparison, we set the collisional loss frequency of the resonant state to zero, and simulated again 10^7 photon paths. Fig. 8.5 shows for each position in the model geometry the average escape time of photons initially emitted from that position. As can already be expected from equation (8.9), the escape time changes only weakly over space. The average escape time of the photons initially emitted according to the excitation rate profile of Fig. 8.3 turns out to be $150 \tau_0$, in good agreement of with the trapping factor $g = 155$.

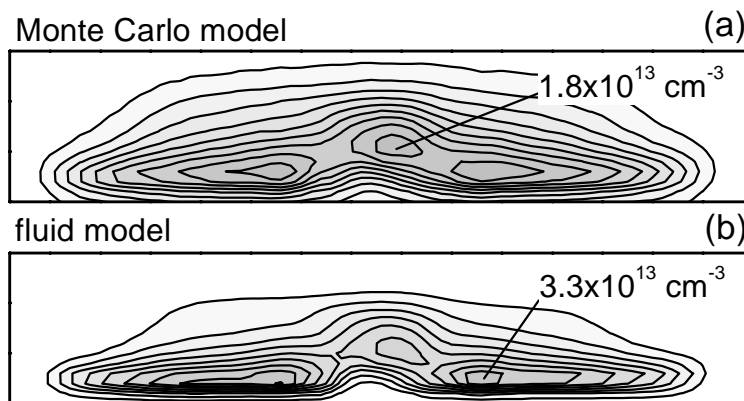


Figure 8.4. Calculated spatial profile of the resonant state atom density, for (a) the Monte Carlo model, and (b) the fluid model using a trapping factor of $g = 155$. The discharge geometry and conditions are shown in Fig. 8.2; the xenon percentage is 5%. The increment of the contours is 1/10 times the maximum value.

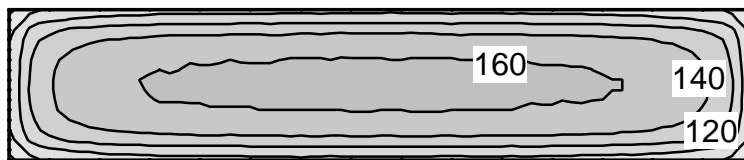


Figure 8.5. Spatial profile of the average escape time, for the geometry of Fig. 8.2; the xenon percentage is 5%. The indicated values are expressed in units of $\tau_0 = 3.46$ ns. The increment of the contours is $20\tau_0$.

8.4 Comparison with experimental results

Due to the radiation trapping, the spectral lineshape of the resonance radiation that leaves the discharge is very different from the emitted Lorentz profile (8.4). This can be seen as follows: Every time a photon is absorbed, it has a small probability to be re-emitted in the wings of the Lorentz distribution, where it has a good chance of escaping from the discharge without being absorbed again. Accordingly, the frequency distribution of the escaping photons has stronger wings than the Lorentz profile, and consequently a weaker center. Under PDP conditions, the lineshape becomes broader by orders of magnitude, and even displays a minimum at the central frequency. Fig. 8.6(a) shows the spectrum of the resonance photons that leave the discharge at the back plate, as it is calculated with the Monte Carlo model, for different cell heights; these results are obtained by integration over the back plate surface indicated in Fig. 8.3. Note that here the actual width of the Lorentz profile is no more than 3.7×10^{-3} nm.

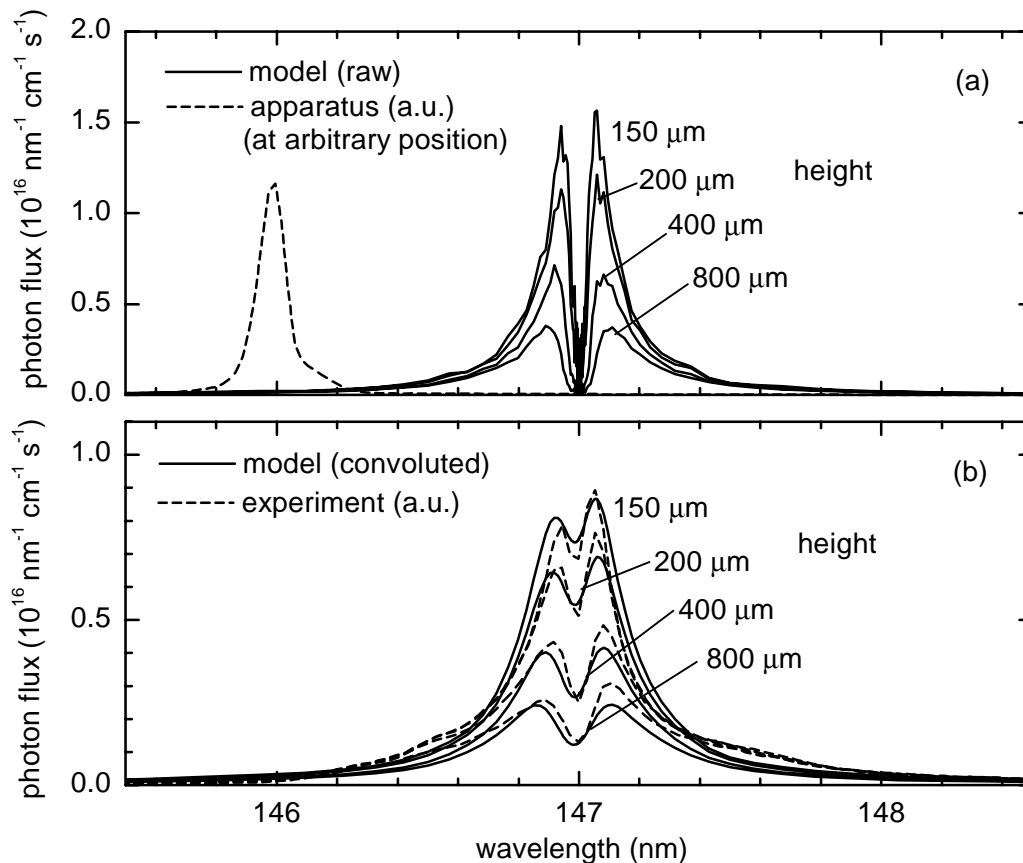


Figure 8.6. Spectrum of the resonance photons leaving the discharge at the back plate, for different cell heights. Each time the geometry and conditions are similar to the model geometry and conditions shown in Fig. 8.2; the xenon percentage 10%. Plot (a) shows the results of the Monte Carlo model, as well as the experimental apparatus profile. Plot (b) compares the convoluted modeling results with the experimental results.

In order to check the validity of the model, we measured the emitted spectrum. The measurement setup is similar to the one used in Ref. [Jeo99]. The photons enter a vacuum UV monochromator (Acton Research VM 504) through an MgF_2 observation window, placed at the position of the back plate. The spectral information is read out via an intensified charge coupled device camera (Princeton Instruments, IVUV 576x384 E) and is spectrally corrected. The experimental discharge geometry is very similar to the model geometry of Fig. 8.3; the most important difference is that the experimental geometry has additional side walls, which confine the discharge in the direction of the sustain electrodes and represent the barrier ribs of a real display.

In order to be able to directly compare the calculated spectrum with the measurements, we convolute it with the experimental apparatus profile. This profile, which we assume to be identical to the measured profile of the 436 nm mercury line, is shown in Fig. 8.6(a). The convoluted calculated spectrum is compared with the measured spectrum in Fig. 8.6(b) for different cell heights, and in Fig. 8.7 for different percentages of xenon. The overall agreement is very good: The width of the lineshape, the width of the central dip, and even the relative intensities for the different conditions are well predicted by the model. However, there are some differences: After convolution, the central dip in the calculated spectrum is less pronounced than the dip in the experimental spectrum. This suggests that the assumed apparatus profile is slightly wider than the actual apparatus profile. In addition, the wings of the measured

lineshape are sometimes stronger than they are in the calculation, especially at higher xenon pressures. For 20% xenon, the measured spectrum is also strongly asymmetric, as can be seen in Fig. 8.7(b). These effects could well be caused by the molecular radiation emitted by higher vibrational levels of $\text{Xe}_2^*(O_u^+)$.

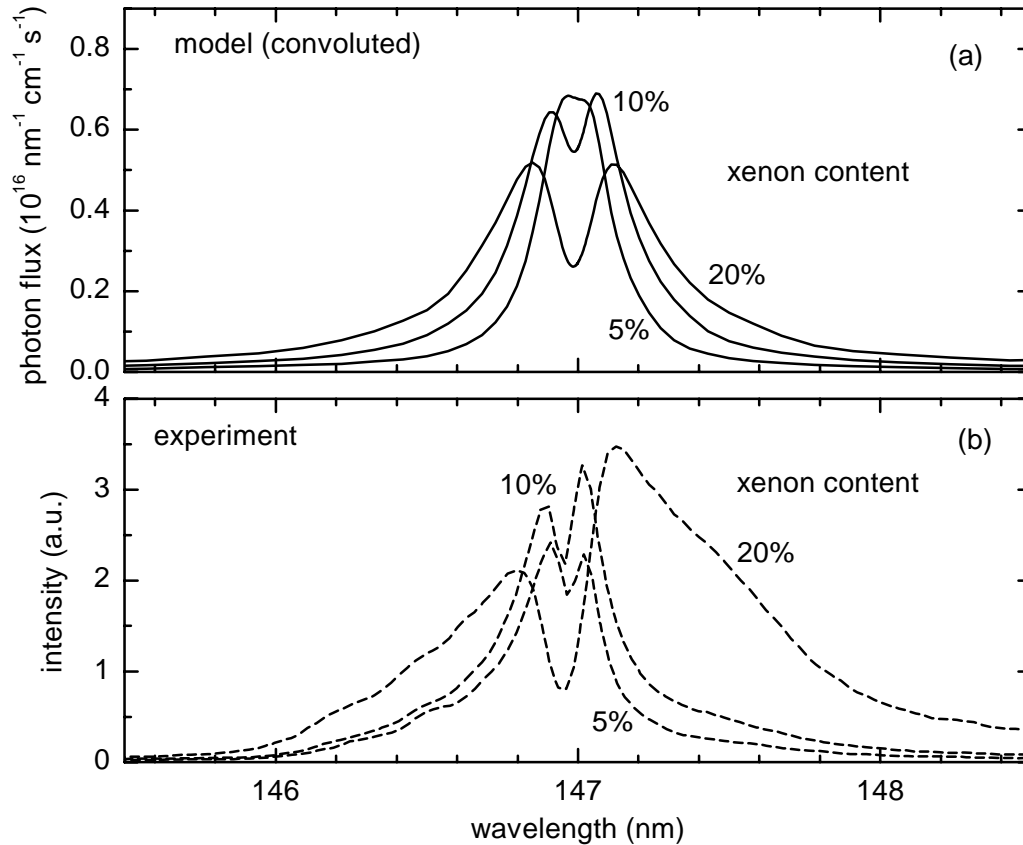


Figure 8.7. Spectrum of the resonance photons leaving the discharge at the back plate, for different percentages of xenon. Each time the geometry and conditions are similar to the model geometry and conditions shown in Fig. 8.2; the cell height is 150 μm . The figure compares (a) the results of the Monte Carlo model, after convolution with the experimental apparatus profile, with (b) the measured spectra.

8.5 Conclusions

We have presented a Monte Carlo model for the transport of resonance radiation in PDPs. First, we have compared the results of this Monte Carlo model with the results of the commonly used trapping factor approach. Although the trapping factor approach does not yield the same spatial distribution for the density of the resonant state atoms, the spatially integrated density is in good agreement with the results of the Monte Carlo model. Next, we have compared the results of the Monte Carlo model with measured spectra of the resonance radiation. The agreement is very good. The minor differences between model and experiment can be easily attributed to experimental artifacts and do not give rise to doubts about the assumptions of the model.

The overall conclusion is that, via the Monte Carlo model, we have provided experimental support for the widely used trapping factor approach.

Chapter 9

Conclusions

We have developed a two-dimensional (2D) self-consistent fluid model of the microdischarges in PALC and PDP displays. This model is based on continuity and drift-diffusion equations for plasma particle species, an electron energy equation, and Poisson's equation, all coupled together; it gives the space and time variations of the particle densities, particle fluxes, electron mean energy, reaction rates, electric field. The model is implemented as a computer code in such a way that arbitrary 2D discharge geometries, driving schemes, and reaction schemes can be taken into account. We have put together the required reaction schemes and data bases for PALC discharges in helium-hydrogen mixtures and for PDP discharges in neon-xenon. The fluid model is capable of simulating the full operation of PALC and PDP discharges, although the three-dimensional features of the PDP geometry are not represented. The simulation of a single PALC or PDP discharge takes 1-10 minutes of computation time on a modern PC.

In order to test the reliability of the fluid model, we have compared the modeling results with experimental results wherever possible. We have found the following:

- Calculated decay times of PALC discharges are in excellent quantitative agreement with measured decay times.
- For PDP discharges, the calculated ratio of the energy of the emitted resonance photons and the total energy of the emitted UV photons is in excellent quantitative agreement with experimental results.
- Calculated current-voltage characteristics and power consumptions are only of qualitative value, because these results are very sensitive to some delicate input parameters, as such secondary emission coefficients. However, calculated trends in the current-voltage characteristics of PALC discharges and in the UV generation efficiency of PDP discharges turn out to be in good agreement with measured trends.
- The model reproduces experimentally observed non-uniformities in the charging of the microsheet in PALC displays.

For all of these cases, the model does not only reproduce the experimental results, but also helps to understand them. For example, the model demonstrates that the non-uniformities in the charging of the microsheet in PALC displays result from electrical cross-talk between adjacent channels.

The basic principles of the fluid model are similar or identical to those of the fluid models developed by other authors. However, the fluid model in this thesis has several special features:

- The boundary conditions used for particle transport are different from the boundary conditions used by other authors. We have shown that the usual boundary conditions are inconsistent with classical diffusion theory, and lead to an unrealistic diffusion flux of emitted secondary electrons back to the wall. In the alternative boundary conditions we use, these problems have been solved.

- The numerical method is simple and yet extremely efficient. To avoid strong restrictions on the numerical time step, we use a (known) semi-implicit technique for the self-consistent calculation of the electric field. In addition to this technique, we have developed a new implicit technique for the evaluation of the electron energy source term. This makes it possible to include the electron energy equation in the fluid model, without significant consequences for the computation speed.
- For the simulation of the afterglow in pure helium, the electrons created by metastable-metastable ionization are described by separate transport equations, with the transport coefficients based on a Dirac function for the electron energy distribution function (EEDF). This unusual approach is necessary to account for the highly non-equilibrium nature of these electrons, and is supported by Monte Carlo simulations.

The results of the fluid model can be used as a basis for non-self-consistent particle (Monte Carlo) models, which provide detailed information that is not given by the fluid model itself. We have developed three of such Monte Carlo models, describing electrons, ions, and resonance photons, respectively. These Monte Carlo models are implemented as independent models, using results of the fluid model as input data, but not self-consistently coupled to the fluid model. The results of the Monte Carlo models are therefore invalid if they seriously contradict any fluid model assumption that is crucial to obtaining the Monte Carlo input data. Fortunately, this is not the case for any of the Monte Carlo studies presented in this thesis.

We have used the electron Monte Carlo model to obtain more insight in the validity of the fluid approach for the simulation of PALC discharges, with helium as a discharge gas. The EEDF calculated with the Monte Carlo model displays several non-equilibrium phenomena, such as peaks of fast electrons that have undergone none or only a few collisions, and the absence of a high energy tail. Although these features are not incorporated in the fluid model, both models lead to virtually the same electron density. However, the ionization rate obtained with the Monte Carlo model is spread out over a larger region than the ionization rate in the fluid model. The Monte Carlo calculations reveal that the electrons in the afterglow have a highly non-equilibrium nature, and require a special treatment in the fluid model.

The ion Monte Carlo model predicts the energy distribution functions of the ions and fast neutrals impinging on the surfaces surrounding the microdischarges; this information is essential for understanding and predicting corrosion of the surface materials. In most cases, the Monte Carlo results can be reproduced with an elementary theoretical approach, which makes it possible to predict the ion and fast neutral energy distribution functions directly from the ion drift velocity.

The photon Monte Carlo model gives an accurate description of the transport of the resonance radiation in PDP discharges, predicting the density of the resonant state atoms as well as the emitted spectrum. In the fluid model itself the radiation transport is only crudely described, using a radiation trapping factor. By carefully comparing the results of the photon Monte Carlo model with both the assumptions of the fluid model, and the measured emission spectrum, we have been able to obtain experimental support for the trapping factor approach used in the fluid model.

In short, the fluid model is supported by experimental data as well as Monte Carlo calculations and uncovers the main physical mechanisms underlying the behavior of the microdischarges.

References

- [Bac81] M. Bacal, A. M. Brunetau, W. G. Graham, G. W. Hamilton, and M. Nachman, "Pressure and electron temperature dependence of H⁺ density in a hydrogen plasma," *J. Appl. Phys.* **52** (3), 1247-1254 (1981).
- [Bar70] J. N. Bardsley and M. A. Biondi, *Adv. At. and Mol. Phys.* **6**, 1-57 (1970).
- [Bar87] M.S. Barnes, T.J. Colter, and M.E. Elta, "Large-signal time-domain modeling of low-pressure rf glow discharges," *J. Appl. Phys.* **61** (1), 81-89 (1987).
- [Ber79] J. Berkowitz, "Photoabsorption, photoionization, and photoelectron spectroscopy," (Academic Press, London, 1979).
- [Bir91] C. K. Birdsall and A. B. Langdon, "Plasma physics via computer simulation," (IOP publishing Ltd., 1991).
- [Bla08] A. Blanc, *J. Phys.* **7**, 825 (1908).
- [Boe87] J.-P. Boeuf, "Numerical model of rf glow discharges", *Phys. Rev. A* **36** (6), 2782 (1987).
- [Boe95] J.-P. Boeuf and L. C. Pitchford, "Two-dimensional model of a capacitively coupled rf discharge and comparisons with experiments in the Gaseous Electronics reference reactor," *Phys. Ref. E* **51** (2), 1376-1390 (1995).
- [Boe95a] J.-P. Boeuf and L.C. Pitchford, SIGLO-RF (Kinema Research, Monument, CO, 1995).
- [Bol96] BOLSIG, "Boltzmann solver for the SIGLO-series 1.0," CPA Toulouse & Kinema Software (1996).
- [Brau85] C. A. Brau, "Rare gas halogen excimers," in "Excimer lasers," *Topics in Applied Physics* **30**, 87-138 (Springer-Verlag, New York, 1984).
- [Bro67] S. C. Brown, "Basic data of plasma physics," 2nd edition (MIT Press, London, 1967).
- [Buz90] T. Buzak, "A new active-matrix technique using plasma addressing," *Digest of Technical Papers 1990 SID International Symposium*, 420-423 (Society for Information Display, 1990).
- [Buz93] T. Buzak, P. Green, S. Guthrie, S. Hartley, K. Hillen, G. Lamer, P. Martin, D. Nishida, T. O'Neal, W. Stein, K. Stinger, and M. Wagner, "A 16-inch full-color plasma addressed active-matrix LCD," *Digest of Technical Papers, 1993 SID International Symposium*, 883-886 (Society for Information Display, 1993).
- [Cam95] R. B. Campbell, R. Veerasingham, and R. T. McGrath, "A two-dimensional multispecies fluid model of the plasma in an ac plasma display panel," *IEEE Trans. Plasma Sci.* 698-708 (1995).
- [Cha87] P. J. Chantry, "A simple formula for diffusion calculations involving wall reflection and low density," *J. Appl. Phys.* **62** (4), 1141-1148 (1987).
- [Cho95] K. C. Choi and K.-W. Whang, "Numerical analysis of the analysis in a dc plasma display panel by 2-dimensional multifluid equations," *IEEE Trans. Plasma Sci.* **23** (3), 399-404 (1995).
- [Col78] C. B. Collins and F. W. Lee, "Measurement of the rate coefficients for the bimolecular and termolecular ion-molecule reactions of He₂⁺ with

- selected atomic and molecular species,” *J. Chem. Phys.* **68**, 1391 (1978).
- [Dem88] A. V. Dem’yanov, N. A. Dyatko, I. V. Kochetov, A. P. Napartovich, A. F. Pal’, V. V. Pichugin, and A. N. Starostin, “Characteristics of non-self-maintained discharges in H₂-He mixtures,” *Sov. Phys. Tech. Phys.* **33** (1), 43-46 (1988).
- [Eck88] D. J. Eckstrom, H. H. Nakano, D. C. Lorents, T. Rothem, J. A. Betts, M. E. Lainhart, D. A. Dakin, and J. E. Maenchen, “Characteristics of electron-beam-excited Xe₂ at low pressures as a vacuum ultraviolet source,” *J. Appl. Phys.* **64** (4), 1679-1690 (1988).
- [Ell76] H. W. Ellis, R. Y. Pai, E. W. McDaniel, E. A. Mason, and L. A. Viehland, “Transport properties of gaseous ions over a wide energy range,” *Atomic Data and Nuclear Data Tables* **17** (3), 177-210 (1976).
- [Ell84] H. W. Ellis, M. G. Thackston, E. W. McDaniel, and E. A. Mason, “Transport properties of gaseous ions over a wide energy range,” *Atomic Data and Nuclear Data Tables* **31**, 113-156 (1984).
- [Fel68] P. V. Feltsan and I. P. Zapesochny, *Ukr. Fiz. Zh.* **13**, 205 (1968).
- [Gar98] J.-P. Gardou, “Imprisonment of resonance radiation in gases,” Ph.D. thesis (Université Paul Sabatier, Toulouse, France, 1998).
- [Gog92] E. Gogolides and H. H. Sawin, “Continuum modeling of radio-frequency glow discharges. I. Theory and results for electropositive and electronegative gases,” *J. Appl. Phys.* **72** (9), 3971-3987 (1992).
- [Gri97] I. S. Grigoriev, E. Z. Meilikhov, and A. A. Radzig, “Handbook of physical quantities,” CRC Press, London (1997).
- [Gro73] T. R. Grossheim and J. J. Leventhal, “Production of He⁺ in He₂⁺-He collisions near threshold,” *Phys. Rev. A* **7** (5), 1591-1594 (1973).
- [Hag99] G. J. M. Hagelaar and G. M. W. Kroesen, “Implementing arbitrarily shaped boundaries in two-dimensional discharge modeling,” *IEEE Trans. Plasma Sci.* **27** (6), 1606-1609 (1999).
- [Has99] K. Hassouni, T. A. Grotjohn, and A. Gicquel, “Self-consistent microwave field and plasma discharge simulations for a moderate pressure hydrogen discharge reactor,” *J. Appl. Phys.* **86** (1), 134-151 (1999).
- [Hir54] J. O. Hirschfelder, C. F. Curtiss, and R. B. Bird, “Molecular theory of gases and liquids,” John Wiley & Sons, Inc. (1954).
- [Hir98] H. Hirakawa et al., “Cell structure and driving method of a 25-in. (64-cm) diagonal high-resolution color AC plasma display,” *SID digest*, 279-282 (1998).
- [His91] J. R. Hiskes, “Cross sections for the vibrational excitation of the H₂ X ¹Σ_g⁺(v) levels generated by electron collisional excitation of the higher singlet states,” *J. Appl. Phys.* **70** (7), 3409-3417 (1991).
- [Hok84] H. Hokazono, K. Midorikawa, M. Obara, and T. Fujioka, “Theoretical analysis of a self-sustained discharge pumped XeCl laser,” *J. Appl. Phys.* **56** (3), 680-690 (1984).
- [Hol51] T. Holstein, “Imprisonment of resonance radiation in gases, II,” *Phys. Rev.* **83** (6), 1159 (1951).
- [Hym79] H. A. Hyman, *Phys. Rev. A* **20**, 855-859 (1979).
- [Hym81] H. A. Hyman, *Phys. Rev. A* **24**, 1094-1095 (1981).
- [Iga95] K. Igarashi, S. Mikoshiba, Y. Watanabe, M. Suzuki, and S. Murayama, “Characterization of imprisoned Xe resonant photons in He-Xe and Ne-Xe mixtures,” *J. Phys. D* **28**, 1377-1383 (1985).

- [Ilc97] K. J. Ilcisin, T. S. Buzak, and G. J. Parker, "The switching dynamics of the plasma addressed liquid crystal display," proceedings of the XXIIIrd International Conference on Phenomena in Ionized Gases, volume IV: invited papers, C4-225 (Toulouse, 1997).
- [Iva99] V. V. Ivanov, Yu. A. Mankelevich, O. V. Proshina, A. T. Rakhimov, and T. V. Rakhimova, "Modeling of a repetitive discharge in the cell of a plasma display panel," *Plasma Physics Reports* **25** (7), 591-598 (1999).
- [Jan87] R. K. Janev, W. D. Langer, K. Evans, Jr., and D. E. Post, Jr., "Elementary processes in hydrogen-helium plasmas," Springer-Verlag, Berlin (1987).
- [Jeo99] H. Jeong, J. Seo, C. Yoon, J. Kim, and K.-W. Whang, "Characteristics of vacuum ultraviolet emission from a surface discharge type alternating current plasma display panel cell," *J. Appl. Phys.* **85**, 3092-3096 (1999).
- [Joh80] R. Johnson, A. Chen, and M. A. Biondi, "Three-body association reactions of He^+ , Ne^+ , and Ar^+ ions in their parent gases from 78 to 300 K," *J. Chem. Phys.* **73**, 1717-1720 (1980).
- [Kak95] T. Kakizaki, S. Tanamachi, M. Hayashi, "Development of 25-inch active-matrix LCD using plasma addressing for video rate high quality displays," Digest of Technical Papers, 1995 SID International Symposium, 915-918 (Society for Information Display, 1995).
- [Kle97] M. Klein and R. Snijkers, "Principles of VUV radiation trapping in PDPs," PFL – Aachen report 1398/99 (1997).
- [Kle99] M. Klein, private communications (Philips Research Laboratories Aachen, Germany, 1999).
- [Lap95] G. Lapenta, F. Iinoya, and J.U. Brackbill, "Particle-in-cell simulation of glow discharges in complex geometries," *IEEE Trans. Plasma Sci.* **23** (4), 769 (1995).
- [Lev81] L. A. Levin, *IEEE J. Quant. Electr.* **17**, 2282 (1985).
- [LTI] Estimate from LTI, University of Karlsruhe, Germany.
- [Mai75] W. B. Maier II, "Reactions of diatomic rare-gas ions with rare-gas atoms for primary-ion energies below 50 eV," *J. Chem. Phys.* **62** (12), 4615-4622 (1975).
- [Mar89] D. W. Martin, C. Weiser, R. F. Sperlein, D. L. Bernfeld, and P. E. Siska, "Collision energy dependence of product branching in Penning ionization: $\text{He}(2^1\text{S}, 2^3\text{S}) + \text{H}_2, \text{D}_2, \text{and HD}$," *J. Chem. Phys.* **90** (3), 1564-1576 (1989).
- [Mas69] H. S. W. Massey and E. H. S. Burhop, "Electronic and ionic impact phenomena," second edition, Oxford University Press, London (1969).
- [Mat84] N. Matsunami, Y. Yamamura, Y. Itikawa, N. Itoh, Y. Kazumata, S. Miyagawa, K. Morita, R. Shimizu, and H. Tawara, "Energy dependence of the ion-induced sputtering yields of monatomic solids," *Atomic Data and Nuclear Data Tables* **31** (1), 1-80 (1984).
- [Mcd64] E. W. McDaniel, "Collision phenomena in ionized gases," John Wiley & Sons, Inc., New York London Sydney (1964).
- [Mcf73] M. McFarland, D. L. Albritton, F. C. Fehsenfeld, E. E. Ferguson, and A. L. Schmeltekopf, "Flow-drift technique for ion mobility and ion-molecule reaction rate constant measurements. I. Apparatus and mobility measurements," *J. Chem. Phys.* **59** (12), 6610-6619 (1973).
- [Mcg98] R. T. McGrath, R. Veerasingham, J. A. Hunter, P. D. Rockett, and R. B. Campbell, "Measurements and simulations of VUV emissions from

- plasma flat panel display pixel microdischarges,” *IEEE Trans. Plasma Sci.* **26** (5), 1532-1542 (1998).
- [Meu95] J. Meunier, Ph. Belenguer, and J. P. Boeuf, “Numerical model of an ac plasma display panel cell in neon-xenon mixtures,” *J. Appl. Phys.* **78** (2), 731-745 (1995).
- [Mey90] M. Meyyappan and J. P. Kresovsky, “Glow discharge simulation through solutions of the moments of the Boltzmann equation,” *J. Appl. Phys.* **68** (4), 1506-1512 (1990).
- [Mol92] A. F. Molisch, B. P. Oehry, and G. Magerl, “Radiation-trapping in a plane-parallel slab,” *J. Quant. Spectrosc. Radiat. Transfer*, **49** (4), 361-370 (1993).
- [Mol93] A. F. Molisch, B. P. Oehry, W. Schupita, and G. Magerl, “Radiation-trapping in cylindrical and spherical geometries,” *J. Quant. Spectrosc. Radiat. Transfer*, **49** (4), 361-370 (1993).
- [Mor94] K.W. Morton and D.F. Mayers, *Numerical Solution of Partial Differential Equations* (Cambridge University Press, 1994).
- [Mot65] N. F. Mott and H. S. W. Massey, “The theory of atomic collisions,” third edition, Oxford University Press, London (1965).
- [Mot85] O. Motret, J. M. Pouvesle, and J. Stevefelt, “Spectroscopic study of the afterglow excited by intense electrical discharges in high-pressure helium hydrogen mixtures,” *J. Chem. Phys.* **83**, 1095 (1985).
- [Mue91] H. Mueller, “Modellierung von Excimer-Gasentladungen zur Erzeugung spektral selektiver Strahlung,” Ph.D. thesis (University of Karlsruhe, Germany, 1991).
- [Nag97] V. P. Nagorny and P. J. Drallos, “Effective secondary emission coefficient in a high-pressure noble gas,” *Plasma Sources Sci. Technol.* **6**, 212-219 (1997).
- [New48] R. R. Newton, “Transients in Townsend discharges,” *Phys. Rev.* **73** (6), 570-583 (1948).
- [Ney70] R. H. Neynaber and Y. S. Tang, *J. Chem. Phys.* **70**, 4272-4276 (1970).
- [Nie97] G.J. Nienhuis, W.J. Goedheer, E.A.G. Hamers, W.G.J.H. van Sark, and J. Bezemer, “A self-consistent fluid model for radio-frequency discharges in SiH₄-H₂ compared to experiments,” *J. Appl. Phys.* **82** (5), 2060 (1997).
- [Nit94] T.E. Nitschke and D.B. Graves, “A comparison of particle in cell and fluid model simulations of low-pressure radio frequency discharges,” *J. Appl. Phys.* **76**, 5646 (1994).
- [Opa71] C. B. Opal, W. K. Peterson, and E. C. Beaty, “Measurements of secondary electron spectra produced by electron impact ionization of a number of simple gases,” *J. Chem. Phys.* **55**, 4100-4106 (1971).
- [Ove00] G. Oversluizen and S. de Zwart, private communication (Philips Research Laboratories, Eindhoven, The Netherlands, 2000).
- [Pas93] J. D. P. Passchier and W. J. Goedheer, “A two-dimensional model for an argon rf discharge,” *J. Appl. Phys.* **74** (6), 3744-3751 (1993).
- [Phe94] A. V. Phelps, “The application of scattering cross sections to ion flux models in discharge sheaths,” *J. Appl. Phys.* **76** (2), 747-753 (1994).
- [Phe99] A. V. Phelps and Z. Lj. Petrovic, “Cold-cathode discharges and breakdown in argon: surface and gas phase production of secondary electrons,” *Plasma Sources Sci. Technol.* **8**, R21-R44 (1999).
- [Pit98] L. C. Pitchford, private communication (CPAT Toulouse, France, 1998).

- [Pre92] W. H. Press, S. A. Teukolsky, W. T. Vettering, and B. P. Flannery, "Numerical recipes in C," second edition (Cambridge University Press, 1992).
- [Pue91] V. Puech and S. Mizzi, "Collision cross section and transport parameters in neon and xenon," *J. Phys. D* **24** (11), 1974-1985 (1991).
- [Pun98] C. Punset, J.-P. Boeuf, and L. C. Pitchford, "Two-dimensional simulation of an alternating current matrix plasma display cell: Cross-talk and other geometric effects," *J. Appl. Phys.* **83** (4), 1884-1897 (1998).
- [Pun98a] C. Punset, Th. Callegari, and J.-P. Boeuf, "Physics of plasma displays – from understanding to optimization," in the proceedings of the International Symposium on Future Emissive Displays (Tottori University, Tottori, Japan, December 10-11, 1998), pp. 87-93.
- [Rai91] Y. P. Raizer, "Gas discharge physics," (Springer-Verlag Berlin, 1991).
- [Rap65] D. Rapp and P. Englander-Golden, *J. Chem. Phys.* **43**, 1464-1479 (1965).
- [Rau99] S. Rauf and M. J. Kushner, "Dynamics of a coplanar-electrode plasma display panel cell. I. Basic operation," *J. Appl. Phys.* **85** (7), 3460-3469 (1999).
- [Rau99a] S. Rauf and M. J. Kushner, "Dynamics of a coplanar-electrode plasma display panel cell. II. Cell optimization," *J. Appl. Phys.* **85** (7), 3470-3476 (1999).
- [Reg84] D. F. Register and S. Tajamar, *Phys. Rev. A* **29**, 1793-1810 (1984).
- [Rho84] C. Rhodes, "Rare gas halogen excimers", 1984.
- [Ric87] A.D. Richards, B.E. Thompson, and H.H. Sawin, "Continuum modeling of argon radio frequency glow discharges," *Appl. Phys. Lett.* **50** (9), 492 (1987).
- [Roa76] P.J. Roache, *Computational Fluid Dynamics* (Hermosa, Albuquerque NM, 1976).
- [Sak91] S. Sakabe and Y. Izawa, "Cross sections for resonant charge transfer between atoms and their positive ions: collision velocity < 1 a.u.," *Atomic data and Nuclear Data Tables* **49** (2), 257-314 (1991).
- [Sch69] D.L. Scharfetter and H.K. Gummel, "Large-signal analysis of a silicon Read diode oscillator," *IEEE Trans. Electron Devices* **ED 16**, 64 (1969).
- [Sch81] G. E. Schneider and M. Zedan, "A modified strongly implicit procedure for the numerical solution of field problems," *Numerical Heat Transfer* **4**, 1-19 (1981).
- [Shk66] I. P. Shkarovsky, T. W. Johnston, and M. P. Bachynski, "The particle kinetics of plasmas," (Addison-Wesley, Reading, MA, 1966).
- [Sku68] H. R. Skullerud, "The stochastic computer simulation of ions in a gas subjected to a constant electric field," *J. Phys. D* **1**, 1567-1568 (1968).
- [Slo76] H. G. Slottow, *IEEE Trans. Electron Devices* **ED-23**, 760 (1976).
- [Slo99] U. van Slooten and H. Schreuders, private communication (Philips Research Laboratories, Eindhoven, The Netherlands, 1999).
- [Sni99] R. Snijkers and M. Klein, "VUV spectroscopy and VUV and IR space and time resolved emission of AC-PDP microdischarges," poster presentation at the 52nd Gaseous Electronics Conference (Nolfolk, Virginia, USA, 1999).
- [Sob91] A. Sobel, "Plasma displays," *IEEE Trans. Plasma Sci.* **19** (6), 1032-1047 (1991).
- [Ste82] J. Stevefelt, J. M. Pouvesle, and A. Bouchoule, "Reaction kinetics of a

- high pressure helium fast discharge afterglow,” *J. Chem. Phys.* **76** (8), 4006-4015 (1982).
- [Sur90] M. Surendra, D. B. Graves, and G. M. Jellum, “Self-consistent model of a direct-current glow discharge: Treatment of fast electrons”, *Phys. Rev. A* **41** (2), 1112-1125 (1990).
- [Vee95] R. Veerasingam, R. B. Campbell, and R. T. McGrath, “One-dimensional fluid and circuit simulation of an ac plasma display cell,” *IEEE Trans. Plasma Sci.* **23** (4), 688-697 (1995).
- [Vee96] R. Veerasingam, R. B. Campbell, and R. T. McGrath, “Two-dimensional simulations of plasma flow and charge spreading across barrier pixels in ac plasma displays,” *IEEE Trans. Plasma Sci.* **24** (6), 1411-1421 (1996).
- [Vee97] R. Veerasingam, R. B. Campbell, and R. T. McGrath, “One-dimensional fluid simulations of a helium-xenon filled ac colour plasma flat panel display pixel,” *Plasma Sources Sci. Technol.* **6**, 157-169 (1997).
- [Ven93] P.L.G. Ventzek, T.J. Sommerer, R.J. Hoekstra, and M.J. Kushner, “Two-dimensional hybrid model of inductively coupled plasma sources for etching,” *Appl. Phys. Lett.* **63**, 605-607 (1993).
- [Ven95] P.L.G. Ventzek, R.J. Hoekstra, and M.J. Kushner, “Two-dimensional modeling of high plasma density inductively coupled sources for materials processing,” *J. Vac. Sci. Technol. B* **12**, 461 (1994).
- [Web85] L. Weber, “Plasma Displays,” in “Flat-Panel Displays and CRTs,” edited by L. Tannas, 332-407 (Van Nostrand Reinhold, 1985).
- [Wes75] G. F. Weston, *J. Phys. E* **8**, 981 (1975).
- [Yos83] S. Yoshida, A. V. Phelps, and L. C. Pitchford, “Effect of electrons produced by ionization on calculated electron-energy distributions,” *Phys. Rev. A* **27** (6), 2858-2867 (1983).

Publications

G. J. M. Hagelaar and G. M. W. Kroesen, "Implementing arbitrarily shaped boundaries in two-dimensional discharge modeling," *IEEE Trans. Plasma Sci.* **27** (6), 1606-1609 (1999).

G. J. M. Hagelaar and G. M. W. Kroesen, "Speeding up fluid models for gas discharges by implicit treatment of the electron energy source term," *J. Comput. Phys.* **159**, 1-12 (2000).

G. J. M. Hagelaar, F. J. de Hoog, and G. M. W. Kroesen, "Boundary conditions in fluid models of gas discharges," *Phys. Rev. E* **62** (1), 1452-1454 (2000).

G. J. M. Hagelaar, G. M. W. Kroesen, U. van Slooten, and H. Schreuders, "Modeling of the microdischarges in plasma addressed liquid crystal displays," *J. Appl. Phys.* **88** (5), 2252-2262 (2000).

G. J. M. Hagelaar, G. M. W. Kroesen, and M. H. Klein, "Energy distribution of ions and fast neutrals in microdischarges for display technology," *J. Appl. Phys.* **88** (5), 2240-2245 (2000).

M. Klein, R. Snijkers, and G. Hagelaar, "Energy loss mechanisms in AC-PDP discharges," accepted for publication in *IEEE Trans. Plasma Sci.*.

G. J. M. Hagelaar and G. M. W. Kroesen, "A Monte Carlo modeling study of the electrons in the microdischarges in plasma addressed liquid crystal displays," accepted for publication in *Plasma Sources Sci. Techn.*.

G. J. M. Hagelaar, M. H. Klein, R. J. M. M. Snijkers, and G. M. W. Kroesen, "Resonance radiation transport in plasma display panels," accepted for publication in *J. Appl. Phys.*.

G. J. M. Hagelaar, M. H. Klein, R. J. M. M. Snijkers, and G. M. W. Kroesen, "Energy loss mechanisms in the microdischarges in plasma display panels," submitted for publication in *J. Appl. Phys.*.

Summary

To the present day, the television (TV) market has been dominated by bulky cathode ray tube displays. Recently however, two alternative display technologies have emerged that offer the possibility of more elegant, flat, lightweight TVs. Both of these technologies make use of exceptionally small gas discharges: microdischarges. Best known is the plasma display panel (PDP) technology, which uses microdischarges to generate the light of the display. The other technology, known as plasma addressed liquid crystal (PALC), uses microdischarges as electrical switching elements.

The display industry asks for physical models that help to understand and predict the behavior of the microdischarges, because these discharges are so small that they are very hard to study experimentally. Within the past few years, several numerical models of PDP discharges have been developed in plasma groups all over the world. In contrast, only one model of PALC discharges has been reported in the literature so far. The main goal of the work presented in this thesis is to obtain a numerical model that is capable of simulating the full operation of both PALC and PDP discharges, and that can be used in the display industry for optimization of the microdischarge properties. In addition to this, there is the more academic goal to contribute to discharge modeling in general.

The core of the work is the development of a two-dimensional self-consistent fluid model. This model is based on continuity equations and drift-diffusion equations for plasma particle species, a balance equation for the electron energy, and Poisson's equation for the electric potential. Surface processes, such as secondary electron emission and the accumulation of surface charge, are taken into account in the boundary conditions of these equations. It is shown in this thesis that the boundary conditions used by most other authors fall short of physical reality in several ways. In the present work alternative boundary conditions are used, which are more realistic. The fluid model is implemented into a computer program in a flexible and userfriendly way. A new numerical technique has been developed for the implicit time integration of the system of fluid equations, which makes it possible to use large numerical time steps, without consequences for the stability of the calculation. This makes the model very fast: a typical micro-discharge simulation takes only a few minutes of computation time.

The fluid model has been used to study PALC-discharges in pure helium and helium-hydrogen mixtures. The results show that these discharges are similar to classical direct current glow discharges. Trends in calculated current-voltage characteristics agree with measured trends. For the PALC technology it is important that the discharges are extinguished quickly. In pure helium this is not the case because collisions between metastables lead to a persistent plasma production, as appears from the simulations. Helium-hydrogen discharges contain much less helium metastables and are extinguished almost instantaneously. Calculated plasma decay times are in excellent agreement with measured decay times. The simulations demonstrate that experimentally observed inhomogeneities in the transmission of picture elements result from electrical interaction between consecutive picture lines.

The fluid model has also been used to study the energy losses in PDP discharges. The simulation results provide a detailed insight in the physical mechanisms behind these energy losses, and agree with measured trends in the luminous efficacy of PDPs.

It turns out that the larger part of the electrical input energy is used for the acceleration of ions, and thus lost for light production.

The fluid model is based on assumptions for the electron energy distribution function (EEDF). Using a Monte Carlo model for electrons, the validity of these assumptions is investigated for the electrons in PALC-discharges in pure helium. The Monte Carlo model simulates the paths of individual electrons, where the occurrence and effect of collisions are treated by random numbers. The Monte Carlo calculations show that near the cathode the EEDF displays peaks of fast electrons and has a depopulated tail. Although these effects are not included in the fluid model, both models lead to the same electron density. The ionization in the fluid model is too much localized at the cathode. According to the Monte Carlo calculations, the energetic electrons produced by metastable-metastable collisions hardly lose any of their initial energy, and require a special treatment in the fluid model.

To be able to improve the lifetime of PALC and PDP displays, it is important to know the energy distribution of the ions and fast neutrals that impinge on the surfaces surrounding the microdischarges. This information cannot be obtained directly from the fluid model. In this thesis however, simple analytical distribution functions are derived, which make it possible to estimate the energy distributions from the results of the fluid model. The distribution functions are essentially different from the Maxwellian function, and are in good agreement with more comprehensive Monte Carlo calculations.

In describing the emission of resonance radiation from PDP-discharges, the fluid model uses a trapping factor. The validity of this crude approach is investigated using a Monte Carlo model for the transport of resonance photons. The results of this model are in good agreement with both the fluid modeling results and measured emission spectra.

In short, the fluid model is supported by experimental data as well as Monte Carlo calculations, and uncovers the main physical mechanisms underlying the behavior of the microdischarges.

Samenvatting

Tot op heden wordt de televisiemarkt overheerst door logge kathodestraalbeeldbuizen. Sinds enkele jaren zijn er echter twee alternatieve beeldschermtechnologieën in opkomst die de mogelijkheid bieden tot veel elegantere, platte, lichtgewicht tv's. Beide technologieën maken gebruik van uitzonderlijk kleine gasontladingen: micro-ontladingen. Het meest bekend is de *plasma display panel* (PDP) technologie, die micro-ontladingen gebruikt om het licht van het beeldscherm te genereren. De andere technologie, *plasma addressed liquid crystal* (PALC) genaamd, gebruikt micro-ontladingen als elektrische schakelementen.

In de beeldschermindustrie bestaat behoefte aan natuurkundige modellen die het mogelijk maken het gedrag van de micro-ontladingen beter te begrijpen en te voorspellen, vooral omdat deze vanwege hun kleine afmetingen zeer moeilijk experimenteel te onderzoeken zijn. De afgelopen jaren zijn dan ook in diverse plasmagroepen over de hele wereld numerieke modellen voor PDP-ontladingen ontwikkeld. Voor PALC-ontladingen is tot nu toe slechts één model beschreven in de literatuur. Het hoofddoel van het werk beschreven in dit proefschrift is het verkrijgen van een numeriek model dat in staat is om zowel PALC- als PDP-ontladingen volledig te simuleren, en dat in de beeldschermindustrie gebruikt kan worden om de eigenschappen van deze ontladingen te optimaliseren. Daarnaast is ernaar gestreefd bij te dragen aan de gasontladingsmodellering in het algemeen.

De kern van het werk is de ontwikkeling van een tweedimensionaal zelfconsistent vloeistofmodel. Dit model is gebaseerd op continuïteitsvergelijkingen en drift-diffusievergelijkingen voor allerlei soorten plasmadeeltjes, een energiebalans voor elektronen, en de Poisson-vergelijking voor de elektrische potentiaal. Wandprocessen, zoals secundaire elektronemissie en de opbouw van wandladingen, worden in rekening gebracht in de randvoorwaarden van deze vergelijkingen. In dit proefschrift wordt aangetoond dat de randvoorwaarden die gebruikt worden door menige andere auteur geen goede beschrijving geven van het deeltjestransport aan de wand. In dit werk worden daarom alternatieve randvoorwaarden gebruikt, die realistischer zijn. Het vloeistofmodel is op flexibele en gebruiksvriendelijke wijze geïmplementeerd in een computerprogramma. Er is een nieuwe numerieke techniek ontwikkeld voor de impliciete tijdsintegratie van het systeem van vloeistofvergelijkingen, die het mogelijk maakt een zeer grote numerieke tijdstap te gebruiken, zonder dat de berekening instabiel wordt. Het model is daardoor zeer snel: een gemiddelde micro-ontladingssimulatie duurt slechts enkele minuten.

Met het vloeistofmodel zijn PALC-ontladingen gesimuleerd in puur helium en helium-waterstofmengsels. De resultaten laten zien dat deze ontladingen nauw verwant zijn aan klassieke gelijkstroom-glimontladingen. Trends in berekende stroomspanningskarakteristieken zijn in goede overeenkomst met gemeten trends. Voor de PALC-technologie is het van belang dat de ontladingen snel uitdoven. In puur helium is dit echter niet het geval doordat botsingen tussen metastabielen voor een aanhoudende plasmaproductie zorgen, zo blijkt uit de simulaties. Helium-waterstofontladingen bevatten veel minder heliummetastabielen en doven vrijwel instantaan uit. Berekende plasmavervaltijden zijn in goede overeenkomst met gemeten vervaltijden. De simulaties laten zien dat experimenteel waargenomen

inhomogeniteiten in transmissie van beeldelementen veroorzaakt worden door elektrische interactie tussen opeenvolgende beeldlijnen.

Tevens is met het vloeistofmodel een studie gedaan naar de energieverliezen die optreden in PDP-ontladingen in neon-xenonmengsels. De simulatieresultaten geven een gedetailleerd inzicht in de fysische mechanismen die ten grondslag liggen aan deze energieverliezen, en vertonen bovendien een goede overeenkomst met gemeten trends in de energie-efficiëntie van PDP's. Het blijkt dat het merendeel van de elektrische energie die aan de ontladingen wordt toegevoerd gebruikt wordt voor de versnelling van ionen en derhalve niet bijdraagt tot de vorming van licht.

Het vloeistofmodel is gebaseerd op aannames met betrekking tot de elektronenergieverdelingsfunctie (EEDF). Met behulp van een Monte Carlo-model voor elektronen is de geldigheid deze aannames onderzocht voor PALC-ontladingen in puur helium. In het Monte Carlo-model wordt de beweging van individuele elektronen gesimuleerd, waarbij *random numbers* gebruikt worden om botsingen in rekening te brengen. De Monte Carlo-berekeningen laten zien dat in de buurt van de kathode de EEDF pieken vertoont van snelle niet-botsende elektronen en een ontvolkte staart heeft. Ofschoon deze niet-evenwichtsverschijnselen niet zijn opgenomen in het vloeistofmodel, leiden beide modellen tot dezelfde elektronendichtheid. De ionisatie is in het vloeistofmodel echter te zeer gelokaliseerd bij de kathode. Volgens de Monte Carlo-berekeningen verliezen de energetische elektronen die geproduceerd worden in metastabiel-metastabielbotsingen slechts een klein gedeelte van hun oorspronkelijke energie, waardoor zij een speciale behandeling behoeven in het vloeistofmodel.

In verband met de verbetering van de levensduur van de PALC- en PDP-beeldschermen is het belangrijk de energieverdeling te kennen van de ionen en snelle neutralen die inslaan op de wanden rondom de micro-ontladingen. Deze informatie kan niet direct worden verkregen uit het vloeistofmodel. In dit proefschrift worden echter door middel van een analytische beschouwing eenvoudige verdelingsfuncties afgeleid, die het mogelijk maken om de energieverdeling van de bewuste ionen en snelle neutralen af te schatten uit de resultaten van het vloeistofmodel. Deze verdelingsfuncties zijn essentieel anders dan de Maxwellse verdelingsfunctie, en zijn in goede overeenkomst met de resultaten van meer geavanceerde Monte Carlo-berekeningen.

Bij de beschrijving van de emissie van resonantiestraling in PDP-ontladingen maakt het vloeistofmodel gebruik van een opsluitingsfactor. Om de juistheid van deze grove benadering te onderzoeken, is een Monte Carlo-model voor het transport van resonantiefotonen ontwikkeld. De resultaten van dit model zijn in goede overeenkomst met die van het vloeistofmodel alsook met gemeten emissiespectra.

Kortom, het vloeistofmodel wordt gesteund door zowel experimentele gegevens als Monte Carlo-berekeningen en legt de belangrijkste fysische mechanismen bloot die schuil gaan achter het gedrag van de micro-ontladingen.

Dankwoord

Graag wil ik de volgende mensen bedanken:

Promotoren Gerrit Kroesen en Frits de Hoog, voor hun steun; bijzondere dank aan groepsleider Gerrit voor het vertrouwen en de grote vrijheid. Philips-medewerkers Udo van Slooten, Leendert Vriens, Markus Klein, Rob Snijkers, en Herman Schreuders, voor de prettige samenwerking. Groepsgenoten Loek Baede, Leon Bakker, Lambert Bisschops, Rina Boom, Jean-Charles Cigal, Marianne van den Elshout, Hans Freriks, Marc van de Grift, Daiyu Hayashi, Tarik Hbid, Marcel Hemerik, Wilfred Hoeben, Carole Maurice, Gabriela Paeva, Wijnand Rutgers, Eva Stoffels, Winfred Stoffels, Geert Swinkels, en Eddie van Veldhuizen, voor de goede sfeer; bijzondere dank aan T. H. en C. M.. Ervaren plasmamodelleurs Leanne Pitchford, Jean-Pierre Boeuf, en Wim Goedheer, voor hun belangstelling en hulp.

Curriculum vitae

- 8 april 1973 geboren te Helmond
- 1985 – 1991 atheneum, Scholengemeenschap Jan van Brabant, Helmond
- 1991 – 1996 studie technische natuurkunde, Technische Universiteit Eindhoven
- 1994 – 1996 propaedeuse psychologie, Katholieke Universiteit Brabant
- 1997 – 2000 promotieonderzoek, groep Elementaire Processen in Gasontladingen, Faculteit Technische Natuurkunde, Technische Universiteit Eindhoven

